Fine-scale grassland monitoring using unmanned aerial vehicle borne remote sensing

Dissertation to obtain the academic degree
Doktor der Agrarwissenschaften (Dr. agr.)

Submitted to Faculty of Organic Agricultural Sciences
of the University of Kassel, Germany

Jayan Sri Jeewantha Wijesingha

Witzenhausen, April, 2020

This work has been accepted by the Faculty of Organic Agricultural Sciences of the University of Kassel as a thesis for acquiring the academic degree Doktor der Agrarwissenschaften (Dr. agr.).

- Supervisor: Prof. Dr. M. Wachendorf, University of Kassel, Germany
- Co-supervisor: Prof. Dr. J. Isselstein, University of Göttingen, Germany

The oral defence day : 25th March 2020

Preface

This dissertation was submitted to the Faculty of Organic Agricultural Sciences of the University of Kassel to fulfil the requirements for the degree Doctor of Agricultural Sciences (Dr. agr.). The dissertation comprises of two published articles and one submitted manuscript in peer-reviewed international journals. The list of the published articles and the submitted manuscript referring to the chapters in the thesis is provided below.

Chapter 3: Wijesingha, J., Moeckel, T., Hensgen, F., Wachendorf, M., 2019. Evaluation of 3D point cloud-based models for the prediction of grassland biomass. International Journal of Applied Earth Observation and Geoinformation. 78, 352–359. doi:10.1016/J.JAG.2018.10.006

Chapter 4: Wijesingha, J., Astor, T., Schulze-Brüninghoff, D., Wengert, M., Wachendorf, M., 2020. Predicting forage quality of grasslands using UAV-borne imaging spectroscopy. Remote Sensing. 12. doi:10.3390/rs12010126

Chapter 5: Wijesingha, J., Astor, T., Schulze-Brüninghoff, D., Wachendorf, M., 2020. Mapping invasive *Lupinus polyphyllus* Lindl. in semi-natural grasslands using object-based analysis of UAV-borne images. (Manuscript submitted for publication in Journal of Photogrammetry, Remote Sensing and Geoinformation Science)

Acknowledgement

This dissertation is the only output that I can show about three years of my life with reading, planning, data collecting, analysing, reporting, writing, rejecting as well as having fun. This journey was made possible by the valuable support and help of many individuals, and I would like to extend my sincere gratitude to all of them.

First of all, I wish to express my heartiest appreciation to my supervisor Prof. Dr. Michael Wachendorf, for guiding me through in the last three years. I am deeply thankful for giving me the opportunity of working at the research group and enlightening me with grassland science and providing excellent advisory support in both high and low time. I thank Prof. Dr. J. Isselstein, for reviewing my dissertation. I acknowledge all members of the PhD examination committee, who came to evaluate the oral defence during the COVID-19 pandemic time.

I would also like to thank Dr. Thomas Astor for the invaluable contribution and inspiring scientific discussion that we shared. Also, my sincere thanks go to Dr. Thomas Fricke and Dr. Frank Hesngen for educating me to grassland science and being supportive whenever I needed.

I much appreciate specifically Susanne Günther, Andrea Gerke, Wolfgang Funke and all technical team and student helpers for their total support in fieldwork and lab analysis. Thank a lot, Ben, Isaac, Supriya, Sarah, Esther, Damian, Matthias, & Fruzsina for your invaluable help during last three years and thanks ever so much for all the memories that we shared together.

I want to thank my parents, two brothers in Sri Lanka who have loved and helped me unconditionally not only the thesis time but also throughout my life.

My lovely wife, Anu, thank you so much for everything. Without your help, this work would not have been possible. Additionally, I must be thankful to my son Yevon, who brought me so much joy and happiness into my life.

Last, not least, my thanks and appreciation also go to my colleagues in GNR, Sri Lankan friends in Germany and all the people who have willingly helped me.

Witzenhausen, April, 2020 *Jayan S.J. Wijesingha*

This dissertation is dedicated to

my beloved parents and my wife
who encouraged me to pursue my dreams.

"If we could first know where we are, and whither we are tending, we could then better judge what to do, and how to do it"

Abraham Lincoln

Contents

List of Figures

List of Tables

List of Abbreviations

2D	2-dimensional
3D	3-dimensional
ADF	acid detergent fibre
adj.R^2	adjusted r square
ASM	angular second moment
CBR	cubist regression
CC	circle compactness
CHM	canopy height model
CP	crude protein
DB	dry biomass
DC	dark current
DM	dry matter
DN	digital number
DSM	digital surface model
DTM	digital terrain model
FB	fresh biomass
FD	fractional dimension
FN	false-negative
FP	false-positive
FPR	false-positive-rate
GCP	ground control point
GNSS	global navigation satellite system
GPR	gaussian processes regression
HIS	hue, intensity, saturation
IDM	inverse difference moment
IMG	intensively managed grassland
K	kappa coefficient
L	lupine
LA	lupine area

LHM	lowland hay meadow
LiDAR	light detection and ranging
m.a.s.l	mean above sea level
MA	map accuracy
MHM	mountain hay meadow
MHML	mountain hay meadow invaded by *Lupinus polyphyllus*
ML	machine learning
N	nitrogen
NA	not assessed
NDSI	normalised difference spectral index
NIRS	near infrared spectroscopy
NL	non-lupine
nRMSE	normalised root mean square error
NSG	*Nardus stricta* grassland
NSGL	*Nardus stricta* grassland invaded by *Lupinus polyphyllus*
OA	overall accuracy
OBIA	object based image analysis
PA	precision agriculture
PCC	pixel-wise correlation coefficient
PD	point density
PLSR	partial least squares regression
QGIS	quantum geographic information system
RF	random forest
RFR	random forest regression
RGB	red, green, blue
RMSE	root mean square error
RS	remote sensing
RTK	real time kinematic
SD	standard deviation
SFM	structure from motion
SR	spectral ration
SSI	spectral shape index
SVR	support vector regression
TLS	terrestrial laser scanner
TN	true-negative
TP	true-positive
TPR	true-positive-rate
UAV	unmanned aerial vehicle

USPO	unsupervised parameters optimisation
V_0	Vegetation at reference time
V_{2weeks}	two weeks older vegetation
V_{4weeks}	four weeks older vegetation
VR_{2weeks}	two weeks regrown vegetation after mowing
VR_{4weeks}	four weeks regrown vegetation after mowing
WC	white calibration

Summary

RS is widely employed as a non-destructive methodology to monitor grasslands. Usage of UAV as the RS platform benefits to provide high spatial (fine-grain) and temporal resolution, unclouded data over small grassland extent. Therefore, this thesis evaluated the applications of UAV-borne RS for fine-scale grassland monitoring along with practical farm condition. Grass biomass estimation, predicting forage quality of grass and mapping invasive lupine in grasslands are considered as applications of UAV-borne RS.

Amount of available grassland biomass at field-scale is essential information for grassland farmers as well as agronomists to make feeding plan to animals. Chapter 3 investigated the grass sward height derived from UAV-borne RGB images to estimate grassland biomass in three different grasslands with variable sward composition and mowing systems in northern Hesse, Germany. First, the strongly related CHM metric out of 10 metrics was found with both FB and DB. The 75^{th} percentile (p75) height was discovered as the highest correlated CHM metric with biomass according to Person's correlation coefficient values. Three different levels of linear empirical models (sampling date-specific, grassland-specific and global) were built to estimate grassland biomass using p75 height. The complexity of grassland sward was increased respectively to the order of modelling level. The sampling date-specific models provided the highest model performance, followed by grassland specific and global models. The results disclosed the potential of CHM derived from UAV-borne images for estimating fine-scale grassland biomass, although models were affected by species heterogeneity of grasslands.

The timely information of forage nutritional values of grassland is vital for feeding high-quality forage for ruminants. UAV-borne imaging spectroscopy data was examined in Chapter 4 to predict two crucial forage quality parameters (CP and ADF) for a multitude of grasslands in northern Hesse, Germany. First, the relationship with forage quality values and various spectral reflectance data sets were evaluated according to Person's correlation coefficient values. Based on that, normalised reflectance data was

found as the strongly associated dataset with forage quality values. Afterwards, the linear regression models were built against forage quality values and different spectral features (i.e. single bands, NDSIs, SRs). None of the linear models with spectral features offered excellent results. Therefore, ML regression models were built using all spectral bands. In that respect, five ML algorithms (PLSR, GPR, RFR, SVR, and CBR) were evaluated with 100 simulations. The SVR model obtained the highest model performances for CP estimation while the CBR model provided the best model for ADF estimation. Lastly, the trained ML model was utilised to generate maps of forage quality values of each grassland fields. The Chapter 4 revealed a combination of full spectral data and ML algorithms can provide comprehensive forage quality estimation model that can predict value regardless of grassland type.

Chapter 5 successfully developed a transferable, repeatable workflow to map invasive lupine grasslands using UAV-borne RS data and OBIA as an alternative standard image digitising. The UNESCO biosphere reserve "Rhön" consists of semi-natural grasslands where most of them were invaded by lupine. The spatial coverage of invasive lupine was crucial to understand invasion pattern, to plan control activities as well as to assess the results of eradication actions. RGB images and thermal images acquired form UAV was used in the developed workflow. In the image segmentation phase, CHM raster, PD raster and hue image were utilised to delineate image segments which represent lupine and non-lupine objects. Four geometric attributes and twenty-eight images-based attributes were computed for each object. An RF classification model was trained using all attributes. The lupine coverage maps generated from classification were compared against standard digitised maps. The accuracy of the lupine map from classification increased when there is low relative lupine coverage. This result indicates a combination of UAV-borne RS data and OBIA would be a valuable tool to map invasive lupine in grasslands.

Zusammenfassung

Fernerkundung ist eine weit verbreitete, nicht-destruktive Untersuchungsmethode im Grünland. Je nach Aufgabengebiet kommen unterschiedlichste Fernerkundungsplattformen (z. B. Satelliten, Flugzeuge, Drohnen und terrestrische Systeme) zum Einsatz. Der Vorteil des Einsatzes von Drohnen liegt in der Erzeugung von räumlich und zeitlich hochaufgelösten, wolkenfreien Daten, welche auf kleinen Günlandbeständen erhoben werden können. Diese Thesis untersucht die Anwendung von drohnenbasierten Fernerkundungssystemen im fein skalierten Grünlandmonitoring unter praktischen Bedingungen. Die Abschätzung von Grünlandbiomasse, die Vorhersage der Futterqualität von Grünlandaufwuchs und das Identifizieren der invasiven Stauden-Lupine werden als Einsatzzwecke für drohnenbasierte Fernerkundungssysteme in Betracht gezogen.

Die Menge verfügbaren Grünlandaufwuchses auf Feldniveau ist eine essenzielle Information für Landwirte, wie auch für Agrarwissenschaftler. Kapitel 3 untersucht die Vegetationshöhe, erhoben mittels drohnenbasierter RGB Bilder, zur Abschätzung von Grünlandbiomasse. Drei verschiedene Grünlandtypen mit unterschiedlicher Artzusammensetzung und Nutzungsintensität wurden hierfür in Nordhessen untersucht. Zunächst wurden aus einem Vegetationshöhenmodell (CHM) zehn Variablen abgeleitet und die beste Variable für die Modellierung von Frisch- und Trockenmasseertrag identifiziert. Das 75. Perzentil (p75) hatte die höchste Biomassekorrelation, gemessen am Korrelationskoeffizienten nach Pearson. Drei unterschiedliche Level von empirischen Modellen (Aufnahmezeit-spezifisch, Grünlandtyp-spezifisch und global) wurden zur Biomasseabschätzung mit Hilfe von p75 modelliert. Die Komplexität der Grünlandtypen stieg gleichermaßen in Reihenfolge der Modellierungslevel an. Das Aufnahmezeit-spezifische Modell erzielte die höchste Modellgenauigkeit, gefolgt vom Grünland-spezifischen und globalen Modell. Die Ergebnisse offenbaren das Potential der Vegetationshöhe aus drohnenbasierten Bildern zur detaillierten Schätzung von Grünlandbeständen, auch wenn die Modelle durch die Heterogenität der Bestände beeinflusst sind.

Die rechtzeitige Erfassung von Qualitätsparametern eines Grünlandbestandes ist entscheidend für die Bereitstellung von hochwertigem Futter für Wiederkäuer. In Kapitel 4 werden drohnenbasierte Spektraldaten untersucht, um zwei relevante Futterqualitätsparameter (Rohprotein und ADF) für eine Vielzahl von Grünlandtypen in Nordhessen zu bestimmen. Zunächst wurde die Beziehung zwischen Futterqualität und verschiedenen spektralen Reflektionsdatensätzen mittels des Korrelationskoeffizienten nach Pearson evaluiert. Hierbei zeigte sich, dass die normalisierten Reflektionsdaten die höchste Assoziation zu Futterqualitätswerten aufwiesen. Des Weiteren wurden lineare Regressionsmodelle mittels unterschiedlicher spektraler Features (z.B. Einzelbänder, NDSIs, SRs) gebaut. Keines dieser linearen Modelle aus spektralen Features erzielte exzellente Ergebnisse. Daher wurden Modelle des maschinellen Lernens mit allen verfügbaren spektralen Bändern eingesetzt. So wurden fünf unterschiedliche Algorithmen mit je 100 Simulationen evaluiert (PLSR, GPR, RFR, SVR und CBR). Die SVR Methode lieferte das beste Modell zur ADF Abschätzung. Zuletzt wurde das trainierte Modell genutzt, um Futterqualitätskarten für jeden Grünlandtyp zu erzeugen. Die Ergebnisse aus Kapitel 4 zeigen, dass eine Kombination aus der Nutzung der gesamten spektralen Daten in Modellen des maschinellen Lernens eine flächendeckende Schätzung der Futterqualität, unabhängig von Grünlandtypen, ermöglichen kann.

In Kapitel 5 zeigt sich die erfolgreiche Entwicklung eines transferierbaren, wiederholbaren Workflows zur Erzeugung von Karten Lupinen invadierten Grünlandes. Dies, mittels drohnenbasierter Daten und objektbasierter Bildanalyse (OBIA), als eine standardisierbare Bild-Digitalisierungsalternative. Das UNESCO Biosphärenreservat „Rhön“ ist geprägt durch extensive Grünlandtypen, von denen ein großer Teil durch die vielblättrige Lupine invadiert ist. Die räumliche Abundanz der invasiven Lupine ist wichtig zur Beurteilung der Ausbreitungsmechanismen, zur Planung von Kontrollmaßnahmen, wie auch zur Beurteilung des Erfolges solcher Maßnahmen. Drohnenbasiere RGB und Thermal-Bilder wurden zur Gestaltung eines Workflows genutzt. In der Phase der Bildsegmentierung wurde das Raster des Vegetationshöhenmodells (CHM) und das der Punktdichte (PD), sowie das Bild der Farbtonwerte genutzt, um die Daten in Objekte von Lupine und nicht-Lupine zu segmentieren. Vier geometrische und 28 bildbasierte Attribute wurden für jedes Objekt errechnet. Ein Random Forest (RF) Klassifikationsmodell wurde mithilfe der gesamten Daten trainiert. Die mittels Klassifikation erzeugten Lupinen-Karten wurden mit manuell digitalisierten Karten verglichen. Die Genauigkeit der Lupinen-Karten aus Klassifikationsmodellen verbesserte sich, wenn nur geringe Lupine-Deckung vorherrschte. Das Ergebnis zeigt, dass die Kombination aus drohnenbasierten Fernerkundungsdaten und OBIA ein wichtiges Werkzeug zur Erzeugung von Lupine-Deckungskarten im Grünland ist.

Chapter 1

Introduction

1.1 Grassland

'Grassland' is an ecosystem where grasses and herbs are the dominant species of the vegetation and woody species do not exceed 10 % of the total land cover (White 1983). Grassland ecosystems are the largest land ecosystems in the world, and they extend through all continents except Antarctica (Xu and Guo, 2015). Types of grassland can be classified or characterised in terms of soil type, climate condition, species composition, and land use management system (e.g. pasture, hay meadow) (Peeters, 2009). The role of grasslands as an ecosystem service provider is very prominent. It is linked to food provision, climate regulation, erosion regulation, water flow regulation, and recreation (Hönigová et al., 2012).

Grasslands cover approximately 70.5 million hectares in 28 European Union member countries in the year 2013 (33 % of the utilised agricultural area), and they are the most species-rich environments (Peeters, 2009; Leclère et al., 2016). According to Huyghe et al. (2014), grassland can be divided into two major groups i) permanent grassland and ii) temporary grassland. Grasslands that have not been disturbed by ploughing for more than five years are considered as the permanent grasslands. They can be further categorised as agriculture-improved grasslands and semi-natural grasslands which are intensively managed with improved yield and extensively managed with low yield respectively. Further, according to management practises, the permanent grasslands can be labelled as meadows (predominantly mowed) and pastures (predominantly grazed). The temporary grasslands are sown with the annual, biennial, or perennial forage species and experienced crop rotation practise (Huyghe et al., 2014).

The most prominent ecosystem service of grassland is forage provision to both domes-

tic and wild herbivores, i.e. cattle, sheep, goats, horses (Gibson, 2009). Since grass is providing the required nutritious feed to herbivores, it was considered as *the earth's green gold* (Frame and Laidlaw, 2011). The forage productivity of grassland is measured using annual forage dry matter quantity (DM) per area (usually using DM tonnes per hectare per year – t ha^{-1} $year^{-1}$). The productivity of grassland is dependent on different factors, namely temperature, rainfall and length of the day (Smit et al., 2008). Moreover, grassland productivity varies due to botanical composition and management practise (Gibson, 2009). In Europe, the productivity of grassland differs between 10 t ha^{-1} $year^{-1}$ in the Atlantic zone and 1.5 t ha^{-1} $year^{-1}$ in the Mediterranean (Smit et al., 2008).

Acting as a hotspot for biodiversity is another leading ecosystem service provided by grassland (Gibson, 2009). Grassland biodiversity is high because of its plant species richness and being a foundational habitat for animals ranging from small insects to large mammals (Silva et al., 2008). However, the biodiversity of grassland is threatened by many factors such as poor agricultural practises, intensified pesticide usage, increasing stocking rate, biological invasions by alien species, and climate change.

1.2 Grassland monitoring

The monitoring is an action of measuring and repeatedly detecting the change of phenomena (Smith et al., 1985). Monitoring of grassland, therefore, involves repetitive measurements of grassland vegetation and management activities (Heather and Nature, 1999). The two most common goals of monitoring grasslands are, to detect natural trends in the ecosystem, and to study the influence of external factors (Zielinska et al., 2015). Biophysical, biochemical plant traits (e.g. biomass, nutrition value), as well as species diversity, richness, and abundance, are concerned as monitoring attributes for natural trends. Grassland changes due to grazing or mowing activities, human intensification, different climatic situations (flood, drought, and wildfire), and biological invasion are related to the external factors.

Moreover, the ecological scale of the grassland monitoring varies from a large spatial extent (e.g. global, national or regional) with a coarser grain (e.g. Pan European grassland map with 100 m spatial resolution from European Environment Agency (2018)) to a small spatial extent (e.g. paddock scale, patch scale or field-scale) with a fine grain (less than 10 m spatial resolution) (t'Mannetje and Jones, 2000). From a greater extent with coarser grain, it is difficult to obtain a detailed botanical composition of grasslands, although it is possible to differentiate grassland types from other land cover types. In contrast, the small spatial extent of fine-grain monitoring provides more in-

depth information on the botanical composition of the grassland study area, but the outcomes are limited to the local level. Consequently, there is a trade-off between the spatial extent and the degree of details that need to be obtained in the monitoring system. Concurrently, temporal frequency is another important factor when it comes to grassland monitoring as well as other targets of monitoring (Heather and Nature, 1999). The monitoring intervals are the variable of the temporal frequency. However, monitoring intervals usually depend on the scale and the goals of the monitoring.

Decisively, when it comes to grassland management, it is an important aspect to monitor grassland variation within the field or paddock level due to spatial and temporal heterogeneity (Schellberg et al., 2008). Primarily, there is a necessity to get information regarding production, nutritional value, and invasive species or functional group of species within the paddock to better achieve management goals (t'Mannetje and Jones, 2000). Secondly, the European grassland distribution is fragmented, and small grassland fields are existing (Zillmann et al., 2014). Therefore, it is indispensable to monitor grassland in the small spatial extent (field or paddock) of fine-grain (from now on referred to as fine-scale) with different focus areas.

One of the most common fine-scale grassland monitoring methods is in-situ (ground-based) monitoring (Ali et al., 2016; Wachendorf et al., 2017). Measurement tools such as rising plate meter, and laboratory analysis using cut grassland samples are some examples of the in-situ type monitoring techniques. Usually, observations are sampled one-dimensionally (point-based) in the field. Subsequently, data is interpolated to obtain a field map, which generally provides fine-scale information of the study area. On the downside, this process is a time-consuming and labour-intensive method which can be untenable in the estimation of results for large areas (t'Mannetje and Jones, 2000; Ali et al., 2016; Wachendorf et al., 2017). On the contrary, remote sensing can overcome those limitations.

1.3 Remote sensing for grassland monitoring

Remote Sensing (RS) is defined as the act of collecting or acquiring information about the object(s) without getting in contact with them (Bhatta, 2013). RS provides the opportunity to extend information from fine-scale to larger scale for land ecosystem monitoring (Borre et al., 2011). It allows to measure and model the ecosystem at various spatial and temporal scales (Ali et al., 2016). According to the two review articles by Ali et al. (2016) and Wachendorf et al. (2017), several studies have applied RS as a non-destructive sampling method to (a) classify grassland types, (b) model grassland biomass, growth rate, as well as forage nutritional values and (c) map species compo-

sition and biodiversity among others. Furthermore, it is summarised that different RS platforms and sensors have certain limitations in estimating the grassland ecosystem's attributes. There is a strong relationship between reflectance derived from the visible and the infrared region of the spectrum and vegetation properties, which can be utilised to estimate vegetation properties through optical RS. In particular, hyperspectral RS data have the full potential to estimate grassland biomass and forage quality (Biewer et al., 2009a; Biewer et al., 2009b; Safari et al., 2016b). Furthermore, it was proven that the grass canopy height derived from RS data also has the potential to estimate grassland biomass (Fricke et al., 2011; Safari et al., 2016a).

In the matter of fine-scale grassland mapping and monitoring, neither satellite- nor ground-borne remote sensing data provide sufficient information (Ali et al., 2016; Möckel et al., 2016). The primary reasons that satellite-borne RS data is not suitable for fine-scale grassland monitoring are, (a) limitations of the spatial resolution to address fine-scale elements in fragmented grassland landscape, (b) unavailability of timely satellite RS data due to cloud coverage, and (c) insufficient revisit time of the satellite sensors (Wachendorf et al., 2017). In contrast, point-based ground-borne RS data (e.g. field spectroscopy, ultra-sonic sensor) provides adequate detailed information. However, the data collection over a larger area is challenging because of the high demand for labour and time. Alternatively, the usage of Unmanned Aerial Vehicles (UAVs) as RS platform can obtain a high spatial resolution, unclouded, and timely RS data over larger fields or paddocks for monitoring grasslands at fine-scale (Möckel et al., 2016).

1.4 UAV-borne remote sensing for grassland monitoring

The rapid development of technology during the last decades has introduced miniature versions of most electronic appliances. Simultaneously, the field of RS has broadened with technology development. Subsequently, UAVs have become a platform for lightweight and small remote sensors, which added a new area of RS called UAV-borne RS (Wijesingha, 2016). The combination of the UAV and mini remote sensors provide cloud-free, high spatial resolution, and timely available data (Ma et al., 2013). Within the last 5-6 years, UAV-borne RS has rapidly developed in terms of payload sensors, flight time, and image processing. Currently, UAVs are equipped with various types of imaging and non-imaging sensors (i.e. consumer-grade visible cameras (red, green, blue (RGB) cameras), multispectral sensors, hyperspectral sensors, and thermal sensors) which provide high spatial and spectral resolution data. In addition to the spectral data, UAV-borne RS can provide 3-dimensional (3D) point cloud data which is advantageous to the derivation of the height of the vegetation canopies (Bendig, 2015).

Typically, overlapping images in both forward and side directions to the flight line are acquired during the UAV-borne RS data collection. The 2-dimensional (2D) overlapping images are processed using a computer vision technology called structure from motion (SFM) which results in two main outputs, namely 3D point cloud and ortho-mosaic. The 3D point cloud is a collection of points where each point consists of x, y, z coordinates in space which can be employed to derive structural parameters of the observed object such as height and volume. The ortho-mosaic is a mosaic of the collected UAV-borne images that is ortho-rectified where each pixel contains the corresponding sensor data (e.g. spectral reflectance, temperature) (Snavely et al., 2006; Wijesingha, 2016). Consequently, the UAV as an RS platform can overcome the mentioned limitations in satellite-borne or ground-borne RS for fine-scale grassland monitoring (Wachendorf et al., 2017).

The allometric relationship between sward height or tiller blade length and biomass has proven as a basis for non-destructive methods to predict grassland biomass. This was employed to model fine-scale grassland biomass using ruler height (Santillan et al., 1979; Williamson et al., 1987), ultra-sonic sensor derived sward height (Frame and Laidlaw, 2011), and terrestrial laser scanner derived sward height (Wallace et al., 2017; Schulze-Brüninghoff et al., 2019). Likewise, 3D point clouds obtained from the UAV-borne RGB camera data enables to get vegetation canopy heights (Bendig, 2015). A canopy height model (CHM) can be generated from two 3D point clouds where one with vegetation canopy (digital surface model – DSM) is subtracted from one without grown vegetation canopy (digital terrain model – DTM). The CHM derived from UAV-borne RGB data was successfully employed to model biomass of crops namely rice (Bendig et al., 2013), barley (Bendig et al., 2014), and wheat (Schirrmann et al., 2016) where mostly homogeneous canopy surfaces are presented due to single plant species. On the contrary, grassland represents a mixed canopy surface with various species. Biomass estimation of grassland using CHM derived from UAV-borne RGB images was also successfully applied in experimental grassland setups which showed significant results (Bareth et al., 2015; Possoch et al., 2016). Besides, UAV-borne multispectral and hyperspectral data have been used to model grassland biomass (Näsi et al., 2018; Lussem et al., 2019).

The nutritional quality parameters of grassland forage showed a relationship with the spectral reflectance in both lab-based and field-based measurements (Ali et al., 2016; Wachendorf et al., 2017). Forage quality parameters of grassland namely crude protein (CP), acid detergent fibre (ADF), and neutral detergent fibre (NDF) have been estimated frequently utilising field spectroscopy data (Biewer et al., 2009b; Skidmore et al., 2010; Pullanagari et al., 2012; Safari et al., 2016b). Similar to grassland biomass

modelling, UAV-borne RS data have been effectively employed to estimate grassland forage quality parameters only in experimental grassland setup (Capolupo et al., 2015; Näsi et al., 2018). The mentioned studies with UAV had utilised hyperspectral sensors which provide almost continuous spectral reflectance data from visible to infrared spectral regions of the electromagnetic spectrum.

UAV-borne RS data provide both high spatial and spectral resolution data, which is beneficial for classifying both native species and invasive species in grassland. One of the latest studies from Lu and He (2017), showed the potential of grassland species classification using UAV-borne images and object-based image analysis (OBIA). On the issue of invasive species mapping in grassland, so far, there has been no study that has utilised UAV-borne RS data. On the contrary, invasive species mapping with UAV-borne RS data was effectively applied to map *Fallopia japonica* (shrub) in flood plains (Martin et al., 2018), *Phragmites australis* (reed) in an estuary (Abeysinghe et al., 2019), and *Heracleum mantegazzianum* (perennial herb) in a riparian zone (Michez et al., 2016). Those studies employed both spectral and CHM data from UAV-borne RS and OBIA to obtain spatial coverage of invasive species.

Regardless of the method of RS data collection, empirical models are developed based on a statistical relationship between RS data and grassland biomass or forage quality values (Möckel, 2015). The model development employs different statistical modelling techniques. Simple linear regression with selected single or multiple RS variables (e.g. single wavebands, vegetation indices, canopy height metrics) and machine learning (ML) regression models using highly correlated RS variables (e.g. full-spectrum data) have been employed in both biomass and forage quality estimation modelling in grassland (Biewer et al., 2009a; Biewer et al., 2009b; Fricke and Wachendorf, 2013; Safari et al., 2016b; Möckel et al., 2017). Comparatively, OBIA was applied in species mapping, including invasive species because of the high spatial resolution characteristics of UAV-borne images. However, under the classification phase in OBIA, either rule-based classification (Lu and He, 2017) or ML classification (Michez et al., 2016; Martin et al., 2018; Abeysinghe et al., 2019) were utilised.

Chapter 2

Research motivations and objectives

As discussed in Chapter 1, up-to-date and accurate information of grasslands is crucial for fine-scale grassland monitoring. Several studies from the last 5-6 years demonstrated the applicability of UAV-borne RS data for different aspects of fine-scale grassland monitoring (i.e. biomass estimation, forage nutritional value estimation, species mapping). However, most of those studies focused on experimental grassland setups, which contained small grassland plots in a controlled environment. It is essential to check the potential of UAV-borne RS data in the experimental setup as a first step. Nevertheless, as a way forward, studies that apply UAV-borne RS data to monitor grasslands at a fine-scale (small extent with fine grain) to experience the proper variations in actual grassland field conditions (i.e. different fertiliser application systems, cutting regimes, conservation systems, different botanical composition, and, environmental conditions) are needed. Therefore, this study was conducted to fulfil these research gaps by addressing the following research question:

Can UAV-borne RS data be utilised for fine-scale grassland monitoring under real field conditions with the aspect of biomass, forage quality estimation and invasive species mapping?

This thesis consists of three distinct studies focusing on three different emphases (biomass estimation, forage nutritional value estimation, and invasive species mapping) of fine-scale grassland monitoring using UAV-borne RS data which have been culminated in three scientific manuscripts.

From three experiments, each study intended to accomplish specific sub-objectives which can lead to achieving the overall objective of the study. In the first study (Chapter 3), 3D point cloud-based CHM derived from UAV-borne RGB (red, green, blue) images were examined for grassland biomass estimation at three grassland fields with

different management intensities near Witzenhausen, Hesse, Germany. Furthermore, the performance of biomass estimation models based on UAV-borne RS data was compared with biomass models based on terrestrial laser scanner (TLS) data to understand the potential of UAV-borne 3D point cloud data for grassland biomass estimation. Examination of UAV-borne imaging spectroscopy data for estimating two important grassland forage quality parameters (crude protein - CP and acid detergent fibre - ADF) in a multitude of grasslands in Northern Hesse, Germany, was conducted in the second study (Chapter 4). Moreover, the developed forage quality estimation models were employed to generate CP, and ADF concentration maps to understand the spatio-temporal variation of forage quality values. The third study (Chapter 5) developed a repeatable and transferable workflow to map invasive *Lupinus polyphyllus* Lindl. (hereafter referred as lupine) coverage in semi-natural grassland using UAV-borne RGB and thermal data and OBIA. It was carried out at UNESCO biosphere reserve 'Rhön' where lupine has invaded many grasslands. Altogether, the three investigations were contributed to achieving the following general objective of the study:

- **To explore the applicability of UAV-borne RS data for fine-scale grassland monitoring under real field conditions**

From this perspective, specific sub-objectives of the study were:

i To investigate the usage of CHM derived from UAV-borne RGB 3D point cloud data for estimating grassland biomass (Chapter 3).

ii To explore the capability of UAV-borne hyperspectral data for selected grassland forage nutritional parameters, namely CP and ADF (Chapter 4).

iii To build a workflow to map invasive lupine using UAV-borne RS data and OBIA (Chapter 5).

iv To understand the limitations as well as measures to improve for fine-scale grassland monitoring using UAV-RS data (Chapter 3, 4, and 5).

Chapter 3

Evaluation of 3D point cloud-based models for the prediction of grassland biomass

Abstract

Farmers, as well as agronomists, are intrigued by efficient quantification of grassland biomass at field-scale. Canopy height model (CHM) based non-destructive grassland biomass estimation over a larger area has important advantages compared to destructive methods. 3D point clouds generated from remote sensing (RS) data offer a systematic methodology to derive CHM and estimate grassland biomass. This study evaluated 3D point clouds derived from a terrestrial laser scanner (TLS) and an unmanned aerial vehicle (UAV)-borne structure from motion (SFM) approach for grassland biomass estimation over three grasslands with different composition and management practice in northern Hesse, Germany. TLS data, UAV-borne images and reference biomass data were collected two days before each harvest from the selected grasslands in 2017. Three levels of linear empirical models (i.e. sampling date-specific, grassland-specific and global) were developed to estimate grasslands fresh and dry biomass using CHM derived from TLS and SFM 3D point clouds. The aforementioned three level models resulted in an average nRMSE of 17.2%, 25.3%, and 28.7% respectively for the grassland dry biomass estimation based on CHM from TLS data. Similarly, models based on CHM from SFM data estimated dry biomass with somewhat higher average nRMSE of 19.5%, 27.1%, and, 36.2% respectively. In general, models with 3D point clouds from UAV-borne SFM was slightly outperformed by models with TLS point cloud data. This study also identified that the utilisation of UAV-borne SFM devel-

oped digital terrain model as a reference layer to derive CHM could enhance the performance of the models with SFM data. Furthermore, the performance of the biomass estimation models was affected by both species richness and sward heterogeneity of the grasslands. Overall, these results disclosed the potential of 3D point cloud derived from RS for estimating field-scale grassland biomass.

Keywords : 3D point cloud; Canopy height model; Grassland biomass; Structure from motion; Terrestrial laser scanner; Unmanned aerial vehicle

3.1 Introduction

Biomass production is one of the most important ecosystem service measures in grassland ecosystems (Zielinska et al., 2015). Destructive sampling methods are commonly used to quantify grassland biomass. However, it is a labour-intensive and time-consuming work and the prediction accuracy can be very low when prediction is done for large areas (Catchpole and Wheelert, 1992). Non-destructive biomass sampling techniques can be advantageous in comparison to destructive methods, particularly for large areas. Plant structural properties such as grass sward height or tiller blade length derived from non-destructive sampling were employed for biomass prediction models and were based on allometric relationships (Santillan et al., 1979; Williamson et al., 1987).

Remote sensing (RS) as a contact-free sampling method can quantify both structural and biochemical properties of the vegetation, such as plant height, leaf area or chlorophyll content (Jones and Vaughan, 2010)). RS instruments can collect data over larger areas at different spatial and temporal scales in comparison to destructive sampling or field-based height measurements. Various RS derived variables have been utilised to develop empirical biomass models such as spectral vegetation indices, vegetation height, or leaf area index (Ali et al., 2016; Safari et al., 2016a; Wachendorf et al., 2017). Vegetation height derived from RS is generally the main input for empirical biomass prediction models in grassland monitoring. Three-dimensional (3D) data acquired from RS sensors is an efficient way to derive vegetation height (Jones and Vaughan, 2010; Fricke and Wachendorf, 2013).

RS-based 3D data acquisition techniques are categorised into active and passive techniques (Weinmann, 2016). Active techniques directly measure the distance from the object to the sensor while passive techniques usually acquire 2D images which are then further processed to obtain distance measurements. Light detection and ranging

(LiDAR) is the most renowned active technique and the most popular passive 3D data acquisition technique is stereoscopic digital photogrammetry. Technological advancements introduced new state-of-the-art passive methods such as structure from motion (SFM) to derive 3D measurements from RS imagery.

LiDAR sensors emit coherent light and receive the reflected energy from the distant object. The distance between sensor and object is calculated based on the time of flight and finally the 3D coordinates of the object's point with respect to the sensor's location are calculated (Heritage and Large, 2009). A terrestrial laser scanner (TLS) is a ground-based static LiDAR sensor. The height or volume derived from the TLS point cloud data is utilised to estimate low vegetation biomass in shrub-covered areas (Glenn et al., 2015; Greaves et al., 2015), agricultural crops (Eitel et al., 2014; Tilly et al., 2014a; Tilly et al., 2014b), as well as in grasslands (Cooper et al., 2017; Wallace et al., 2017).

Structure from motion is a computer vision technology that generates a 3D dense point cloud from overlapping 2D images. The dense cloud is derived from repetitive bundle adjustment of the multiple overlapping images and precise image matching techniques (Snavely et al., 2006). The overlapping images are generally taken from the moving camera mounted on a, for example, unmanned aerial vehicle (UAV). Using a UAV for the SFM method has advantages over terrestrial-based techniques, as it allows systematic acquisition of images over large areas with the same procedure. SFM derived object height has been utilised in tree structure assessments (Hesse, 2014; Morgenroth and Gomez, 2014) as well as in agricultural monitoring (Bendig et al., 2013; Bendig et al., 2014; Holman et al., 2016).

To our knowledge, there exist only two studies that compared grassland biomass prediction using SFM and TLS derived data. Wallace et al. (2017) and Cooper et al. (2017) estimated pasture and *Bromus inermis* grassland biomass, respectively, using TLS and SFM derived heights. Both the SFM and TLS data models had similar potentials to estimate grassland biomass. However, in both studies close-range images were taken by humans and both methods monitored only small areas (~1 m^2 plots). While such methods do not allow the biomass prediction on large areas, the SFM approach based on UAVs do have much less constraints. SFM was applied to images from large barley (Bendig et al., 2014) and rice fields (Bendig et al., 2013) and provided accurate biomass predictions.

So far, there has been no study that examined the performance of SFM with UAV-borne images compared to other 3D RS methods for grassland biomass prediction. Therefore, this study compares SFM with TLS based methods for developing empirical models for biomass prediction from grasslands differing in terms of botanical composition and

management practises. We hypothesize that the canopy height model calculated from SFM 3D point clouds based on UAV-borne images can predict grassland biomass with similar accuracy as with 3D point clouds based on TLS data. Thus, the objectives of this study are;

- To develop empirical models to estimate grassland biomass from 3D point clouds derived from SFM and TLS methods
- To compare the performance of biomass prediction models based on SFM and TLS data
- To assess the model accuracy for different grassland types

3.2 Material and methods

3.2.1 Study area

The study was conducted on three grasslands with different management practise and species composition. All grasslands were located in the Werra-Meißner district in Hesse, Germany. The location of the grasslands is shown in Figure 3.1.

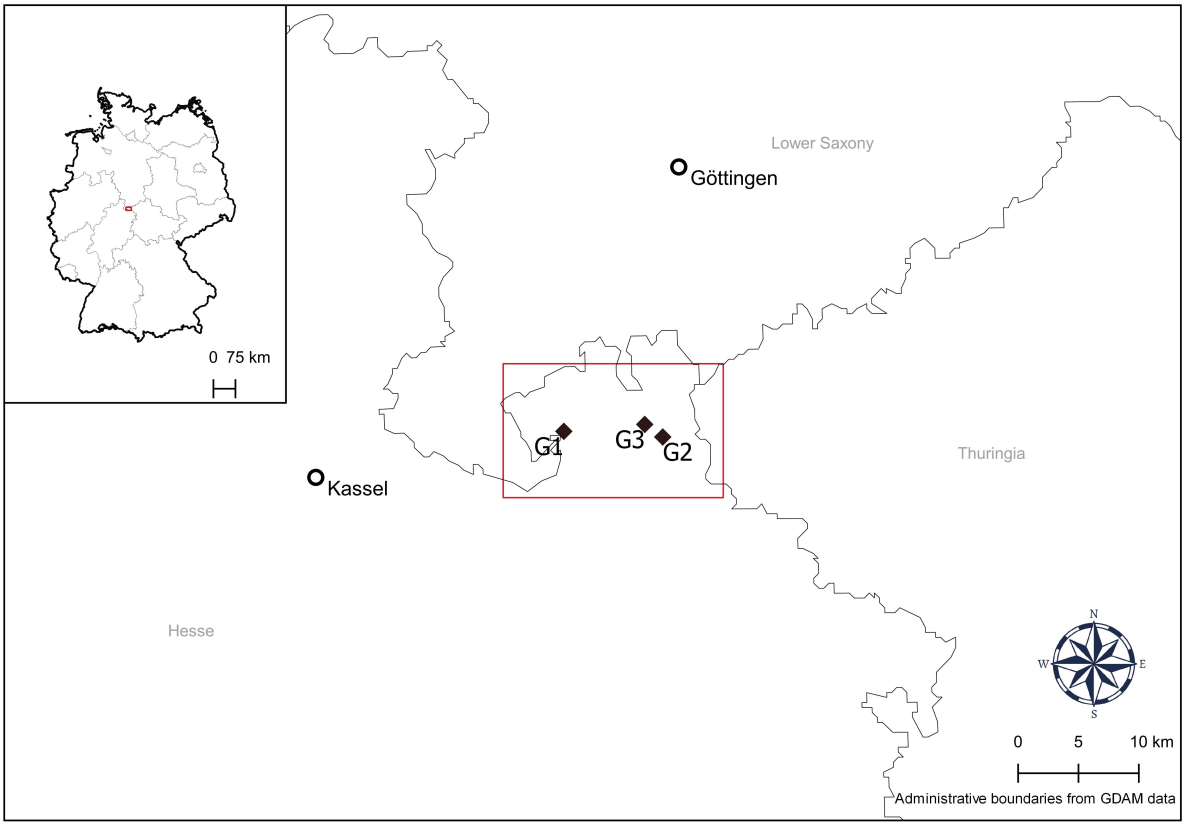

Figure 3.1: The map of the study area and selected grasslands

Grassland one (G1) was an intensively managed temporal grassland established on a former arable field in 2013. The field was situated on a gentle slope at an altitude of 270 m a.s.l. *Lollium multiforum* and *Trifolium repens* were the dominant species and species diversity (8 species) and spatial variability of the vegetation was very low. It was cut four times per year and nitrogen fertiliser was applied with 80 kg ha-1 year-1. G2 was a leniently managed permanent grassland, which was also cut four times but was not fertilised in 2017. It was located at 200 m a.s.l. The sward was more heterogeneous with 29 species and classified as an *Arrhenatheretum elatioris* meadow. G3 was situated in a flat land next to a river. It was an old permanent grassland with only two cuts per year and no N fertiliser application. The sward comprised 30 species and was classified as a *Plantagini lanceolatae-Festucetum rubrae* meadow. Based on the Bray-Curtis index value (McCune and Grace, 2002), which describes the species dissimilarity between sites, G3 obtained highest index values (0.62), equivalent to lowest species dissimilarity, followed by G2 (0.47) and G1 (0.36). In each grassland a 25 m by 50 m rectangle plot (~1250 m^2) was selected as the study plot. 18 randomly distributed sub-plots (1 m^2 each) were established within each study plot to conduct destructive biomass samplings and species composition surveys. Sub plot location was generated using QGIS programme and each sub plot is minimum 6 m away from the nearest other sub plot.

3.2.2 Data collection

TLS data and UAV-borne images were collected in each study plot two days before mowing between May and October 2017. In total four data sets for G1, three data sets for G2, and one data set for G3 were collected. The dates and connected harvest number for each sampling are described in Table 3.1. The data for the second cut in G2 and G3 could not be collected.

Table 3.1: Sampling dates and connected harvest numbers of grasslands

Grassland	Date	Harvest
G1	15th May	First cut (H1)
	23rd June	Second cut (H2)
	14th August	Third cut (H3)
	29th September	Fourth cut (H4)
G2	14th May	First cut (H1)
	15th August	Third cut (H3)
	30th September	Fourth cut (H4)
G3	06th June	First cut (H1)

TLS data

A Leica ScanStation P30 (Leica Geosystem, Switzerland) TLS was used. The TLS is equipped with a 1550 nm near-infrared wavelength sensor, which has a three-dimension accuracy of 3 mm at a distance of 50 m. It can scan 1 million points per second with a field of view of 360° horizontal and 290° vertical (Leica Geosystems, 2017).

The TLS data collection was conducted with the same procedure in all plots and at all harvest dates. Six scans were taken in each study plot to obtain equal density point clouds for the whole area and to avoid shadow effects within the grassland canopy. Three reflective markers were utilised at each scan for mosaicking the single point clouds. The positions of the markers were measured using a Leica real time kinematic (RTK) global navigation satellite system (GNSS) with an accuracy of 2 cm. In addition, one TLS data set was gathered for each plot one day after mowing to generate a digital terrain model (DTM).

UAV-borne images

A DJI-Phantom III quadcopter with an inbuilt consumer grade camera (DJI, China) was used to obtain UAV-borne images. The camera (FC300S) captures 12-megapixel images in true colour (R: Red, G: Green, B: Blue). The UAV was flown over the study plot using a pre-designed flight plan which had two flight grids with 90° orientation difference. The UAV flight grids were designed using Pix4D capture app for android (Pix4D, Switzerland). To ensure an image overlap of 80% for both sides and forward, the camera was set to trigger automatically considering the flying altitude of 25 m and flying speed of 3 ms^{-1}. Markers were used as ground control points (GCPs), which

were installed in the four corners of the rectangle plot prior to the flight session. The position data for the GCPs were collected after the flight session using RTK GNSS.

Biomass smapling

The selected 1 m^2 sampling areas were used at every sampling in each study plot. After the sensory data collection, two corners of each subplot were staked out on the ground using RTK GNSS and the biomass was clipped at 5 cm above ground level, which is the common stubble height in practical mowing. The sample was weighted in the field (fresh biomass, FB) and a sub-sample was dried at 105° C for 48 hours to calculate the dry matter content, which was used for calculating dry biomass (DB).

3.2.3 Data processing

Canopy height modelling based on TLS data

The TLS data was processed using Leica Cyclone 3D (Leica Geosystem, Switzerland) point cloud processing software. The six separate scan measurements for each study plot were merged using marker locations. The merged scan data was geo-referenced using the measured GPS coordinates, cropped to the boundary of the study plot and finally exported as a 3D point cloud. The scan data recorded after harvest was processed similarly and point clouds were exported for each plot. Post-harvest point clouds were binned to a raster (Petras et al., 2018) and minimum z values of all points falling within each cell was considered as equal to ground level . To identify the optimum raster cell size for the binned raster, cell size was varied from 1 cm to 10 cm in 10 steps. The raster cell size resulting in the lowest no-data cell percentage was identified as the optimum cell size for binning, which was 10 cm (1.1% of no-data cells). The binned raster from post-harvest data was considered as the DTM in this study. Z values of the DTM were subtracted from respective z values of the pre-harvest point cloud based on x and y coordinates to generate a point cloud with canopy height model (CHM, see Equation 3.1).

$$CHM_{x,y} = Z_{x,y} - DTM_{x,y} \tag{3.1}$$

Canopy height modelling based on SFM data

The acquired UAV-borne images were processed with the Agisoft PhotoScan Professional version 1.3.4 (64 bit) software (Agisoft LLC, Russia) to generate a point cloud. To this end geo-tagged images from one UAV flight session were aligned using tie points

in the overlapping images. In this step sparse point clouds were produced which only contained matching points and which had to be geo-referenced based on the geotag data from the images. However, as the geo-reference accuracy was not adequate for precise analysis, GCP data was used for geo-referencing the points (Figure 3.2). The resulting point cloud was further processed to build a dense point cloud containing all image points of the study area. In this step, the quality parameter was set as high and filtering parameter was set to mild to obtain many points and to reduce possible data loss (Figure 3.2).

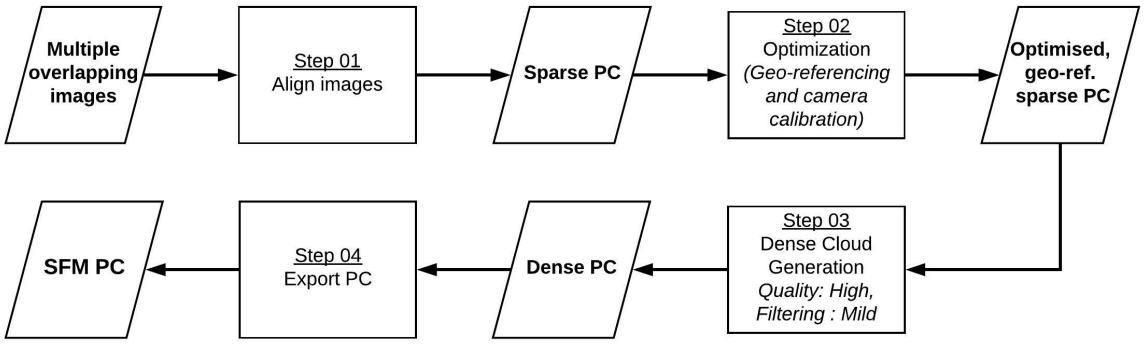

Figure 3.2: SFM data processing chain using the Agisoft PhotoScan software (PC: point cloud)

Similar to the TLS data processing, CHM based on SFM data was obtained by subtracting z values of the DTM from the dense point cloud z values based on x and y location (Equation 3.1).

Biomass modelling

Canopy height model for each subplot was extracted for the TLS and SFM datasets separately. CHM statistics for each subplot were computed comprising minimum, maximum, arithmetic mean, median, standard deviation, count, and 25^{th}, 75^{th}, 90^{th} and 95^{th} percentiles.

The grassland biomass was modelled for each sampling in each study plot using SFM and TLS data exclusively. First the Pearson correlation coefficient (r) was calculated for each CHM statistic parameter from both SFM and TLS data. Ordinary least squares linear regression models with 5-fold cross validation were built for the parameter with highest r value both for FB and DB. The performance of the linear regression model was evaluated using the adjusted coefficient of determination (adj.R^2) value, root mean square value (RMSE) (Equation 3.2) and normalised RMSE (nRMSE) value (Equation 3.3). All analyses were carried out using R software version 3.4.1.

$$RMSE = \sqrt{\frac{1}{18}\sum_{i=1}^{18}(measured\ yield - estimated\ yield)^2} \quad (3.2)$$

$$nRMSE = \frac{RMSE}{mean\ measured\ yield} \times 100 \quad (3.3)$$

3.3 Results

3.3.1 Biomass reference data

Average dry matter content of the grassland biomass was 22.5 %, 27.1 %, and, 25.4 % for G1, G2, and G3, respectively (Table 3.2). For G1 the average FB was 22.3 t ha^{-1} and DB was 5.1 t ha^{-1}. Without the missing data from H2 average FB was 10.6 t ha^{-1} and DB was 2.8 t ha^{-1} for G2. The only harvest obtained from G3 was 5.8 t ha^{-1} and 1.5 t ha^{-1} for FB and DB respectively.

Table 3.2: Mean, minimum (Min), maximum (Max) values and standard deviations (SD) of measured grassland biomass (FB: fresh biomass, DB: dry biomass)

Grass-land	Harvest number	FB (t ha^{-1})			DB (t ha^{-1})		
		Min	Mean±SD	Max	Min	Mean±SD	Max
G1	H1	2.9	5.6±2.0	11.4	0.7	1.3±0.4	2.2
	H2	5.4	8.6±1.9	12.1	1.2	2.0±0.4	2.6
	H3	1.4	4.5±2.3	9.5	0.4	1.0±0.4	1.9
	H4	1.1	3.6±1.7	6.6	0.3	0.8±0.3	1.3
G2	H1	3.0	4.7±1.0	6.8	0.8	1.2±0.2	1.6
	H3	2.4	4.7±1.1	6.8	0.7	1.3±0.2	1.7
	H4	0.7	1.2±0.3	1.9	0.2	0.3±0.1	0.5
G3	H1	4.3	5.8±1.1	8.3	0.9	1.5±0.3	2.2

3.3.2 Canopy height model as derived from point clouds

Canopy height model based on TLS ranged from 0.10 to 0.36 m, whereas values based on SFM were somewhat lower (0.04 to 0.27 m) (Table 3.3). Point densities of clouds fluctuated substantially among harvests for both methods. Although CHM calculation was similar for TSL and SFM, values of the first harvest of G2 exceeded the georeference $RMSE_{xyz}$ threshold which was 0.20 m. Therefore, CHM from this sampling

were not considered in this study. SFM based point densities from G1 were considerably smaller than from G2 and G3. Exemplary CHM derived from both TLS and SFM for a subplot at the third harvest of G2 is shown in Figure 3.3.

Table 3.3: Summary statistics of point density and canopy height model (CHM) as derived from TLS and SFM measurements (M: mean, SD: standard deviation, NA: not assessed)

Grass-land	Harvest number	TLS		SFM	
		Point density (m^{-2})	CHM (m) (M±SD)	Point density (m^{-2})	CHM (m) (M±SD)
G1	H1	15260	0.19±0.07	2666	0.27±0.14
	H2	16002	0.31±0.11	2048	0.22±0.06
	H3	8615	0.15±0.07	2095	0.07±0.04
	H4	15920	0.10±0.15	1012	0.04±0.02
G2	H1	5175	0.27±0.07	NA	NA
	H3	10335	0.22±0.08	10729	0.24±0.05
	H4	19151	0.11±0.04	13627	0.06±0.04
G3	H1	7446	0.36±0.16	8088	0.39±0.09

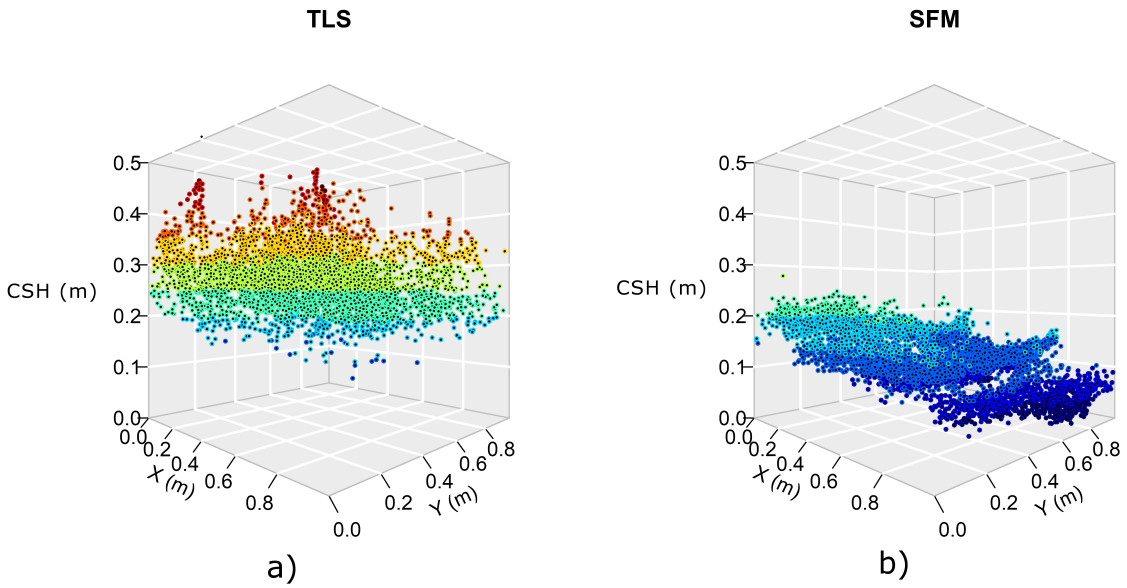

Figure 3.3: Canopy height model based on TLS (a) and SFM (b) point clouds for one 1 m^2-subplot in the third harvest of G2

3.3.3 Biomass prediction

Prior to the biomass calculation correlations between statistic parameters from both TLS and SFM based CHM and the measured biomass (FB and DB) were evaluated. For TLS the 25th percentile (p25) of CHM values obtained the highest correlation coefficient (r) both for FB and DB in five of eight harvests (G1-H3, G2-H1, G2-H3, G2-H4, and, G3-H1) (average r = 0.7). Based on these results, the p25 value was identified as the most appropriate parameter for biomass calculation with TLS data. Correlation analysis between the SFM based CHM parameters and the biomass produced more heterogeneous results, but overall the 75th percentile achieved the strongest explanatory power (average r = 0.63). Consequently, p75 values were used to estimate biomass from SFM based CHMs from all harvests.

Sampling date-specific biomass prediction

Biomass prediction models based on TLS data for G1 provided the highest adjusted coefficient of determination (adj.R^2) and the lowest normalised RMSE (nRMSE). However, for the second harvest of G1 no significant relationship between the TLS derived p25 height and both the FB and the DB was found. The three regression models developed for G2 had an average adj.R^2 of 0.46 ($p < 0.01$) with an average nRMSE of 18.7 % for the prediction of FB. In contrast, the prediction of DB for G2 showed an adj.R^2 of 0.34, 0.60, and 0.25 ($p < 0.005$) for H1, H3, and H4, respectively. The model for G3 had the lowest prediction accuracy of all three grasslands with an adj.R^2 of 0.35 ($p < 0.05$) and a nRMSE of 18.4 %. The model results based on TLS and SFM data are shown in Table 3.4.

Table 3.4: Regression statistics for sampling date-specific relationships between measured fresh (FB) and dry biomass (DB) for canopy height model based on TLS and SFM. (NA: not assessed)

Grass-land	Harvest number	TLS				SFM			
		FB		DB		FB		DB	
		adj.R^2	nRMSE	adj.R^2	nRMSE	adj.R^2	nRMSE	adj.R^2	nRMSE
G1	H1	0.60^{***}	21.7 %	0.59^{***}	17.8 %	0.56^{***}	22.7 %	0.53^{***}	18.8 %
	H2	0.03^{ns}	21.2 %	0.05^{ns}	25.9 %	$0.14^{\bullet}$	19.2 %	$0.14^{\bullet}$	15.9 %
	H3	0.78^{***}	22.3 %	0.83^{***}	15.0 %	0.58^{***}	31.0 %	0.62^{***}	22.7 %
	H4	0.58^{***}	29.1 %	0.58^{***}	24.2 %	0.57^{***}	29.3 %	0.55^{***}	24.9 %
G2	H1	0.46^{**}	15. 0 %	0.34^{**}	16.0 %	NA	NA	NA	NA
	H3	0.49^{**}	15.6 %	0.60^{***}	11.6 %	0.29^{*}	18.4 %	0.40^{**}	14.1 %
	H4	0.42^{**}	20.1 %	0.25^{*}	19.5 %	0.01^{ns}	26.3 %	0.06^{ns}	21.7 %
G3	H1	0.23^{*}	15.3 %	0.35^{*}	16.3 %	$0.10^{\bullet}$	16.5 %	0.15^{*}	18.6 %

^{ns} - not significant

$^{\bullet}$ - significant at $p < 0.1$

* - significant at $p < 0.05$

** - significant at $p < 0.01$

*** - significant at $p < 0.001$

Similar to the TLS results SFM based prediction of biomass was more accurate for G1 than for the other grasslands. Except for the second harvest average adj.R^2 was 0.57. H2 models both for FB and DB achieved significant weaker accuracies of adj.R^2 = 0.14. For G2 only H3 gave significant results with an adj.R^2 of 0.29 and 0.40 for FB and DB respectively. No strong relationship between biomass and SFM based CHM was found for G3.

Grassland-specific biomass prediction

There were strong and statistically significant linear relationships between TLS and SFM derived CHM and field measured biomass when analysed separately for G1 and G2. Generally, relationships for DB showed a more stable trend than for FB. Correlations between TLS and DB resulted in adj.R^2 0.72 for G1 and 0.70 for G2, whereas correlations with SFM were weaker for G1 (adj.R^2 0.49) and better for G2 (adj.R^2 0.86). As SFM covered a wider range in CHM, slopes of SFM regression functions were generally lower than with TLS data. Observed and predicted biomass plots from each model were presented in Figure 3.4.

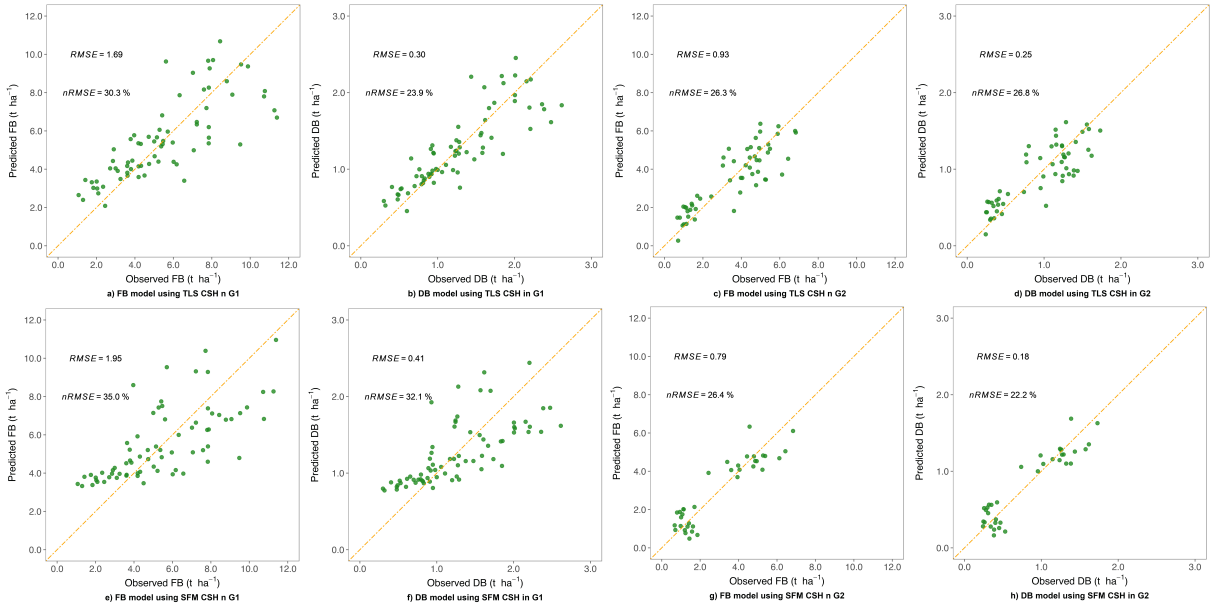

Figure 3.4: Relationship between observed and predicted biomass (FB and DB) from TLS- (a-d) and SFM- (e-h) based canopy heights for the G1 (a, b, e, f) and G2 (c, d, g, h) grasslands. (broken line is 1:1 relationship)

Global grassland biomass prediction

Global regression models were developed to predict biomass including SFM and TLS data from all samplings of grasslands G1, G2, and G3 (Figure 3.5). Like in grassland specific models, the TLS based prediction model (adj.R^2 = 0.61) for DB performed better than for FB (adj.R^2 = 0.48, $p < 0.001$). Global models based on SFM data performed slightly weaker with adj.R^2 = 0.45 for DB and adj.R^2 = 0.35 for FB.

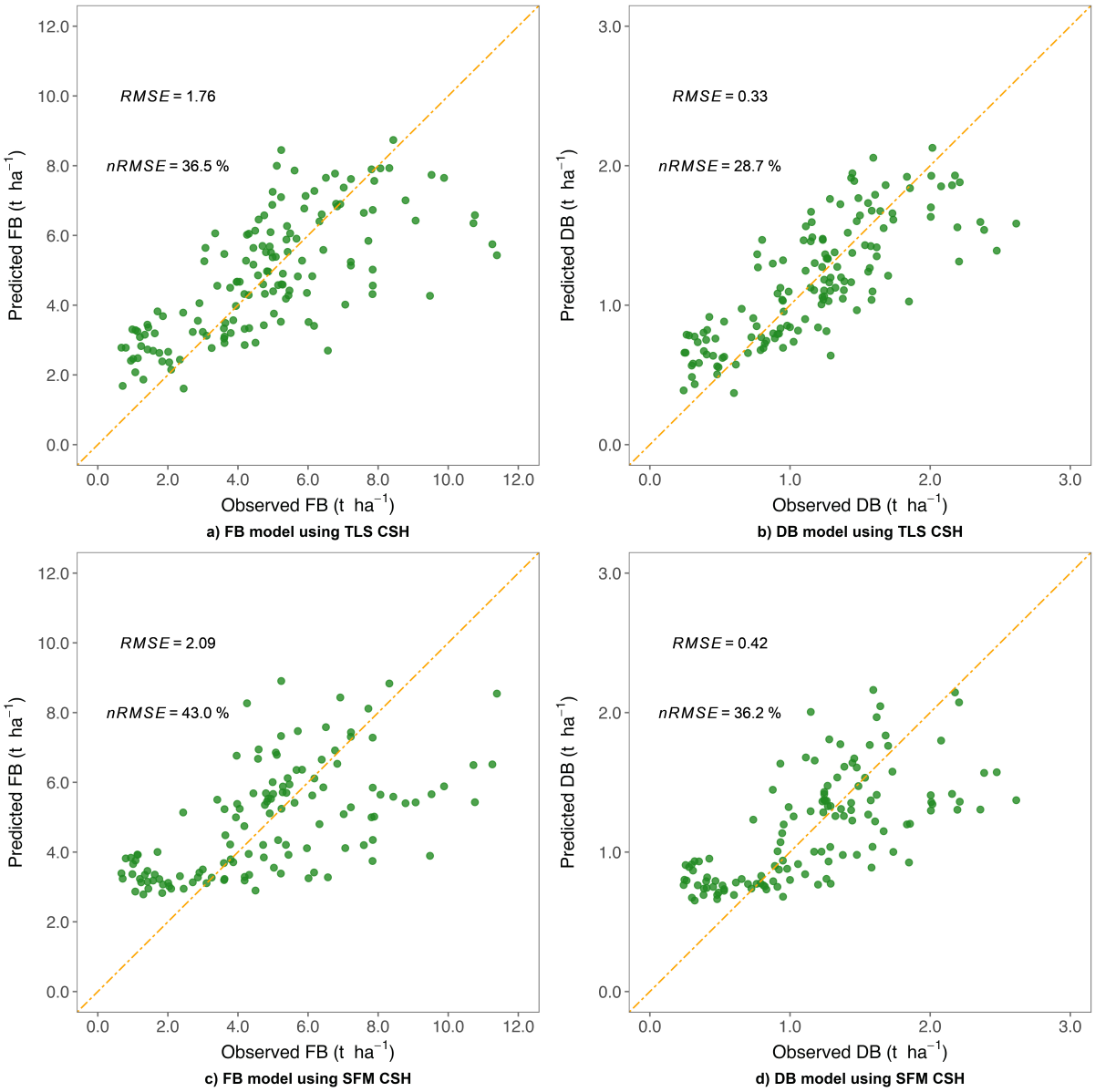

Figure 3.5: Relationships between measured and predicted biomass (FB and DB) from TLS (a, b) and SFM (c, d) based canopy heights global models for grasslands. (broken line is 1:1 relationship)

3.4 Discussion

The results of this study showed that SFM data based on UAV-borne imagery has the capability to assess grassland CHM with a similar accuracy as with TLS data. Both TLS and SFM provided similar CHM distribution for each harvest date and grassland type, therefore, both approaches can be assumed a sound basis for the prediction of grassland biomass.

The first goal of this study was to develop biomass prediction models based on SFM and TLS data. The linear empirical models with cross validation were developed to

predict grassland biomass (FB and DB) from both data sources (SFM and TLS) at three different levels, which were i) harvest-specific, ii) grassland-specific and iii) global models including all data. While TLS based models predicted DB with an average nRMSE of 17.2 %, 25.3 % and 28.7 %, nRMSE values for SFM were bigger (19.5 %, 27.1 % and 36.2 %, respectively) at the three before-mentioned levels. The results for SFM are similar to those from two other studies that utilised close-range images with subsequent SFM analysis in pastures (nRMSE 21.7 %) and Bromus inermis grasslands (nRMSE 28.0 %) (Cooper et al., 2017; Wallace et al., 2017). Li et al. (2017) showed good results for non-linear models including a multitude of statistical variables derived from CHM contrary to our study, where only the optimal parameter was used. However, this procedure was tested for shrub biomass prediction with airborne LiDAR data, which is not readily comparable with our experimental setting. In any case, such procedure would largely increase the complexity of modelling compared to our simple linear modelling approach.

Possible reasons for the different performance of TLS and SFM based prediction models may be a) variation of the viewing geometry of the two sensors, and b) effects of the utilised DTM and geo-referencing procedure of the point clouds.

Considering a) The lateral perception and the high resolution (in our study 3 mm point distance at a range of 10 m) of the TLS was shown to capture more of the isolated elements of the canopy top, i.e. single grass blades and seed heads (Cooper et al., 2017). Contrary, UAV-borne photo images provide an aerial perception of the grasslands and due to the dense vegetation canopy do not collect data from below the canopy surface level. Depth filtering and multi-view image processing during SFM processing further reduced the information from lower canopy levels (Wallace et al., 2017). Though the spatial resolution of our UAV-borne images was 1-2 cm due to the low flight altitude of the UAV, it did not allow both the separation of distinctive canopy elements in the image and the collection of any information about the density of biomass below the canopy surface. Flying at a lower altitude would certainly increase the spatial resolution of images, but would at the same time reduce the area to be covered.

Considering b) The accuracy of CHM prediction based on SFM data was shown to be substantially affected by the DTM and the geo-referencing step in the SFM procedure (Shi et al., 2016). In our study, the DTM from the post-harvest TLS data were employed for both the TLS and SFM based models. Therefore, misalignment between the DTM and the SFM point cloud may have occurred. DTM generation derived directly from the UAV-borne images may be advantageous, as was shown for semi-desert grassland without using post-harvest data (Cunliffe et al., 2016), where ground point classifica-

tion was utilised to derive the DTM from the SFM data. However, that methodology did not work under our conditions, as canopies of temperate grasslands are too dense to allow a sound ground point identification. In our study the SFM point cloud was geo-referenced using four GCPs, while the TLS point cloud was geo-referenced with six black-white targets. Using only four GCPs, which is the minimum for proper geo-referencing, limited somewhat the possibility to select clearly visible GCPs and to reject low accurate GCPs in the UAV-borne images (Wijesingha, 2016). Therefore, increasing the number of GCPs may enhance the precision of SFM data and improve the model performance. Moreover, the study plots that were utilised in this study provided very low biomass yield in the year of the experiment due to frost in late spring and extended dry spells in summer. Total annual DB of intensively managed grassland is around 8 t ha^{-1} (Statistisches Bundesamt, 2018). However, the temporal grassland in this study (G1) produced only 5.1 t DB/ha per year. Similarly, the two permanent grasslands delivered lower DB (average 3.0 t ha^{-1} per year) than what is normally expected for permanent grassland's DB in North Hesse . Therefore, as prediction accuracy is usually low at low levels of biomass, the TLS and SFM derived model results cannot be extrapolated to highly productive grasslands.

The third objective of this study was to assess the biomass prediction model accuracy for different grassland types. The data suggest that the performance of the empirical models decreased with the increase of species richness and the related spatial heterogeneity of grassland for both SFM and TLS data. Biomass prediction for the species-poor and homogeneous grassland (G1) showed higher correlations than for the two other grasslands (G2 and G3), which were species-rich, heterogeneous grasslands. Consequently, global models for grassland biomass did not provide a convincing predictive ability. These results imply that exclusive use of CHM is not informative enough to predict the biomass in species-rich, heterogeneous grassland, which was also suggested by Fricke and Wachendorf (2013) and Möckel et al. (2017).

The hypothesis, that CHM derived from SFM processed UAV-borne images can predict the biomass with similar accuracy as with TLS derived CHM, could be proven based on the examined grasslands. It was found that SFM derived CHM can predict grassland biomass more easily, when models were developed specifically for the grasslands. A better understanding of measures to minimise possible shortcomings of acquiring and processing of SFM data can lead to an improved UAV-borne biomass assessment as a low-cost precision agriculture method for temperate grasslands, like it was shown for a range of arable crops (i.e. rice, barley, maize) (Bendig et al., 2013; Bendig et al., 2014; Malambo et al., 2018).

3.5 Conclusions

Accurate and timely quantification of biomass is an important information in sustainable grassland management. The results of this study demonstrate that FB and DB of grasslands can be predicted using the CHM derived from SFM and TLS point cloud data and that prediction accuracy in intensively managed species-poor grassland is higher than in divers and heterogeneous canopies. However, SFM exhibited a slightly worse performance than TLS did. This study identified measures that can minimise the prediction errors of the UAV-borne images with SFM. In contrast to pure-species, arable crops, the complex structures in grassland lowers biomass prediction accuracy if CHM is used exclusively. The combination of CHM and spectral data from UAV-borne images is seen as a promising way for future research.

The content of Chapter 3 has not been changed from the original published version.

Wijesingha, J., Moeckel, T., Hensgen, F., & Wachendorf, M. (2019). Evaluation of 3D point cloud-based models for the prediction of grassland biomass. International Journal of Applied Earth Observation and Geoinformation, 78(June), 352–359, 10.1016/J.JAG.2018.10.006.

(Received: 24 May 2018; Received in revised form: 9 October 2018; Accepted: 10 October 2018; Available online: 17 October 2018)

Chapter 4

Predicting forage quality of grasslands using UAV-borne imaging spectroscopy

Abstract

The timely knowledge of forage quality of grasslands is vital for matching the demands in animal feeding. Remote sensing (RS) is a promising tool for estimating field-scale forage quality compared with traditional methods, which usually do not provide equally detailed information. However, the applicability of RS prediction models depends on the variability of the underlying calibration data, which can be brought about by the inclusion of a multitude of grassland types and management practices in the model development. Major aims of this study were (i) to build forage quality estimation models for multiple grassland types based on an unmanned aerial vehicle (UAV)-borne imaging spectroscopy and (ii) to generate forage quality distribution maps using the best models obtained. The study examined data from eight grasslands in northern Hesse, Germany, which largely differed in terms of vegetation type and cutting regime. The UAV with a hyperspectral camera on board was utilised to acquire spectral images from the grasslands, and crude protein (CP) and acid detergent fibre (ADF) concentration of the forage was assessed at each cut. Five predictive modelling regression algorithms were applied to develop quality estimation models. Further, grassland forage quality distribution maps were created using the best models developed. The normalised spectral reflectance data showed the strongest relationship with both CP and ADF concentration. From all predictive algorithms, support vector regression provided the highest precision and accuracy for CP estimation (median normalised root mean square error prediction (nRMSEp) = 10.6 %), while cubist regression model proved best for ADF estimation (median nRMSEp = 13.4 %). The maps gener-

ated for both CP and ADF showed a distinct spatial variation in forage quality values for the different grasslands and cutting regimes. Overall, the results disclose that UAV-borne imaging spectroscopy, in combination with predictive modelling, provides a promising tool for accurate forage quality estimation of multiple grasslands.

Keywords : unmanned aerial vehicle; hyperspectral; grassland; crude protein; acid detergent fibre; predictive modelling

4.1 Introduction

In Europe, approximately 30 % to 35 % of the agricultural area consists of grasslands (Huyghe et al., 2014). Mainly permanent grasslands are incredibly variable in species composition, biodiversity, and management practices, as well as in productivity (Lesschen et al., 2014). Food provisions as forage for ruminants and herbivores and as biomass substrate for energy production are the most comprehensive ecosystem services from grasslands. There exists a multitude of destructive and non-destructive methods to measure or estimate the production and quality of the forage (Heather and Nature, 1999; t'Mannetje and Jones, 2000; Wachendorf, 2018). Timely and accurate information about forage quality is essential to match available feed on offer with animals' demand.

Usually, farmers use visual criteria to evaluate forage quality, such as the plants' phenological stage, leafiness, or colour. Additionally, lab-based chemical analysis and near-infrared reflectance spectroscopy (NIRS) are utilised by agronomists to evaluate forage quality (Horrocks and Vallentine, 1999). Lab-based methods are used to determine chemical forage components that relate to the digestibility of the forage. Acid detergent fibre (ADF), which represents cellulose, lignin, and silica, is an important parameter that is negatively correlated with forage digestibility (Horrocks and Vallentine, 1999; Gibson, 2009). The protein concentration of forages is another parameter essential for the creation of adequate fodder rations. Protein consists mainly of amino acids, which are fundamental elements of all cells and tissues. Protein is an essential component of ruminant nutrition and provides nitrogen for ruminants' metabolism and production of milk and meat (Frame and Laidlaw, 2011).

Remote sensing (RS) is a non-destructive method for estimating grassland biomass and forage quality (Numata, 2011; Möckel, 2015; Wachendorf et al., 2017). From satellite RS to field spectroscopy and from optical RS to synthetic aperture radar were employed for forage quality monitoring and mapping (Ali et al., 2016; Wachendorf, 2018). A lit-

erature review on RS based forage quality estimation studies published between 2004 and 2018 shows that more than 60 % of studies (21 out of a total of 31 reviewed studies) have utilised field spectroscopy. Often, point-level spectral reflectance data from visible to short-wave infrared regions of the electromagnetic spectrum are collected in field spectroscopy (Milton, 1987). Crude protein (CP), nitrogen (N), neutral detergent fibre (NDF), and ADF are the most common forage quality parameters that have been estimated using field spectroscopy data for different grasslands with significant accuracy (Mutanga et al., 2004; Biewer et al., 2009b; Pullanagari et al., 2012; Ramoelo et al., 2013b; Safari et al., 2016a).

Point-level data observation is laborious and challenging to collect over large areas. The application of imaging spectroscopy (also known as hyperspectral imaging) mounted on higher-altitude platforms (i.e., airborne, space-borne) could overcome these disadvantages. Imaging spectroscopy is the "acquisition of images in many (hundreds) narrow contiguous spectral bands" (Goetz et al., 1985). Instead of point observation, imaging spectroscopy provides a two-dimensional image with each pixel containing spectral reflectance data. Airborne imaging spectroscopy has been utilised for forage quality mapping in grassland (Skidmore et al., 2010; Knox et al., 2011; Pullanagari et al., 2012), but conducting manned airborne mission requires extensive well-ahead planning. On the contrary, an unmanned aerial vehicle (UAV) allows the collection of low altitude images over large areas with less effort and relatively low costs.

UAV as an RS platform for both multi- and hyperspectral imaging has been frequently applied for field-scale vegetation mapping in the last few years owing to miniature sensor availability and the advancement of computer vision techniques. Concerning grassland monitoring and mapping, the UAV-borne RS has been employed mainly for grassland biomass estimation with multispectral imaging (Viljanen et al., 2018), imaging spectroscopy (Capolupo et al., 2015; Näsi et al., 2018), and consumer-grade cameras (Grüner et al., 2019; Wijesingha et al., 2019). Only two studies that utilised UAV-borne imaging spectroscopy data for forage quality estimation are known to the authors (Capolupo et al., 2015; Näsi et al., 2018), and the results showed that UAV-borne imaging spectroscopy data could accurately predict forage quality parameters. However, those studies have only focused on experimental plots, and no study has evaluated the UAV-borne imaging spectroscopy for forage quality estimation under practical field conditions including different grassland types in terms of plant community composition and with a wide range of management practices.

Except for the spectral data collection method, the model development for forage quality estimation employed various techniques. In general, forage quality modelling

utilised actual reflectance data or transformed spectral reflectance data, among which normalised spectra, derivative spectra, and continuum removal spectra. The most frequently applied statistical modelling method is the linear regression (simple linear, step-wise linear) with selected highly correlated spectral features, such as wavebands (Skidmore et al., 2010; Durante et al., 2014), normalised difference spectral indices (NDSIs) (Safari et al., 2016a; Castro and Garbulsky, 2018; Näsi et al., 2018), spectral ratios (SRs) (Biewer et al., 2009b; Zengeya et al., 2012), and other well-known vegetation indices (e.g., NDVI, SAVI, NDRE) (Ramoelo et al., 2013b; Viljanen et al., 2018). Predictive modelling (also known as machine learning) algorithms, such as partial least squares regression (PLSR) (Starks et al., 2004; Pullanagari et al., 2012; Ramoelo et al., 2013a; Durante et al., 2014; Safari et al., 2016b), random forest regression (RFR) (Singh et al., 2017; Näsi et al., 2018; Pullanagari et al., 2018), and artificial neural network (Mutanga and Skidmore, 2004; Skidmore et al., 2010; Knox et al., 2011), were employed to estimate forage quality parameters using highly correlated spectral reflectance data. Predictive modelling algorithms frequently enhanced the predictive capability compared with the simpler linear regression models (Näsi et al., 2018; Pullanagari et al., 2018). Moreover, there are several other algorithms in predictive modelling, namely, Gaussian processing regression (GPR), support vector regression (SVR), and cubist regression (CBR), that have not been examined with spectral data to estimate forage quality.

Typically, the models developed to estimate forage quality using spectral data are restricted to single grassland types. Consequently, the transferability of the models to other grassland types is limited due to the low variability of the underlying training data. Therefore, a general model that can estimate forage quality parameters, irrespective of the grassland type, would be a preferable solution. Thus, we hypothesise that the usage of spectral data over different grasslands with predictive modelling algorithms can build models to estimate major forage quality parameters regardless of the grassland type or management practice. The overall objective of this study is to develop comprehensive predictive models to estimate CP and ADF concentrations (from now on referred to as CP and ADF) on the field level, using UAV-borne imaging spectroscopy data from different grasslands. Specifically, to build models that can predict values regardless of the grassland type and to examine the effect of grassland type for the model performances. With this in mind, the specific sub-objectives are as follows:

- To understand the relationship between forage quality parameters (CP and ADF) and spectral reflectance
- To develop models for CP and ADF estimation from imaging spectroscopy data

and to evaluate models

- To create field-level CP and ADF maps for grasslands and describe the spatial and temporal variation of forage quality

4.2 Material and methods

4.2.1 Study area

The study was carried out on eight grasslands with different management practice and species composition. Table 4.1 gives details of the grasslands, and Figure 4.1 shows their locations on the map. Six grasslands were in nature protection areas, where no fertilisation was applied, and they were mowed only once per year. Two of them were mountain hay meadows (MHM), and another two were *Nardus stricta grasslands* (NSG). MHML and NSGL were MHM and NSG grasslands, which were substantially invaded by the neophyte *Lupinus polyphyllus*. The lowland hay meadow (LHM) is an extensively utilised grassland located on the Werra riverbank, and it was mowed two times per year. The intensively managed grassland (IMG) was fertilised and was harvested three times per year. All grasslands were in northern Hesse, Germany. MHM1, NSG1, LHM, and IMG grasslands were in Werra-Meißner district in Hesse (EPSG 4326: 9.9°N, 51.3°E) (Figure 4.1b). The other four grasslands (MHM2, NSG2, MHML, and NSGL) were located in UNSECO Biosphere reserve Rhön (EPSG 4326: 10.0°N, 50.5°E) (Figure 4.1c).

Table 4.1: Details of grasslands investigated in the study. (m.a.s.l. = meter above sea level).

Field ID	**Vegetation Type**	**Location (m.a.s.l)**	**Short Description**
MHM1	Mountain hay meadow	Werra-Meißner district (684)	Nature conservation grassland late harvest, no fertilisation
MHM2	Mountain hay meadow	Biosphere Reserve "Rhön" (739)	Nature conservation grassland late harvest, no fertilisation
NSG1	*Nardus stricta* grassland	Werra-Meißner district (718)	Nature conservation grassland late harvest, no fertilisation
NSG2	*Nardus stricta* grassland	Biosphere Reserve "Rhön" (822)	Nature conservation grassland late harvest, no fertilisation
MHML	Former Mountain hay meadow invaded by *Lupinus polyphyllus*	Biosphere Reserve "Rhön" (839)	Nature conservation grassland late harvest, no fertilisation
NSGL	Former *Nardus stricta* grassland invaded by *Lupinus polyphyllus*	Biosphere Reserve "Rhön" (846)	Nature conservation grassland late harvest, no fertilisation
LHM	Lowland hay meadow	Werra-Meißner district (135)	Extensive alluvial grassland, no fertilisation
IMG	Seeded grassland	Werra-Meißner district (199)	Intensive grassland, fertilised

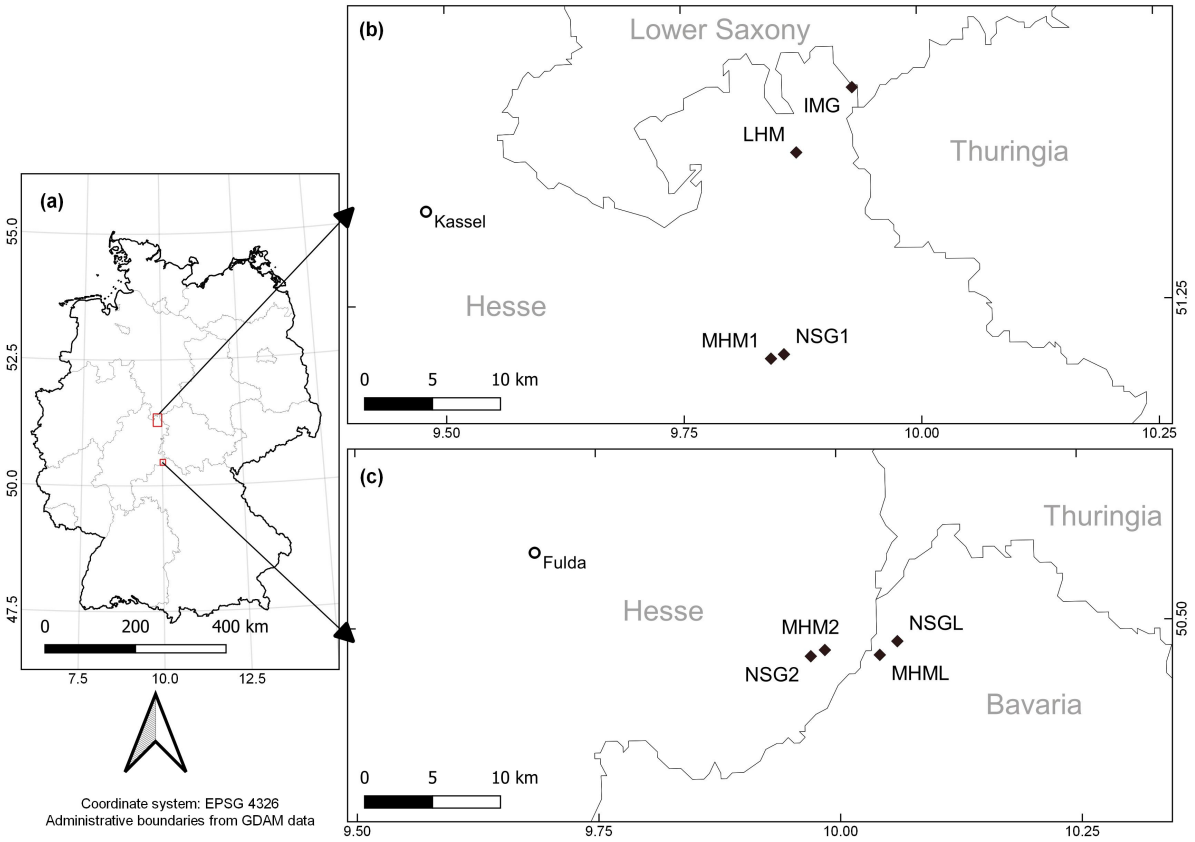

Figure 4.1: Map of Germany (a) and the areas with the location of grasslands investigated in the study (b,c). MHM: mountain hay meadow, NSG: *Nardus stricta* grassland, MHML: MHM invaded by *Lupinus polyphyllus*, NSGL: NSG invaded by *Lupinus polyphyllus*, LHM: lowland hay meadow, IMG: intensively managed grassland.

A 25 m by 50 m rectangle plot (1250 m^2) was selected as the study plot in grasslands located in Werra-Meißner district. In each study plot, twenty 1 m^2 subplots were randomly distributed and selected for destructive biomass samplings. The random subplot generation was done in QGIS, with each subplot having a minimum distance of 5 m to the nearest subplot.

The plots in the biosphere reserve Rhön were not allowed to be mown before 15 July and, to replicate different vegetation maturity stages, different sampling design was employed. From the grasslands in biosphere reserve Rhön, a 50 m by 30 m rectangle plot (1500 m^2) was chosen as the study plot. A total of fifteen small plots (8 m by 8 m) were established in each study plot, and they were in a regular grid (five rows and three columns). Three 1 m^2 sampling plots were picked from each small plot as the subplots for destructive biomass sampling.

4.2.2 Data collection

The UAV-borne imaging spectroscopy system

The Cubert Hyperspectral Firefleye S185 SE (Cubert GmbH, (Ulm, Germany) www.cubert-gmbh.de) snapshot camera (12 mm focal length) is an imaging spectroscopy sensor that acquires spectral images between 450 and 998 nm. It is a 2D imager with a multi-point spectrometer. The spectral resolution of the sensor (full width at half maximum) is 4.8 nm at 450 nm and 25.6 nm at 850 nm. The camera records a total of 138 spectral bands with a 4 nm sampling interval, but the manufacturer recommended to use only 126 bands between 450 and 950 nm. Each spectral band image is 50 by 50 pixel, and radiometric resolution is 12 bit (0–4096 digital numbers). In addition to the spectral bands, a grayscale panchromatic image is also recorded with 1000 by 990 pixels in size (Aasen et al., 2015; Cubert GmbH, 2016). The spatial resolution of the spectral image is 20 cm at 20 m flying height. The captured image from the camera is an image cube that has 126 bands.

The Cubert camera was attached to the UAV (RTK X8 Hyperspectral Mapping, Cubert GmbH, www.cubert-gmbh.de). It is a co-axial multi-rotor UAV equipped with real-time kinematic (RTK) global navigation satellite system (GNSS). It can fly automatically guided with less than 1 m position accuracy. The maximum payload is 2.5 kg, and maximum flight weight is 10 kg. The camera is affixed to a gimble on the UAV, which compensates for pitch and roll movement during the flight, and keeps the camera always nadir looking (Cubert GmbH and Copter Squad, 2018). Figure 4.2 shows the UAV and the attached Cubert camera.

Figure 4.2: The unmanned aerial vehicle (UAV) and the Cubert camera used in the study.

Spectral images and forage quality data

UAV-borne imaging spectroscopy data collection and destructive biomass sampling were carried out on every grassland immediately prior to each cut between May and September in 2018 (Table 4.2).

Spectral images were acquired between 10:00 and 14:00 under clear-sky conditions. Before the UAV flight, four corners of the study area were staked out using the Leica RTK GNSS (Leica Geosystem, www.leica-geosystems.com) and six black-white 1 m^2 ground control points (GCP) were distributed around the study plot. The coordinates of the GCPs were also measured using the RTK GNSS. The UAV flight mission was done with guided auto-pilot system in parallel flight lines at a flying height of 20 m and a horizontal flying speed of 5 ms^{-1}. Image acquisition points were calculated based on 80 % image overlap in both directions. In each image capturing point, the UAV hovered for 1 s to minimise the shaking effect. The UAV automatically triggered the Cubert camera on each correct position.

Table 4.2: Details on samplings of the grasslands investigated in the study.

Field ID	Harvest	Sampling date	No. quality samples
MHM1	First cut	13 July	20†
NSG1	First cut	14 July	19†
MHM2, NSG2, MHML, NSGL	First cut	15 June	20† (5, 5, 5, 5)
MHM2, NSG2, MHML, NSGL	First cut	27 June	20‡ (5, 5, 5, 5)
MHM2, NSG2, MHML, NSGL	First cut	11 July	20‡ (5, 5, 5, 5)
LHM	First cut	28 May	20†
	Second cut	24 September	15†
IMG	First cut	10 May	20†
	Second cut	06 June	20†
	Third cut	01 August	20†

† - 1 m^2 plots.

‡ - at each cut, three 1 m2 subplots inside the 64 m^2 plots were sampled, which gives a total of fifteen samples (3 × 5) at each cut for one grassland. However, in the lab analysis, samples from the three sub-plots were mixed and concentration data were determined (five quality samples per cut in one grassland).

Before the flight, the radiometric calibration for the Cubert camera was done using a spectral reference image on the white calibration panel (95 % reflectance Zenith Lite) and a dark current image by closing the lens using a lens cap. The relative spectral reflectance value for each image pixel was calculated according to Equation 4.1 during image acquisition.

$$R_{i,j,\lambda} = \frac{DN_{i,j,\lambda} - DC_{i,j,\lambda}}{WC_{i,j,\lambda} - DC_{i,j,\lambda}} \tag{4.1}$$

where i, j, and λ represent image row number, column number, and wavelength, respectively; R is the relative spectral reflectance; and DC, WC, and DN are the digital numbers of the dark current image, the white calibration panel image, and the raw image, respectively (Yang et al., 2017).

After spectral data collection, grass biomass was clipped on the identified 1 m^2 subplots at a stubble height of 5 cm. The fresh biomass was weighted in the field, and total biomass in each plot was divided into two separate samples for dry biomass and

forage quality analysis. The samples for the quality analysis were dried at 65 °C for 48 hours. Afterwards, the dried samples were ground for 1 mm uniform particles with a Foss CT 193 Cyclotec mill (FOSS, www.fossanalytics.com). Subsequently, the dry matter and the ash content of the ground samples were determined, and the N and ADF were determined.

The ADF was determined using the ANKOM 200 Fibre Analyser (ANKOM Technology, www.ankom.com). The samples were cooked in the analyser at 100° C for one hour in strong acid detergent (Cetyltrimethylammonium bromid in 1 N H2SO4). Afterwards, the cooked samples were washed, dried, and weighed to determine the ADF. The N concentration was measured using a Vario Max CHN elemental analyser (Elementar Analysensysteme GmbH, (Langenselbold, Germany) www.elementar.de), which employs the Dumas method in analytical chemistry. CP was computed multiplying the N concentration by 6.25. CP and ADF were determined for a total of one hundred and ninety-four (194) samples in all grasslands (Table 4.2).

From image cubes to digital ortho-mosaic

The following procedure was applied in each image acquisition to generate a mosaic from Cubert image cubes (Figure 4.3). First, the image cubes were exported as TIFF files using the CubeExport DOS (Cubert GmbH, www.cubert-gmbh.de) programme. It produced a stacked spectral image (50 × 50 pixels) and a grayscale image (1000 × 1000 pixels). Afterwards, the spectral images were disaggregated (nearest neighbour resampling) 20 times and stacked with the grayscale image using raster package in R programming language (R Core Team, 2019; Hijmans, 2019). Then, the preprocessed stacked images were input to the Agisoft PhotoScan Professional version 1.4.1 (64 bit) software (Agisoft LLC, (St. Petersburg, Russia) www.agisoft.com) (AgiSoft LLC, 2018). The PhotoScan software was used to create the ortho-mosaic from single images. The measured GCP coordinates were fed to the PhotoScan during the mosaic generation. The geo-referenced mosaic was then corrected for elevation to produce an ortho-mosaic with 127 layers (grayscale band + 126 spectral bands). The mean spectral reflectance data for each 1 m2 subplot were extracted from the ortho-mosaics of each sampling date. Due to noise in the spectral bands between 450 and 478 nm (8 bands), only 118 spectral bands (482–950 nm) were utilised in this study.

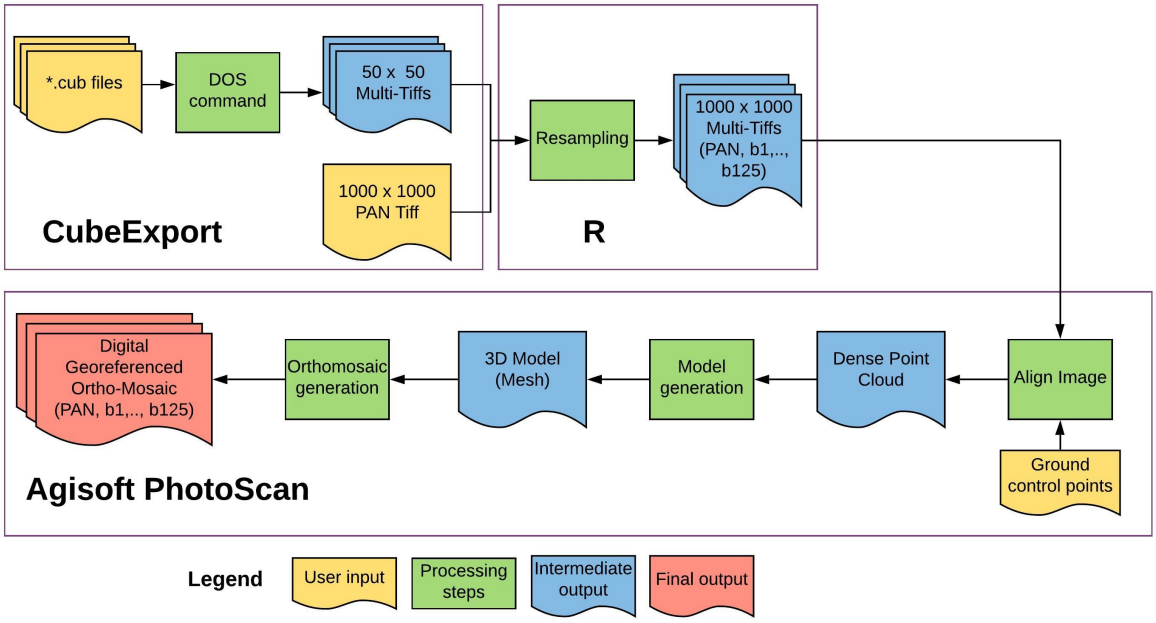

Figure 4.3: The workflow for processing the UAV-borne spectral images to obtain a single geo-referenced ortho-mosaic.

4.2.3 Data analysis

4.2.4 The relationship between reflectance and forage quality

Correlation analysis was carried out to understand the relationship between CP and ADF in the grassland biomass and the reflectance data. First, spectral reflectance data were normalised using vector normalisation based on Equation 4.2 (Sun et al., 2015), where x_i is the spectral vector for $i = 1, 2, \ldots, n$. The normalised reflectance data was transformed into the first derivative reflectance (Dawson and Curran, 1998) and continuum removal band depth (Clark and Roush, 1984).

$$x_i = \frac{x_i}{\sqrt{\sum \|x_i\|^2}} \tag{4.2}$$

Pearson correlation coefficients (r) between various transformed reflectance (actual, normalised, derivative, and continuum removal) data and forage quality data were computed. The optimal transformation method was identified based on the highest average correlation coefficient value. Simple linear regression models were created between each band from the identified transformed reflectance data set and forage quality data. Further, all possible variants of SR and NDSI (Equations 4.3 and 4.4) were derived from the reflectance data to check for the relationship with CP and ADF by simple linear regression modelling. The resulting models were evaluated based on

the adjusted coefficient of determination (adj.R^2) value.

$$SR_{\lambda 1,\lambda 2} = \frac{\rho_{\lambda 1}}{\rho_{\lambda 2}} \tag{4.3}$$

$$NDSI_{\lambda 1,\lambda 2} = \frac{\rho_{\lambda 2} - \rho_{\lambda 1}}{\rho_{\lambda 2} + \rho_{\lambda 1}} \tag{4.4}$$

where $\lambda 1, \lambda 2$ are two wavelengths and ρ is the reflectance at the wavelength.

Forage quality modelling with full spectral data

In conformity with the results from the simple linear regression analysis, neither single wavelengths nor SR or NDSI provided strong relationships with CP or ADF (data are shown in Results in Section 4.3.3) Consequently, full spectral reflectance data were used instead of selected spectral features. Five predictive modelling algorithms were utilised, namely, partial least squares regression (PLSR), random forest regression (RFR), Gaussian processes regression (GPR), support vector regression (SVR), and cubist regression (CBR). A short description of each regression algorithm with references is given in Table 4.3.

Table 4.3: Summary of the predictive modelling algorithms used in the study.

Algorithm	Description	Reference
PLSR	Partial least squares regression builds a linear regression model on the data projected in a space, based on nonlinear iterative partial least squares	Geladi and Kowalski (1986)
GPR	Gaussian processes regression finds a regression solution based on a probabilistic approach	Rasmussen and Williams (2006) and Williams and Rasmussen (2008)
RFR	Random forest is ensemble method consists decision trees and bagging	Breiman (2001)
SVR	Support vector regression builds linear regression models in high dimension feature space	Smola (1996), Drucker et al. (2003), and Smola and Scholkopf (2004)
CBR	Cubist is a rule based regression technique with boosting functionality	Quinlan (1992), Quinlan (1999), and Quinlan (2006)

Predictive modelling can be either supervised or unsupervised learning methods (Kuhn and Johnson, 2013). Thus, a supervised learning approach was employed in this study. First, the data set was split into two portions, representing the training and test dataset. Then, the model was trained using only the train data, while the test data were held out. After the model was trained, the model performance was evaluated using the test data (hold-out method) (Raschka, 2018). However, one random split of the data in the hold-out method results in only one model and the model performance may differ significantly among different split sets from the data (Kuhn and Johnson, 2013). Developing separate models for different data splits could explain the variability in model performance within the given data subsets. Therefore, a simulation was done 100 times and each replicate consisted of separate training (80 % data) and test (20 % data) data sets. Data set split was based on the stratified random sampling method with grassland field as strata. Then, 100 separate models using 100 training data sets were built for each regression algorithm using the R package "classification and regression training (caret)" (R Core Team, 2019; Kuhn and Johnson, 2013; Kuhn et al., 2018). In the model training phase, the repeated cross-validation (five folds; three repeats) technique was applied to tune the models' hyper-parameters (ncomp in PLSR; sigma in GPR; mtry in RFR; sigma & cost in SVR; committees & neighbours in CBR). Hyper-parameters are model configuration parameters that optimise the performance of the predictive modelling algorithm (Raschka, 2018). Finally, model testing was done using the corresponding 100 different test data. To evaluate the prediction performances of the model, the squared correlation coefficient between observed and prediction R^2_p (Kvalseth, 1985), root mean square error prediction ($RMSE_p$) (Equation 4.5), and normalised $RMSE_p$ based on observation range ($nRMSE_p$) (Equation 4.6) (Otto, 2019) were calculated. The overall workflow is shown in Figure 4.4.

$$RMSE_p = \sqrt{\frac{1}{n}\sum_{i=1}^{n}(y_i - \hat{y}_i)^2} \tag{4.5}$$

$$nRMSE_p = \frac{RMSE_p}{y_{max} - y_{min}} \times 100 \tag{4.6}$$

where y is the observed value, $\hat{y}$ is the predicted value, y_{max} is the maximum observed value, y_{min} is the minimum observed value, and n is the number of observations.

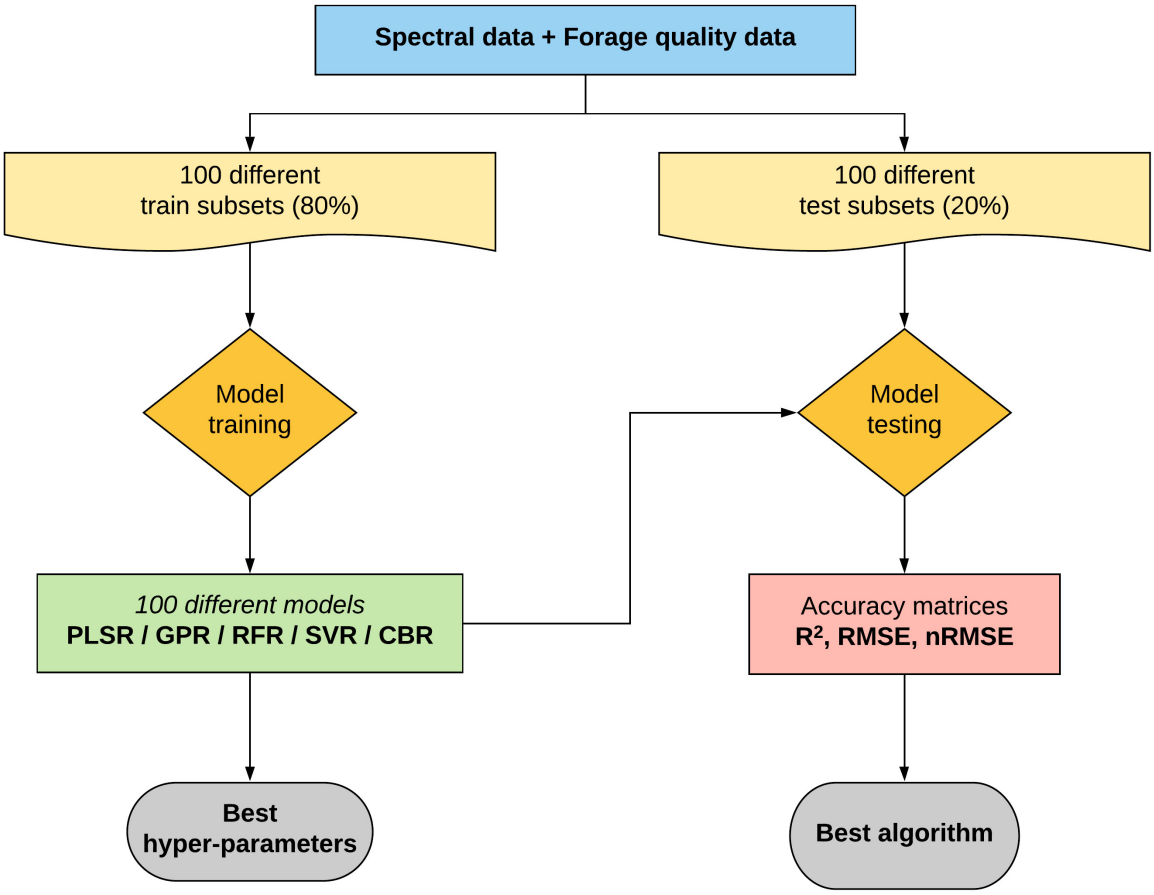

Figure 4.4: The model building workflow. PLSR:, partial least squares regression, RFR: random forest regression, GPR: Gaussian processes regression, SVR: support vector regression, CBR: cubist regression, RMSE: root mean square error, nRMSE: normalised RMSE.

On the basis of the optimal regression algorithms and hyper-parameter values, two models were calibrated using the 100 % data with the repeated cross-validation technique (five folds; three repeats) as the final predictive models for CP and ADF. The performance of final models was evaluated using R^2_{cv} (Kvalseth, 1985), $RMSE_{cv}$ (Equation 4.5), and $nRMSE_{cv}$ (Equation 4.6).

Forage quality prediction maps

Model predictions were utilised to create forage quality distribution maps. For this purpose, the ortho-mosaic was averaged to 1 m^2 pixel to match the ground sampling distance of the models, and for every pixel, CP and ADF were predicted for each harvest in each grassland. The predicted forage quality maps were compared visually for different cuts in the same grassland and examined for spatial and temporal variations.

4.3 Results

4.3.1 Forage quality data

Crude protein concentration varied between 5.1 %DM and 23.3 %DM, while ADF varied between 22.5 %DM and 38.5 %DM (Table 4.4). Forage from the intensively managed grassland (IMG) had the highest average CP and the lowest average ADF (Figure 4.5). However, forage from the two grasslands invaded by *Lupinus polyphyllus* (MHML, NSGL) contained higher CP than non-invaded grasslands. Further, CP and ADF were inversely correlated (correlation coefficient −0.78).

Table 4.4: Summary statistics for crude protein (CP) and acid detergent fibre (ADF) concentrations of different grasslands.

Variable	**CP (%DM)**	**ADF (%DM)**
n	194	194
Min	5.14	22.50
Max	23.35	38.54
Range	18.21	16.04
Median	9.84	30.84
Mean	11.20	30.77
Variance	16.29	10.57
Standard deviation	4.04	3.25
Coefficient of variation	36 %	11 %

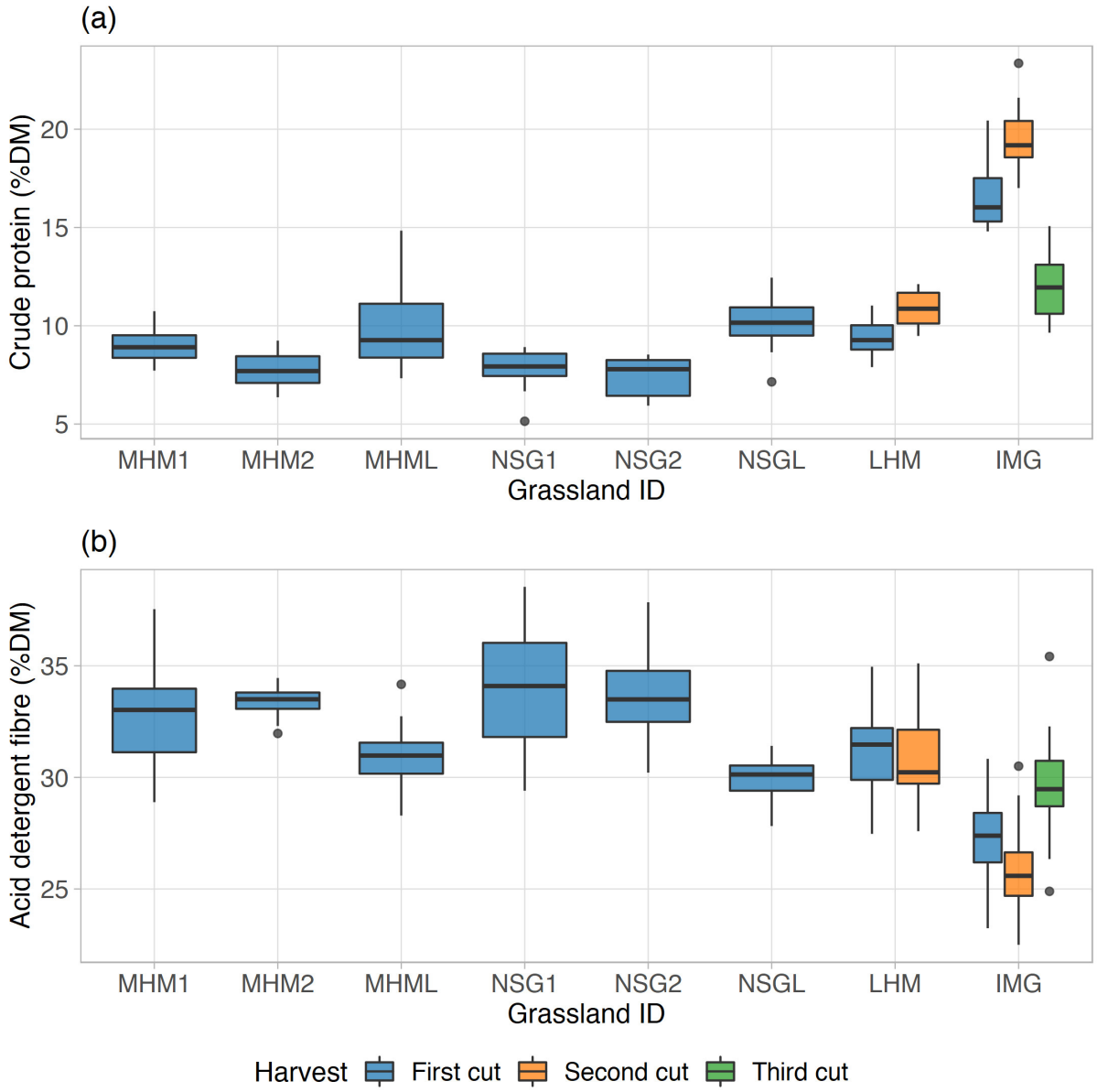

Figure 4.5: Distribution of crude protein (CP) (a) and acid detergent fibre (ADF) (b) concentrations in the harvested biomass of different grasslands.

4.3.2 Imaging spectroscopy data

Normalised mean reflectance values in the visible region (500–700 nm) obtained for every 1 m^2 sampling plot were lower for samples with higher CP values, along with higher values in the near-infrared region (750–900 nm) (Figure 4.6). A similar pattern was found for ADF data. However, there were some reflectance curves that did not follow the natural vegetation spectral curve, as they probably contained mixed vegetation signals.

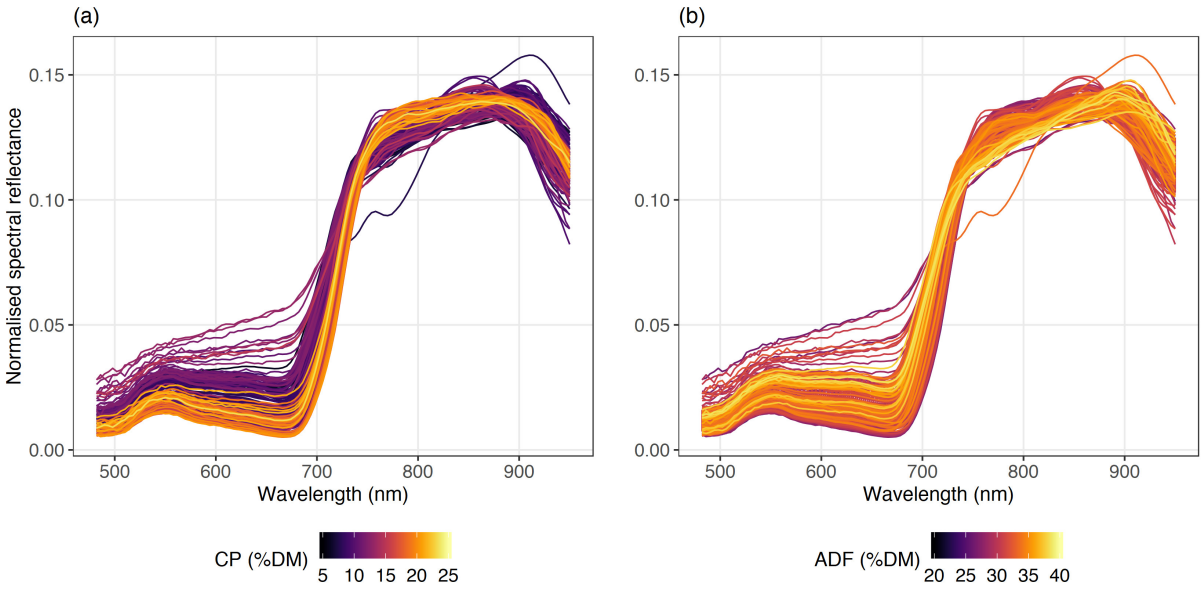

Figure 4.6: Normalised mean spectral reflectance for CP (a) and ADF (b) concentration data for all 1 m^2 sampling plots.

4.3.3 Linear modelling with individual bands and spectral indices (spectral features)

Correlograms for the different reflectance data sets (original, normalised, derivatives, and continuum removal band depth) are shown in Figure 4.7. On the basis of correlation values, normalised reflectance data obtained the highest average r-value from all wavelengths (0.26 for both CP and ADF) and highest cumulative sum of r-value (30.5 for both CP and ADF). Therefore, the normalised reflectance data were used for further statistical analysis in this study. For CP, the normalised reflectance value obtained negative r-values in the visible region, but these became positive in the near-infrared region. The correlogram of normalised reflectance for ADF showed an opposite pattern compared with that of CP.

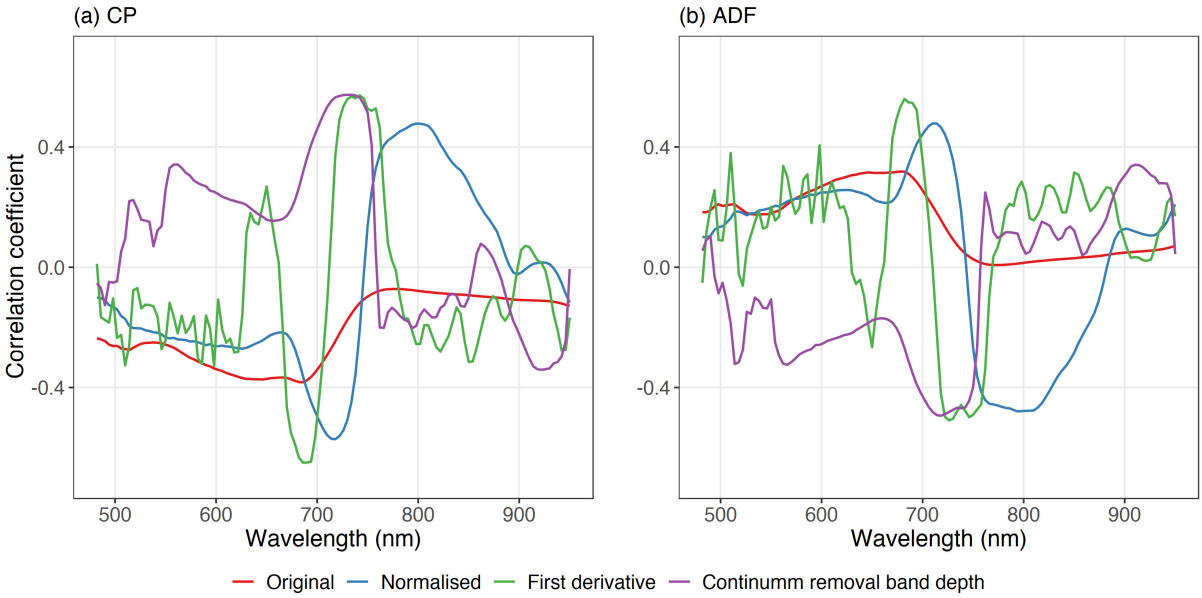

Figure 4.7: Correlogram for CP (a) and ADF (b) between original, normalised, derivative reflectance, and continuum removal band depth data.

With simple linear regression modelling, a weak relationship was found for both CP and ADF against individual spectral bands (Table 4.5). The best performing model for CP was found with 718 nm (adj.R^2 = 0.33) and for ADF with 794 nm (adj.R^2 = 0.23). Overall, the model performance was better for CP in the visible region and, vice-versa, for ADF in the near-infrared region.

Linear regression models with NDSI and SR performed better than single-band models (Table 4.5). Models with the two indices performed similarly, and the best results were found for similar band combinations for both forage quality values. For CP estimation, the best NDSI and SR models obtained adj.R^2 values of 0.42 and 0.40, respectively. Similarly, for ADF, the best NDSI and SR models obtained adj.R^2 values of 0.34 and 0.33, respectively.

Table 4.5: Summary of the best linear regression models using spectral features for CP and ADF estimation for different grasslands. (NDSI: normalised difference spectral indices; SR: spectral ratio)

Forage quality	Spectral feature	$\lambda 1$	$\lambda 1$	adj.R^2
CP	Single band	718 nm	-	0.33***
	NDSI	626 nm	486 nm	0.42***
	SR	626 nm	490 nm	0.40***
ADF	Single band	794 nm	-	0.23***
	NDSI	630 nm	486 nm	0.34***
	SR	630 nm	490 nm	0.33***

*** - significant at p <0.001

4.3.4 Predictive modelling with full spectral data

The best predictive modelling algorithm

On the basis of 100 different model runs with random train and test data sets, the model with the highest accuracy (lowest median $RMSE_p$ and lowest median $nRMSE_p$), the highest precision (highest R^2_p), and the highest stability (lowest standard deviation of $RMSE_p$) was identified as the best-performing model (Table 4.6 and Figure 4.8). Accordingly, the SVR model (median $RMSE_p$ = 1.9 %DM; median $nRMSE_p$ = 10.6 %; median R^2_p = 0.79; SD $RMSE_p$ = 0.29 %DM) was the best model for CP estimation, whereas for ADF, the CBR model (median $RMSE_p$ = 2.2 %DM; median $nRMSE_p$ = 13.4 %; median R^2_p = 0.56; SD $RMSE_p$ = 0.23 %DM) was the optimal model. PLSR was the least performing model type among all the predictive algorithm models. For CP estimation, $nRMSE_p$ of the SVR model varied between 7.0 % and 14.5 % and $nRMSE_p$ varied from 6.5 % to 16.4 % of the CBR model. Comparably, $nRMSE_p$ of ADF models varied from 10.7 % to 18.3 % and from 10.5 % to 16.7 % for the SVR and CBR models, respectively. Further, the precision of (median R^2_p) CP models was larger than 0.73, except for the PLSR model. However, the precision of (median R^2_p) ADF models was lower than for CP models.

Table 4.6: Summary of the predictive algorithm models (from 100 different model runs) for CP and ADF estimation of different grasslands. Bold values highlight the best models. (SD: standard deviation, CBR: cubist regression, GPR: Gaussian processing regression, PLSR: partial least squares regression, RFR: random forest regression, SVR: support vector regression).

Quality parameter	Algorithm	Median R^2_p	Median $RMSE_p$ (%DM)	SD $RMSE_p$ (%DM)	Median $nRMSE_p$
CP	PLSR	0.48	3.0	0.36	16.5 %
	GPR	0.73	2.3	0.33	12.4 %
	RFR	0.74	2.1	0.38	11.5 %
	SVR	**0.79**	**1.9**	**0.29**	**10.6** %
	CBR	0.77	1.9	0.45	10.4 %
ADF	PLSR	0.39	2.6	0.31	16.4 %
	GPR	0.51	2.3	0.25	14.5 %
	RFR	0.52	2.3	0.24	14.5 %
	SVR	0.50	2.3	0.26	14.5 %
	CBR	**0.56**	**2.2**	**0.23**	**13.4** %

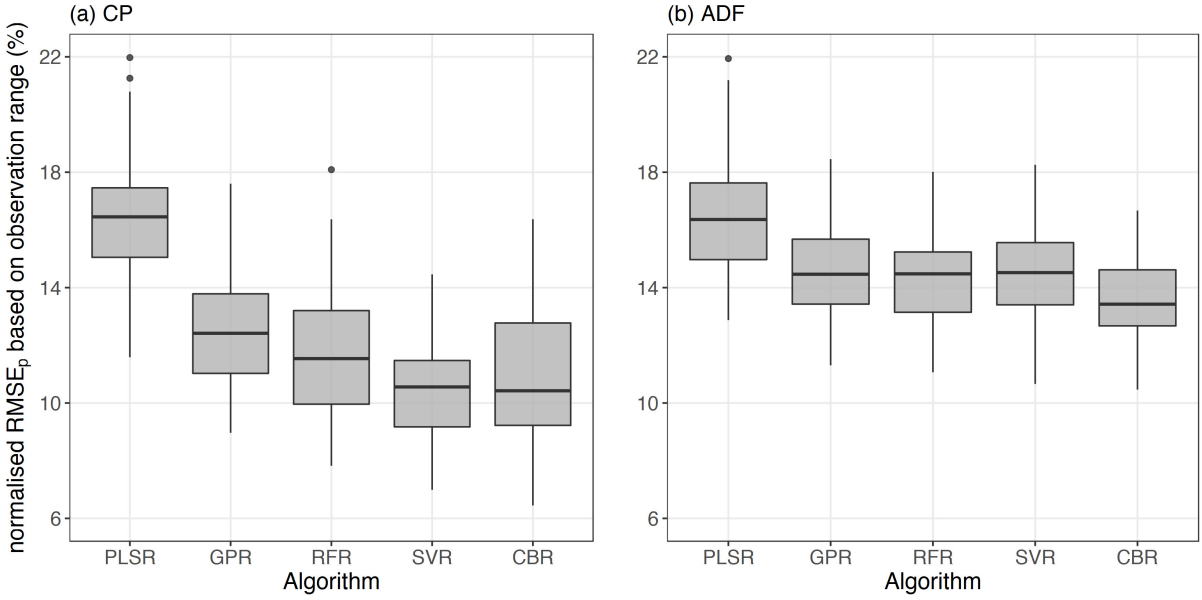

Figure 4.8: Normalised $RMSE_p$ distribution for CP (a) and ADF (b) concentrations in different grasslands for each predictive algorithm model (CBR: cubist regression, GPR: Gaussian processing regression, PLSR: partial least squares regression, RFR: random forest regression).

The plots of fit for the best-performing models show the model fit across all grasslands (Figure 4.9). Overall, prediction accuracy tended to be lower at higher levels of CP, whereas for ADF, accuracy was consistent across the whole range of values observed.

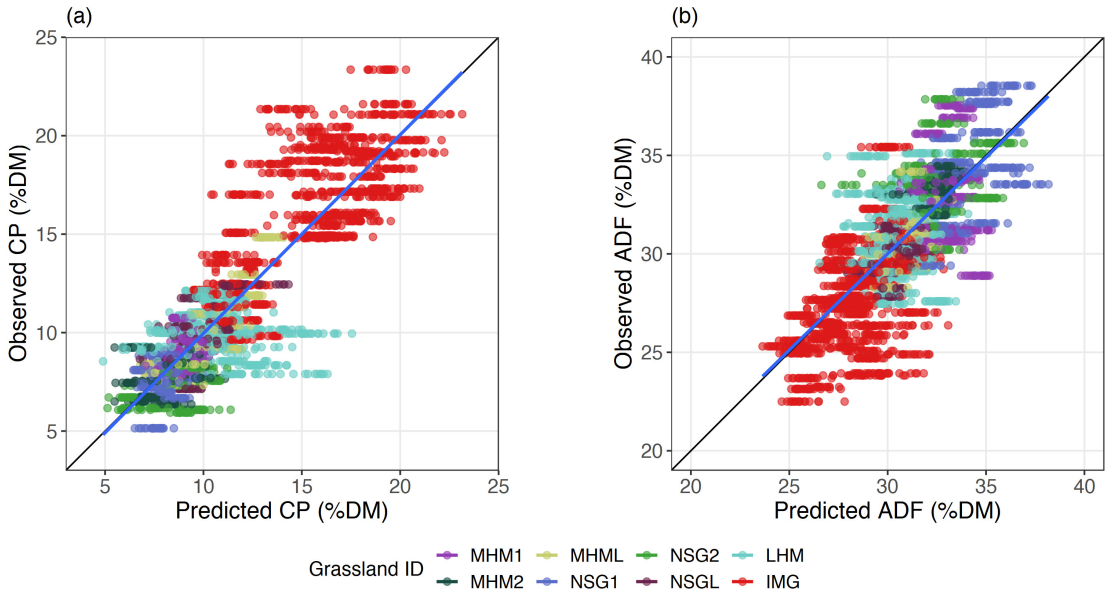

Figure 4.9: Observation versus prediction scatter plots from the SVR model for CP (a) and the CBR model for ADF (b) concentrations in different grasslands. Colours represent different grasslands. The black line is the 1:1 line, and the blue line represents the linear regression line between observed and predicted values.

Apart from the determination of the optimal predictive modelling algorithm, the best hyper-parameter values for each algorithm were identified. In the SVR model for CP estimation, the best sigma value was 0.035, and the optimum cost parameter was 20. In the CBR model for ADF, the optimal committees and neighbours values were 91 and 9, respectively (Table 4.7).

Table 4.7: The optimal hyper-parameter values for each predictive modelling algorithm to estimate CP and ADF concentrations in different grasslands.

Algorithm	**Hyper-parameter**	**Best for CP**	**Best for ADF**
PLSR	ncomp	6	7
GPR	sigma	0.045	0.040
RFR	mtry	20	20
SVR	sigma	0.035	0.025
	cost	20	4
CBR	committees	91	91
	neighbors	5	9

Final models

With SVR and the CBR predictive algorithms being identified as the best algorithms to estimate CP and ADF, repeated cross-validations were performed using the complete data set. The SVR model resulted in a $nRMSE_{cv}$ of 9.6 % with R^2_{cv} = 0.81 for CP estimation, while for ADF estimation, the CBR model had a $nRMSE_{cv}$ of 13.0 % and a R^2_{cv} of 0.60. The errors of the final models were found between the errors from 100 different models in the model training and testing phase.

4.3.5 Forage quality maps

The final models (SVR for CP and CBR for ADF) were applied to the mosaic images to generate forage quality prediction maps exemplary for the IMG and MHML grasslands (Figures 4.10 and 4.11). The produced maps show observed spatial and temporal variability for both quality parameters. The maps of the IMG grassland (Figure 4.10) indicate an increase in CP from the first to the second cut and a decrease from second to the third cut, which agrees with the values of the reference data (Figure 4.5). The maps for ADF (Figure 4.10g–i) indicate an opposite pattern compared with CP (Figure 4.10d–f). Both CP and ADF maps for the second cut (Figure 4.10e,h, respectively) indicate a considerably higher spatial variation compared with the first and third cut. The ADF map of the third cut (Figure 4.10i) shows certain areas (towards the west-southwest corner) with somewhat lower values (purple colour patches) compared with the rest of the field.

The true colour images of the MHML grassland show a unique chessboard pattern at the later cutting dates (Figure 4.11). While on the 13th June, the whole area had the same maturity stage (the first cut was taken at 15 June on a third of all plots), the five brownish areas in the picture from 27 June represent the plots that were regrown since the first cutting date. Brown colour shades further increase in the picture from 11 July. The forage quality maps for the last two dates were masked using small plot boundaries (64 m^2). The CP map from 13 June shows higher CP value patches (yellow patches) at the northern region of the plot and lower ADF values (purple spots) for corresponding areas are shown in the ADF map from the same date. The most matured grass plots were available on 11 July, where the lowest CP values are shown (dark purple plots). Those patterns are less pronounced in the ADF map of 11 July. Colours on the map from 27 June indicate that the biomass on recently cut areas has more significant ADF concentrations than that from areas with continued growth, and thus an advanced plant maturity.

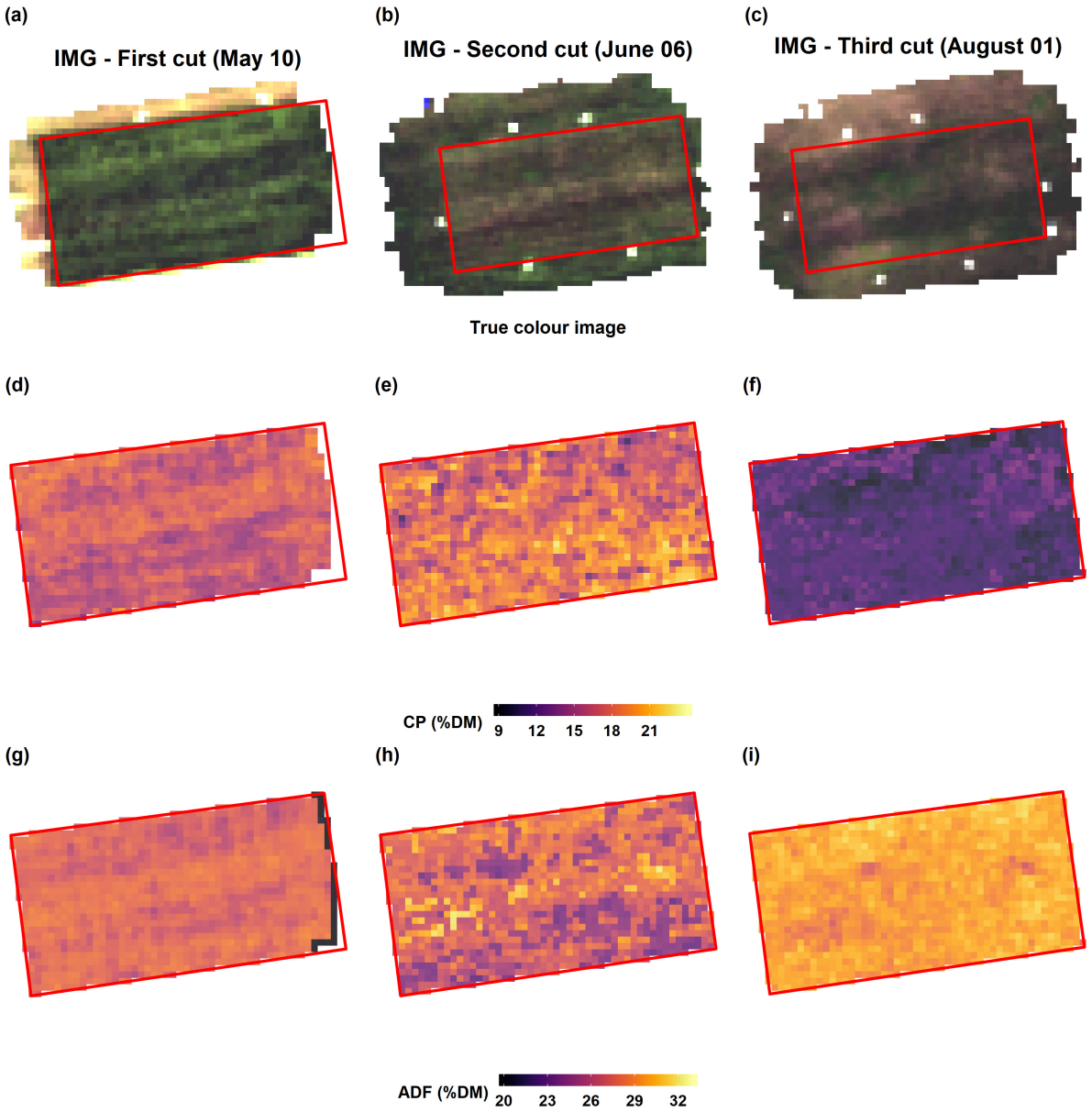

Figure 4.10: Forage quality prediction maps for the intensively managed grassland (IMG). The first row is the hyperspectral mosaic in the true colour composite (R: 606 nm, G: 546 nm, B: 482 nm) for different sampling dates (a–c). Predicted CP and ADF maps are shown in the second (d–f) and third rows (g–i), respectively. Columns represent different cutting dates. The value range in the colour scale is different for each quality parameter. White spots in the map represent no data pixels.

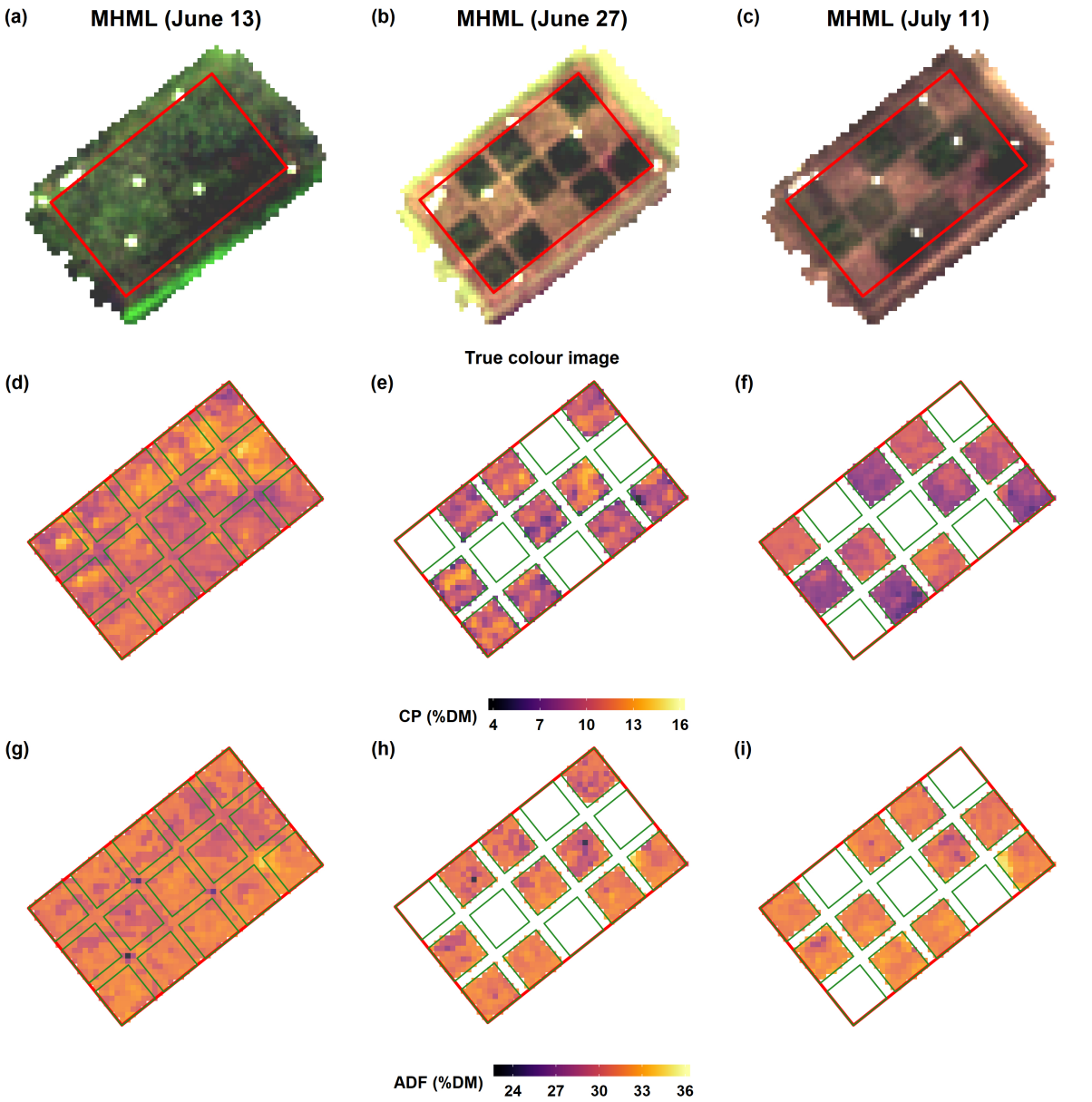

Figure 4.11: Forage quality prediction maps for the mountain hay meadow invaded by *Lupinus polyphyllus* (MHML). The first row is the hyperspectral mosaic in the true colour composite (R: 606 nm, G: 546 nm, B: 482 nm) for different sampling dates (a–c). Predicted CP and ADF maps are shown in the second (d–f) and third rows (g–i), respectively. Columns represent different cutting dates. The value range in the colour scale is different for each quality parameter. White spots in the map represent no data pixels. The 64 m^2 small plot boundaries are in green colour.

The extracted CP and ADF values from each cutting date of the MHML grassland were plotted against each other to understand the temporal variation of the relationship between the two forage quality parameters (Figure 4.12). The strength of the negative linear relationship between the two parameters decreased when the cutting date was delayed. Further, the distribution of CP values decreased with increasing duration of growth, but the distribution of ADF values did not change significantly.

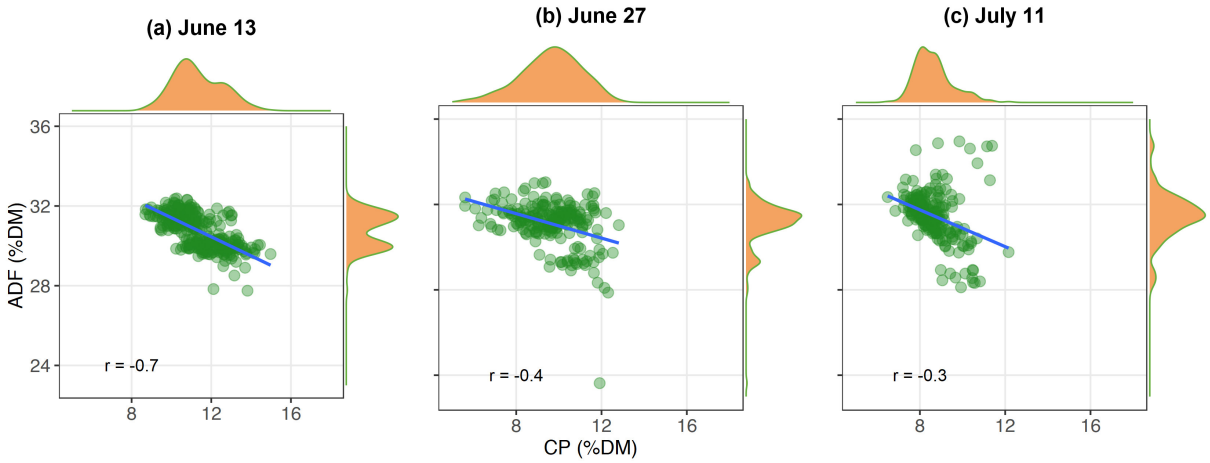

Figure 4.12: Scatter plots between predicted CP and ADF from MHML's small plots harvested on 13 June (a), 27 June (b), and 11 July (c). The marginal histogram shows the distribution of each axis value.

4.4 Discussion

Correlograms were used to understand the relationship between grassland CP and ADF and spectral reflectance (Figure 4.7). For both quality parameters, normalised spectra indicated a stronger relationship with forage quality parameters than the original spectra or other spectra transformations (derivatives and continuum removal band depth). The normalisation process reduced the temporal noise of the data, which strengthened the relationship between spectral features and forage quality. Further, two correlograms from CP and ADF showed an inverse pattern, confirmed by the negative correlation between them. Nevertheless, both forage quality parameters had a stronger relationship in the red-edge and the near-infrared regions of the spectrum.

Linear regression models with spectral features (single waveband, NDSI, SR) obtained a maximum adj.R^2 of 0.42 for CP and 0.34 for ADF. The best correlated NDSIs comprised wavebands in the chlorophyll absorption features in the visible domain of the spectrum (470–518 nm and 550–750 nm), which relates to N and other biochemicals in green canopies (Mutanga et al., 2004). These results paralleled with the results from previous studies that come from the same geographical region (Biewer et al., 2009b; Safari et al., 2016a). The study from Safari et al. (2016b) obtained linear regression models with NDSI with R^2 of 0.58 and 0.49 for CP and ADF, respectively. Moreover, the results from Biewer et al. (2009b) reported R^2 values of 0.33 and 0.13 R^2 for CP and ADF models with SR, respectively. Nonetheless, the results from the studies mentioned above

were obtained with field spectroscopy data, which had a more comprehensive spectral range (305–1700 nm) than the camera utilised in the present study.

Several predictive modelling algorithms were tested to identify the best algorithms to estimate CP and ADF from the full spectral data, as no single consistent algorithm was shown to surpass all the given circumstances every time in a study by the authors of (Yuan et al., 2017). Moreover, model consistency was evaluated by training and testing 100 models using 100 different random train and test data sets, which allowed to disclose the model performance irrespective of the calibration data set. Except for the PLSR, other tested predictive algorithms (GPR, RFR, SVR, and CBR) proved promising for the underlying data. The SVR and CBR models for CP and ADF estimation showed the maximum precision (highest R^2_p) and prediction accuracy (lowest $nRMSE_p$) followed by the RFR, GPR, and PLSR models, respectively. SVR and CBR predictive modelling algorithms were previously utilised to estimate water quality parameters based on spectral data (Keller et al., 2018; Hafeez et al., 2019), however, to our knowledge, such algorithms have not been employed so far to estimate forage quality parameters.

According to the literature, the PLSR and RFR were the most prominent predictive modelling algorithms in forage quality parameter estimation using spectral data. For example, Safari et al. (2016b) reported on PLSR models, which obtained nRMSE values of 8.5 % and 7.3 % for CP and ADF, respectively. However, PLSR models resulted in the lowest accuracies both for CP and ADF in this study. Moreover, Pullanagari et al. (2018) achieved an nRMSE of 11.2 % for CP with the RFR model, and Singh et al. (2017) obtained an nRMSE of 21.7 % for ADF with the same modelling algorithm. It is noteworthy that the studies mentioned above only tested one predictive modelling algorithm; thus, no conclusions are possible considering the comparison with other algorithms.

Both CP and ADF estimation models resulted in less than 15 % relative prediction error. However, CP estimation had a slightly lower relative error (median $nRMSE_p$ = 10.6 %) than ADF estimation (median $nRMSE_p$ = 13.4 %). A similar relative error pattern for CP and ADF estimation models was obtained in previous studies that utilised field spectroscopy data (Kawamura et al., 2008; Pullanagari et al., 2012; Safari et al., 2016b). Moreover, the data points from the IMG were clustered out and acted as the driver of the CP model according to the plot of fit (Figure 4.9a). Although, ADF data points in the observed against predicted plot did not highlight a similar pattern (Figure 4.9b). The high variation of CP between the cuts in IMG due to intensive management practice might be the reason for the mentioned pattern. However, the data points from

other grasslands were mostly grouped in both plots because they almost experienced similar management practice.

Remarkably, the wavelength (718 nm) that obtained the highest linear correlation with CP turned out to be the most fundamental wavelength for the final CP and ADF models (Appendix Figure 4.13). However, the identified first most important wavelengths were not related to any foliar chemical absorption feature, such as chlorophyll, protein, or cellulose (Curran, 1989). According to Curran (1989), the absorption features that relate to CP and ADF can be found at wavelengths in the shortwave infrared region of the spectrum (1400–3000 nm). Singh et al. (2017) also confirmed that important wavelengths for ADF were in the shortwave infrared region of the spectrum. The camera used in the present study did not have the sensitivity to the shortwave infrared regions, even though the study showed a superior accuracy for grassland CP and ADF.

Imaging spectroscopy provides the advantage to generate maps by direct application of the model to recorded spectral images without the need for spatial interpolation. The prediction maps in our study displayed a substantial spatial variation in forage quality on the grasslands. While there is an inverse relationship between CP and ADF at the early cutting date of the MHML grassland, it vanishes with the increasing maturity of plants (Figure 4.12). Thus, biomass from such grasslands (MHML, NSGL) may display a much more considerable variation in CP than in ADF content, which probably depends very much on the degree of *Lupinus polyphyllus* invasion. Such information may help farmers to identify areas with contrasting forage quality, which is a prerequisite for targeted site-specific management of larger fields, for example, to determine a sound scheduling of mowing or grazing activities. Further, biomass from grassland areas with contrasting quality may be collected and ensiled separately to match the requirements of animals, which usually differ sharply among different animal species and performance categories.

To summarise, predictive modelling algorithms allow an adequate forage quality estimation, regardless of the grassland type and cutting regimes applied. Ultimately, fine-tuning of the calibrated models with data from further diverse grassland types could increase the robustness of the models to generate forage quality maps for grasslands with different vegetation types and management practices.

4.5 Conclusions

The present study aimed to estimate CP and ADF concentrations of a multitude of grasslands with different vegetation composition and cutting regimes applied based

on UAV-borne imaging spectroscopy data. It was demonstrated that the resulting models could accurately estimate CP and ADF irrespective of the grassland type, and that model accuracies are in the same range as those obtained with the use of field spectroscopy. With such models, forage quality maps can be generated, which may provide a benefit for practical grassland farming. Eventually, continued tweaking of the models with data from additional grasslands will be a way forward to ultimately obtain an accurate generalised model with a validity range that covers most grasslands within a broader region.

Appendix

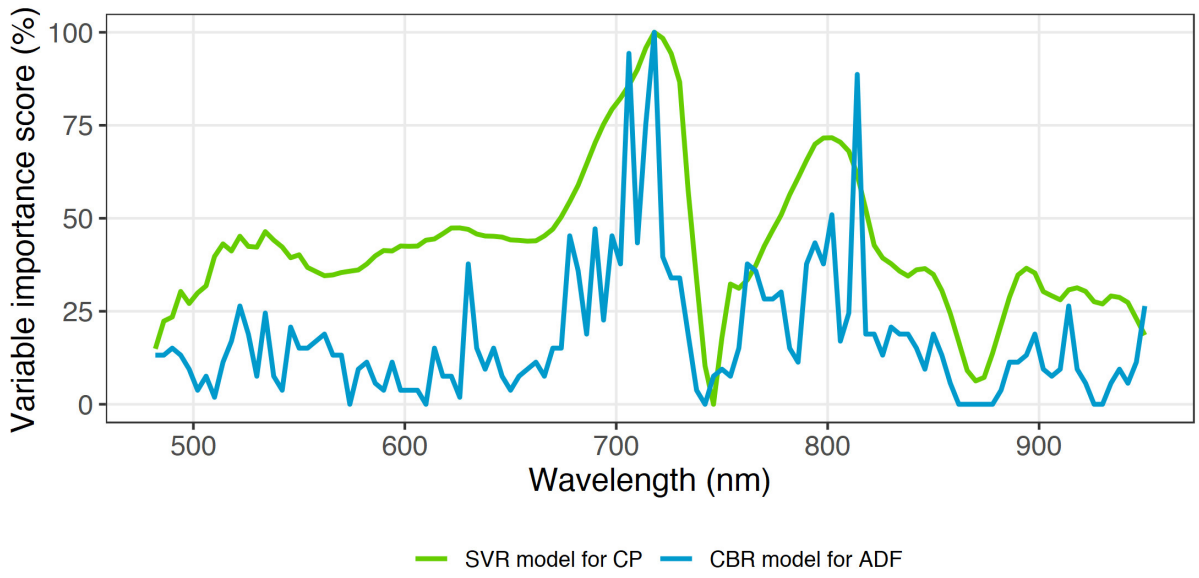

Figure 4.13: Wavelength importance for two models. The higher the important variable score, the higher the importance of the wavelength.

The content of Chapter 4 has not been changed from the original published version.

Wijesingha, J., Astor, T., Schulze-Brüninghoff, D., Wengert, M. & Wachendorf, M. (2020). Predicting Forage Quality of Grasslands Using UAV-Borne Imaging Spectroscopy. Remote Sensing, 12(1), 10.3390/rs12010126. (Received: 3 December 2019; Accepted: 25 December 2019; Published: 1 January 2020)

Chapter 5

Mapping invasive *Lupinus polyphyllus* Lindl. in semi-natural grasslands using object-based analysis of UAV-borne images

Abstract

Knowledge on the spatio-temporal distribution of invasive plant species is vital to maintain biodiversity in grasslands which are threatened by the invasion of such plants and to evaluate the effect of control activities conducted. Manual digitising of aerial images with field verification is the standard method to create maps of the invasive *Lupinus polyphyllus* Lindl. (lupine) in semi-natural grasslands of the UNESCO biosphere reserve "Rhön". As the standard method is labour- and time-intensive, a workflow was developed to map lupine coverage using an unmanned aerial vehicle (UAV)-borne remote sensing (RS) along with object-based image analysis (OBIA). UAV-borne red, green, blue (R, G, B) and thermal imaging, as well as photogrammetric canopy height modelling (CHM), were applied. Images were segmented by unsupervised parameter optimisation into image objects representing lupine plants and grass vegetation. Image objects obtained were classified using random forest classification modelling based on objects' attributes. The developed classification model was employed to create lupine distribution maps of test areas and predicted data were compared with manually digitised lupine coverage maps. The classification models yielded a mean prediction accuracy of 89 %, and 0.78 mean kappa statistics. The maximum difference in lupine area between classified and digitised lupine maps was 5 %. Moreover, the

pixel-wise map comparison showed that 88 % of all pixels matched between classified and digitised maps. Our results indicate that lupine coverage mapping using UAV-borne RS data and OBIA provides similar results as the standard manual digitising method and, thus, offers a valuable tool to map invasive lupine on grasslands.

Keywords : invasive plant species; Lupine; RGB camera; object-based image analysis; spatial coverage mapping; grassland

5.1 Introduction

Biological invasion is threatening to biodiversity in many ecosystems in the world. The invasion by alien plant species is considered as one of the significant drivers for loss of biodiversity and ecosystem functionality. The leading cause for the introduction of alien plant species is human activities. After a new plant species is introduced to the ecosystem, depending on the adaptation capability of the plant it obtains a naturalisation status which is the ability to self-sustain without human involvement (Pyšek and Richardson, 2011). At present, there are 3749 naturalised alien plant species in Europe, and 37.4 % out of them occur in grassland habitats (Lambdon et al., 2008).

Processes and dynamics of invasion of plant species are complex (Courchamp et al., 2017). However, knowledge on spatial, temporal distribution of invasive plant species in a given habitat is critical to understand invasion pattern (Müllerová et al., 2017), and maps showing invasive plants' distribution are helpful for effective control activities. Aerial image digitising verified with field survey is the standard method to create invasive plant species distribution maps. Such maps are time-consuming and labour intensive to produce due to aerial image acquisition, manual digitising, and field verification steps.

Classification of remotely sensed images to map invasive species is a well-adopted technology for many invasive species in different parts of the world and various ecosystems (Royimani et al., 2018). In grasslands, invasive woody (Mirik et al., 2013) and shrubby (Laliberte et al., 2004; Ishii and Washitani, 2013) species mapping has shown excellent results with satellite and airborne image classification. Meanwhile, using an unmanned aerial vehicle (UAV) borne remotely sensed (RS) imaging was increasingly applied for invasive species mapping in the recent years in flood plains and coastal regions (de Sá et al., 2018; Martin et al., 2018; Abeysinghe et al., 2019). Cost-effectiveness, high spatial and temporal resolution and the increasing availability of various miniature sensors (e.g. RGB cameras, spectral sensors, thermal cameras) are the main advantages of the UAV-borne imaging compared to satellite RS data (Michez et al., 2016).

Apart from the spectral or thermal information, UAV-borne RS data can also provide 3D point cloud data, which can be employed to derive canopy height models (CHM) for grassland canopies (Grüner et al., 2019; Wijesingha et al., 2019).

UAV-borne RS images are very-high spatial resolution images (less than 50 cm), where one object in the real world is represented by many pixels. Object-based image analysis (OBIA) can better be employed when pixels are considerably smaller than the object to be identified (Blaschke, 2010). Several studies indicated that OBIA provides substantial advantages for mapping invasive plant species based on UAV-borne RS data (Michez et al., 2016; Martin et al., 2018; Abeysinghe et al., 2019). Typical OBIA employs rules derived from the object's attributes to classify an object, which requires expert knowledge and limits the transferability of the classification model (Belgiu et al., 2014). Contrary, machine learning classification algorithms (e.g. random forest, support vector machine) have shown their capability in OBIA procedures, as they do not require prior knowledge of the objects (Grippa et al., 2017).

Lupinus polyphyllus Lindl. (hereafter referred to as lupine) is on the list of the most 150 widespread alien plant species in Europe (Lambdon et al., 2008). The lupine plant is about 50-150 cm tall and contains 1-2 cm broad leaflets. Lupine flowers are up to 80 cm long in a single terminal, and they are in shades of blue, pink and white (Fremstad, 2010). Lupine is native to the western parts of North America. It has been recorded in many habitats in Europe, such as grasslands in Germany, Lithuania, and road verges as well as in ruderal areas in Scandinavia (Fremstad, 2010). The UNESCO biosphere reserve Rhön in Germany covers a total area of 2433 km^2 and mainly consists of low mountain semi-natural grasslands (e.g. NATURA habitat types 6520 - mountain hay meadows and 6230 - species-rich *Nardus* grasslands) (Biosphärenreservat Rhön, 2019). In the last few decades, lupine invaded significant parts of the grasslands in the biosphere reserve. It substantially changed the habitat functionality mainly through the ability to fix atmospheric nitrogen, which transforms the low-growing, open and species-rich grasslands into dense and productive, but species-poor dominance stands (Otte and Maul, 2005). Individual lupine plants are controlled manually at early stages of invasion to prevent a massive invasion by lupine, and grassland mowing is allowed after 1st July to maintain a broad diversity of insects and ground breeding birds (Biosphärenreservat Rhön, 2019).

The knowledge of the spatial distribution of lupine in the grasslands is vital to conduct control activities and to monitor their efficacy. The first lupine distribution map of the region was created in 1998 using manually digitised aerial photographs at a 1:2500 scale (Otte and Maul, 2005). The latest map of the spatial distribution was gen-

erated in 2016 using 20 cm digital ortho-mosaics from aerial photographs (Klinger et al., 2019). Those maps were useful to monitor changes in the lupine distribution in the long term. The interval between the two maps of eighteen years is partly due to the time and labour demanding processes involved. Therefore, a repeatable, transferable methodology is needed, that produces lupine distribution maps at different spatial and temporal scales to monitor the lupine distribution and to assess the benefit of control activities.

According to Skowronek et al. (2018), RS based mapping of the spatial distribution of Lupine was not successfully implemented until now. In order to fill this gap, we propose an approach to map invasive lupine in grassland, which is based on UAV-borne RS data and OBIA. We hypothesise that the proposed procedure could categorise lupine and non-lupine vegetation in grasslands with the same precision as the standard digitising method. This study presents an operational workflow to create maps of lupine cover and compares lupine distribution maps from the developed workflow with manually digitised lupine coverage maps.

5.2 Material and methods

5.2.1 Study area

The study was carried out in two grassland fields UNESCO biosphere reserve Röhn in Germany which were invaded by lupine (Figure 5.1a, Figure 5.1b, Figure 5.2). One field was classified as a former mountain hay meadow (hereafter referred to as G1), and the other was an old *Nardus stricta* grassland (hereafter referred to as G2). In both fields, rectangle plots of 1500 m2 (50 m by 30 m) were chosen as study areas, and 15 small plots of 64m2 (8 m by 8 m) were established within a grid (Figure 5.1c, Figure 5.1d). Three cutting dates (12th June, 26th June, 09th July, hereafter referred to as D1, D2, and D3, respectively) were randomly assigned to 5 replicated plots (Figure 5.1c, Figure 5.1d). At each date, plots were mowed at a stubble height of 5 cm, and biomass was removed from the field.

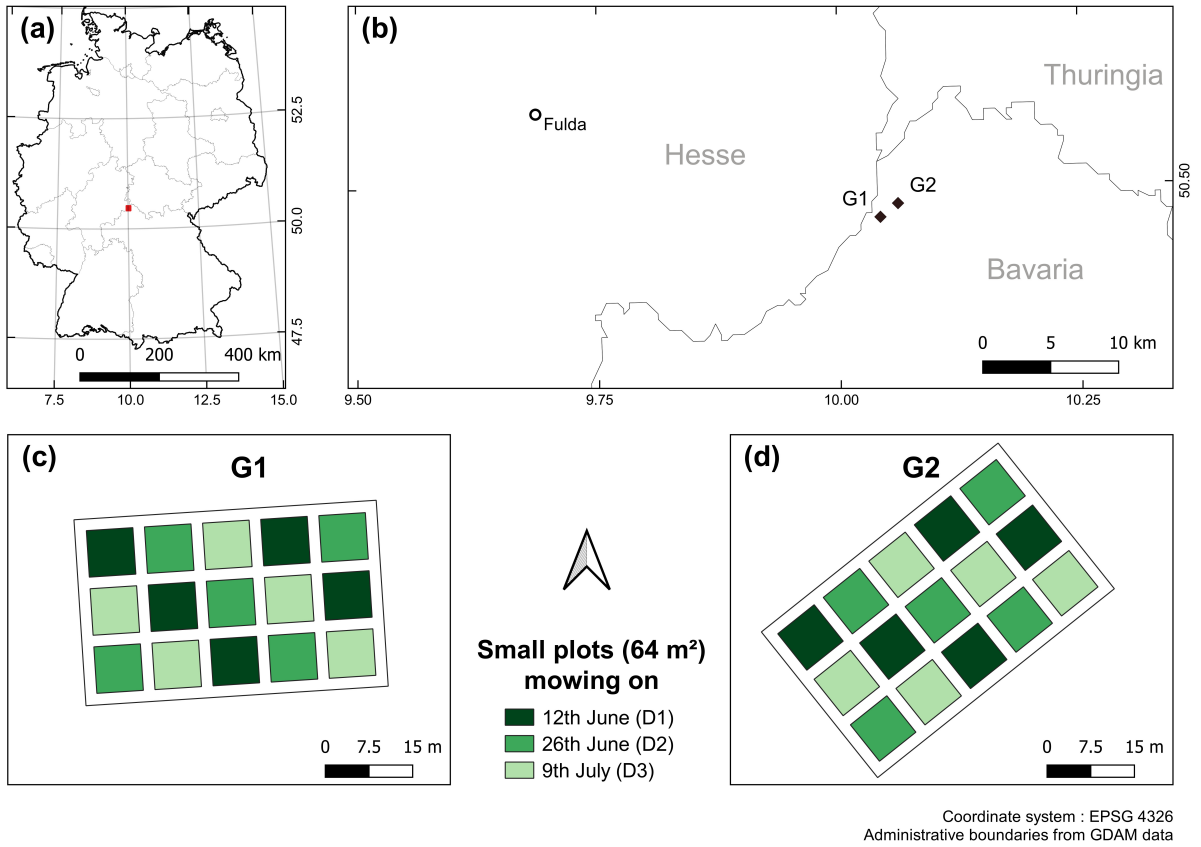

Figure 5.1: (a) Location of the UNESCO biosphere reserve Rhön, (b) positions of the two grassland fields, and the experimental plot design of (c) G1 and (d) G2 grasslands.

Figure 5.2: Lupine invaded grassland in the Röhn biosphere reserve.

5.2.2 Data collection

At each sampling date in each grassland field, UAV-borne images were acquired. A DJI-Phantom IV quadcopter (DJI, China) with an inbuilt off-the-shelf camera (FC330) was employed to obtain UAV-borne RGB images. The camera (FC330) captures a 12-megapixel image in red (R), green (G), and blue (B) bands. The UAV was flown at 20 m flying height, and it resulted in 0.09 m ground sampling distance. The UAV flight mission was designed using Pix4D capture app for Android (App version 4.4.0, Pix4D, Switzerland). The UAV was flown as double grid mission (two perpendicular missions), and the camera was triggered automatically to capture nadir looking images based on the image overlap configuration (80 % both forward and side overlap). All the flight sessions were conducted between 12:00 and 14:00. Before each flight session, nine black and white 1 m2 ground control points were distributed over the study area. Just after the UAV flights, the position of each ground control point was measured using a Leica RTK GNSS (Leica Geosystems GmbH, Germany) with 2 cm 3D coordinate precision. Additional UAV-borne RGB image was taken on 16th August 2019, when the whole fields were mowed.

A FLIR Vue Pro R (FLIR Systems Incorporation, USA) thermal camera was attached to the UAV parallel to the RGB camera. The camera has a 19 mm lens, and it has a spectral sensitivity between 7500 - 13500 nm. With a single UAV flight, both thermal and RGB images were captured simultaneously. The thermal camera captures images as a radiometric JPEG which contains radiometrically calibrated temperature data. The thermal image has 640 by 512 pixels (FLIR, 2016). The thermal camera was triggered every second throughout the whole UAV mission. Before each thermal data collection, metadata related to the thermal camera was collected using the FLIR UAS 2 app (App version 2.2.4, FLIR Systems Incorporation, USA), such as distance to the target (20 m), relative humidity, air temperature, and emissivity (0.98). All the metadata was saved in each captured image's EXIF data.

A total of six UAV-borne RGB and six thermal datasets were collected. Hereafter, each dataset is labelled according to cutting date and grassland type (D_iG_j: where i = 1, 2, 3 and j=1, 2). In each dataset, maturity stages of grasslands were different due to mowing activities in 64 m2 small plots. Maturity stage was lowest (V_0) in the D1 dataset and was the same for all 30 small plots. At the 2nd cutting date (D2), 20 small plots out of 30 were covered by two weeks older vegetation (V_{2weeks}), while 10 small plots (which were cut at D1) had vegetation which was regrown for two weeks (VR_{2weeks}). The D3 dataset was composed of 10 plots with undisturbed vegetation (V_{4weeks}) which was four weeks older than V_0, 10 plots of (VR_{2weeks}), and further 10 plots with vegetation

regrown for four weeks (VR_{4weeks}) after D1.

5.2.3 Object-based image analysis

Canopy height model and point density

Each collected dataset was processed separately, and the same procedure was applied, as explained below. The UAV-borne RGB images and coordinates of ground control points were processed with the Agisoft PhotoScan Professional version 1.4.4 software (Agisoft LLC, Russia) (AgiSoft LLC, 2018). The software applied structure from motion (SFM) technique to align multi-view overlapping images and to build a dense 3D cloud point. The procedure of point cloud generation and canopy height computation was adopted from Wijesingha et al. (2019), and further details of the process can be found there.

The point density (PD) raster was created from the dense point cloud by binning into a raster with 2cm. The PD raster contained point count under a cell area (4 cm^2). The digital terrain model (reference plane) was generated using the August RGB images with a cell size raster of 5 cm. The z values of 3D point cloud and the digital terrain model based on x, y locations were subtracted to generate a point cloud with canopy height. The point cloud with canopy height was binned into the 2 cm cell size raster, where each cell contained mean crop height value and hereafter it was considered CHM raster.

RGB ortho-mosaic

RGB ortho-mosaic was obtained after further processing of the dense point cloud in PhotoScan software. The output RGB ortho-mosaic was geo-referenced with a 1 cm spatial resolution. The RGB ortho-mosaic was converted into hue (H), intensity (I), and saturation (S) colour model using GRASS GIS and hereafter it was considered as HIS ortho-mosaic (Gonzalez and Woods, 2008; GRASS Development Team, 2017).

Thermal ortho-mosaic

The single JPEG thermal image contained 8-bit digital numbers. Following workflow and equations were adapted from Turner et al. (2017) to convert digital numbers to temperature values. The conversion workflow was conducted with EXIFtools and R programming language (Phil Harvey, 2016; Dunnington and Harvey, 2019; R Core Team, 2019). A raw thermal TIFF image was exported from the JPEG image. Metadata of image were extracted from the JPEG EXIF header for each image. Based on the

metadata and raw TIFF image values, the image with temperature was computed and exported as a TIFF file. The exported TIFF image contained a calibrated temperature value in degree Celsius (°C). Like RGB ortho-mosaic generation, thermal ortho-mosaic with 2 cm spatial resolution was generated using calibrated thermal images.

Spectral shape index and texture images

A spectral shape index (SSI) (Equation 5.1) based on RGB image values were computed, and it showed excellent results for isolation of shadows within the vegetation (Chen et al., 2009). Moreover, two texture features (angular second moment (ASM) - uniformity, and inverse difference moment (IDM) - homogeneity) (Haralick, 1979) from both intensity image and thermal image were computed.

$$SSI = |R + B - 2 \times G| \tag{5.1}$$

where R, G, and B are red, green, and blue values respectively.

Segmentation

Segmentation and classification are the two main steps in OBIA (Silver et al., 2019). The segmentation is the first step and by definition "it divides an image or any raster or point data into spatially continuous, disjoint and homogeneous regions, referred to as segments or image objects" (Blaschke et al., 2014). According to Espindola et al. (2006), the quality of segmentation depends on the balance between intersegment homogeneity (the similarity between segments) and intersegment heterogeneity (the difference between segments).

Variance and spatial autocorrelation (Moran's I) between segments are utilised as measures to evaluate intersegment homogeneity and heterogeneity respectively. A low variance leads to over-segmentation of images, as very similar pixels are contained in each segment which divides one real-world object into many segments. In contrast, a low spatial autocorrelation between segments can increase the variance, and it causes under-segmentation, which gives one large segment that covers many different real-world objects. The segmentation threshold (also referred to as scale) can control the balance between intersegment variance and spatial autocorrelation. Therefore, finding the optimum threshold is essential to produce segments which are matching to the real-world objects (Espindola et al., 2006).

Johnson et al. (2015) established an F measure to identify the quality of the segmentation result for a given threshold value. The F measure is based on variance and spa-

tial autocorrelation and calculated using Equation 5.2 (Johnson et al., 2015). A weight value (a) must be defined in the F measure, with 0.5 is half weighting, and 2 is double weighting. Like the normalise sum measure, the higher the F measure, the higher the quality of the segmentation.

$$F = (1 + a^2) \left(\frac{MI_{norm} \times V_{norm}}{a^2 \times MI_{norm} + V_{norm}} \right) \tag{5.2}$$

here MI_{norm} is the normalised Moran's I value, V_{norm} is the normalised variance value, a is the alpha weight, and F is the F measure.

Espindola et al. (2006) introduced the Unsupervised Parameter Optimisation (USPO) procedure to identify the optimum threshold value for the given image from a range of threshold values based on one of the quality measures mentioned above. The USPO procedure was implemented as an add-on tool called *i.segment.uspo* in GRASS GIS software (Lennert and GRASS Development Team 2019a). The CHM raster, PD raster and hue image from HIS ortho-mosaic were used in the segmentation process (Figure 5.3). According to Georganos et al. (2018), finding the optimum threshold values for different local image regions gives superior results compared to the use of a single threshold for the whole image. Hence, the image was divided into sixteen small zones (15 zones overlapping with the 64 m^2 plots for each study plot and one zone for the paths between the plots). Specific local thresholds (ranging from 0.01 to 0.15) was determined for each region based on the F measure. The alpha value in the F measure calculation was kept at 0.5. Python *Jupyter Notebook* codes from Grippa (2018) were adopted and modified according to this study for automatizing the segmentation process using *i.segment.uspo* for each zone. The segmentation procedure was applied separately for each study plot and sampling date. A total of six different segmented raster were created according to six datasets.

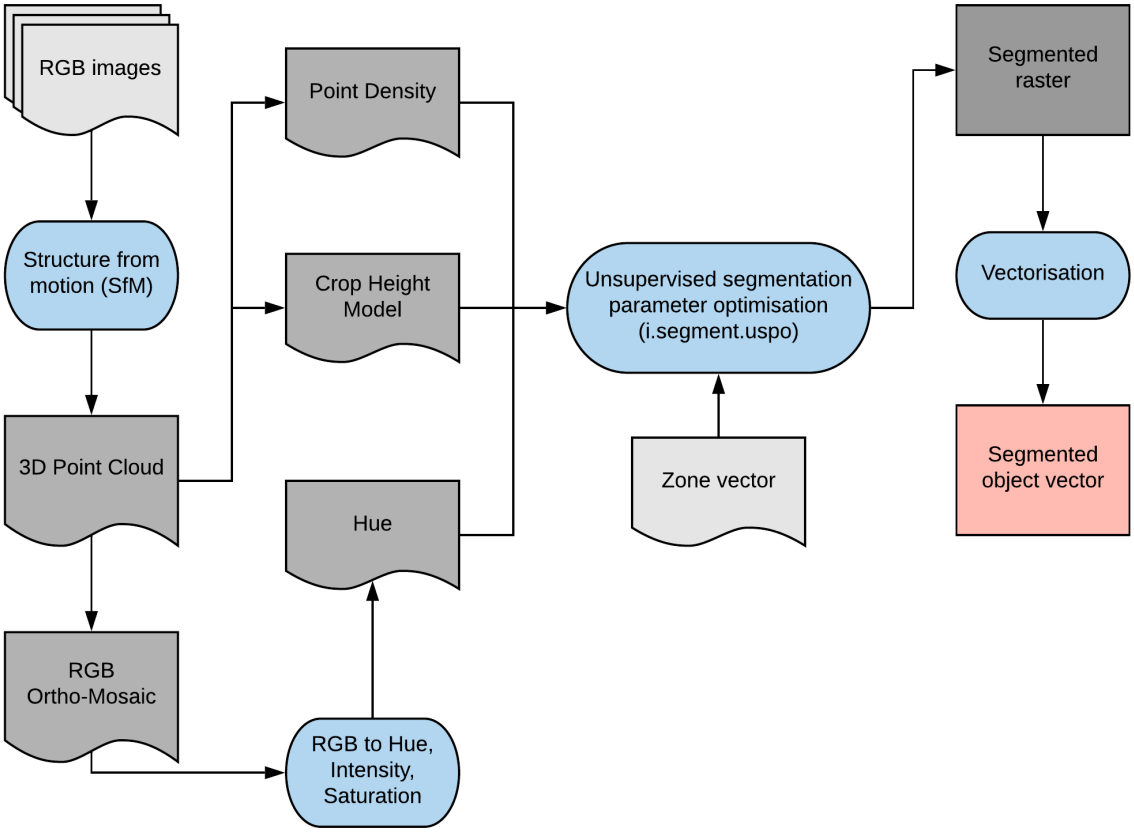

Figure 5.3: Flow diagram of the segmentation with *i.segment.uspo* and attribute calculation using GRASS GIS

Attribute calculation for segmented image objects

The segmented raster was vectorised, and each segmented object was created as a polygon. Four geometric attributes (area (A), perimeter (P), fractional dimension (FD) (Equation 5.3), and circle compactness (CC) (Equation 5.4)) for the segmented objects were calculated. Based on all raster data (RGB image, HIS image, CHM raster, PD raster, thermal image, SSI image, and texture raster), the mean and standard deviation values for each polygon was computed as image-based attributes. Attribute calculation was done using *i.segment.stats* add-on in GRASS GIS (Lennert and GRASS Development Team, 2019; GRASS Development Team, 2017). In total, 32 attributes (4 geometric and 28 image-based) were generated (Table 5.1).

$$FD = 2 \times \left(\frac{\log P}{\log A + 0.001} \right) \tag{5.3}$$

$$CC = \frac{P}{2 \times \sqrt{\pi \times A}} \tag{5.4}$$

Table 5.1: Description of the calculated object's attributes. (SD: Standard deviation

ID	Attribute	Description
1	Area	Area of the object
2	Perimeter	Perimeter of the object
3	FD	fractional dimension of the object
4	CC	circle compactness of the object
5	Mean R	Mean red image value of the object
6	Mean G	Mean green image value of the object
7	Mean B	Mean blue image value of the object
8	Mean hue	Mean hue image value of the object
9	Mean intensity	Mean intensity image value of the object
10	Mean saturation	Mean saturation image value of the object
11	Mean intensity ASM	Mean intensity ASM texture image value of the object
12	Mean intensity IDM	Mean intensity IDM texture image value of the object
13	Mean SSI	Mean spherical shape index image value of the object
14	Mean temperature	Mean temperature value of the object
15	Mean thermal ASM	Mean thermal ASM texture image value of the object
16	Mean thermal IDM	Mean thermal IDM texture image value of the object
17	Mean CHM	Mean canopy height value of the object
18	Mean PD	Mean point density value of the object
19	SD R	SD of of red image value of the object
20	SD G	SD of gree image value of the object
21	SD B	SD of blue image value of the object
22	SD hue	SD of hue image value of the object
23	SD intensity	SD of intensity image value of the object
24	SD saturation	SD of saturation image value of the object
25	SD intensity ASM	SD of intensity ASM texture image value of the object
26	SD intensity IDM	SD of intensity IDM texture image value of the object
27	SD SSI	SD of spherical shape index image value of the object
28	SD temperature	SD of temperature value of the object
29	SD thermal ASM	SD of thermal ASM texture image value of the object
30	SD thermal IDM	SD of thermal IDM texture image value of the object
31	SD CHM	SD of canopy height value of the object

32	SD PD	SD of point density value of the object

Classification model

Ten percent of the segmented objects (3698 out of a total of 81704 objects) were manually labelled as either lupine (L) or non-lupine (NL) based on visual observation using the RGB ortho-mosaics. In each dataset, the number of L and NL labels were very similar (L = 1892 and NL = 1806), and labelled objects were spatially randomised. The labelled objects with attributes were utilised to develop a supervised classification model.

Classification model training and testing were conducted using R statistical software (R Core Team, 2019). The random forest (RF) machine learning classification algorithm was employed to build a classification model using the *mlr* package in R software (Bischl et al., 2016). The RF has proven its efficiency for image object classification using objects' attribute data (Belgiu and Drăgu, 2016). The RF algorithm utilises both decision trees and bagging (Breiman, 2001). The decision trees are created from a subset of the training samples with replacement (known as bagging). Based on the average decision of the trees, the sample is assigned to different classes (Belgiu and Drăgu, 2016).

A total of six RF classification models were built, and in each model, five datasets were employed to train the model, while the remaining dataset was used to test the model (Table 5.2). All the attributes (32) were employed as an input of the model alone with objects' labels. Two hyperparameters, namely *mtry* (number of selected variables in each split) and node size (number of observations in a terminal node) (Probst et al., 2019), were tuned in the model training phase using random search. The model was trained with repeated spatial cross-validation resampling (five-folds and two repeats) to classify objects. Resampling is based on the location of the observations to reduce the effect of spatial autocorrelation for model accuracy (Brenning, 2012). The location was based on the centroid of the objects. The trained model employed to predict objects' labels of the holdout. According to predicted labels and actual labels, the model performance was evaluated by calculating overall accuracy (OA), true-positive-rate (TPR), false-positive-rate (FPR), and Kappa (K) values (Equation 5.5, 5.6, 5.7, and 5.8 respectively).

$$OA = \frac{TP + TN}{TP + FN + FP + TN} \tag{5.5}$$

$$TPR = \frac{TP}{TP + FN} \tag{5.6}$$

$$FPR = \frac{FP}{FP + TN} \tag{5.7}$$

$$K = \frac{Observed\ agreement - Expected\ agreement}{1 - Expected\ agreement} \tag{5.8}$$

Where TP is true positives, TN is true negative, FP is false positive, and FN false negative.

Table 5.2: Details of the training and testing datasets for different classification models.

Model name	Datasets for training	Dataset for testing
M11	D_1G_2, D_2G_1, D_2G_2, D_3G_1, D_3G_2	D_1G_1
M12	D_1G_1, D_2G_1, D_2G_2, D_3G_1, D_3G_2	D_1G_2
M21	D_1G_2, D_1G_2, D_2G_2, D_3G_1, D_3G_2	D_2G_1
M22	D_1G_2, D_1G_2, D_2G_1, D_3G_1, D_3G_2	D_2G_2
M31	D_1G_2, D_1G_2, D_2G_1, D_2G_2, D_3G_2	D_3G_1
M32	D_1G_2, D_1G_2, D_2G_1, D_2G_2, D_3G_1	D_3G_2

5.2.4 Lupine coverage mapping

A single RF classification model (M_{all}) was trained using all labelled objects from the six datasets. Based on predicted labels from Mall, a lupine coverage map was generated (hereafter referred to as classification-based lupine coverage map).

A reference lupine coverage map for each dataset was created by digitising each RGB ortho-mosaic and was compared to the lupine area from the classification-based lupine coverage map. A relative number of no-difference pixels from two maps was computed as a measure for map accuracy (MA) (Equation 5.9). Additionally, the pixel-wise Person's correlation coefficient (PCC) was calculated. Each 64 m^2 plot was divided into four equal areas of 16m^2 each, and the relationship between relative digitised lupine area (LA) and MA of subdivided plots was analysed to understand the MA at different levels of LA.

$$MA = \frac{Number\ of\ equally\ categorised\ pixels\ in\ the\ two\ maps}{Total\ number\ of\ pixels} \tag{5.9}$$

5.3 Results

5.3.1 Image segmentation

Ortho-mosaics from RGB and thermal camera images were created in this study and SSI, and hue images were computed from the RGB ortho-mosaic. RGB images were processed with SFM technique to generate CHM raster and PD raster. Exemplary images and raster from D1 of G1 are shown in Figure 5.4.

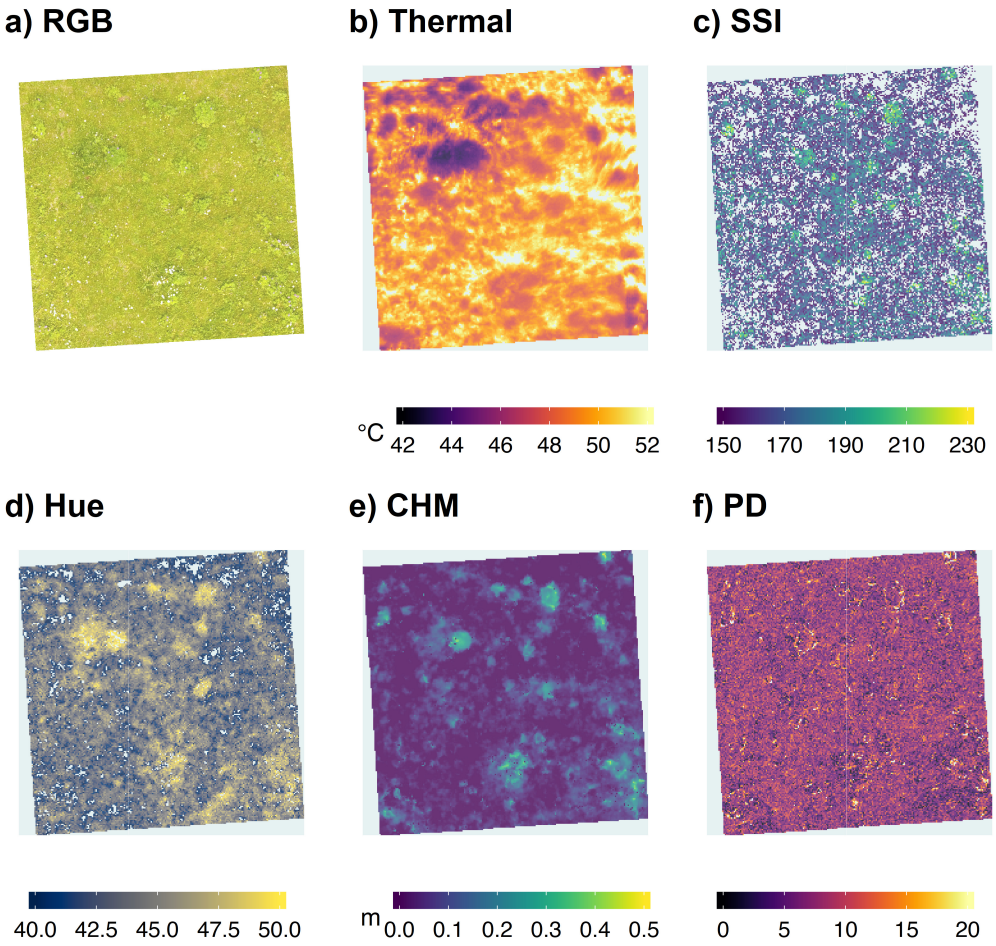

Figure 5.4: Exemplary images for D_1G_1 (Field G1, 12th June) dataset (a) RGB digital ortho-mosaic, (b) Thermal digital ortho-mosaic, (c) spectral shape index (SSI) image, (d) hue image, (e) canopy height model (CHM) raster, and (f) point density (PD) raster

The CHM raster, PD raster, and hue image were utilised to create image objects. The optimum threshold values for different image regions were determined using USPO. As shown in Figure 5.5, three image regions with different vegetation maturity obtained distinct optimum threshold values. Example segmented image is shown in the Appendix Figure 5.9.

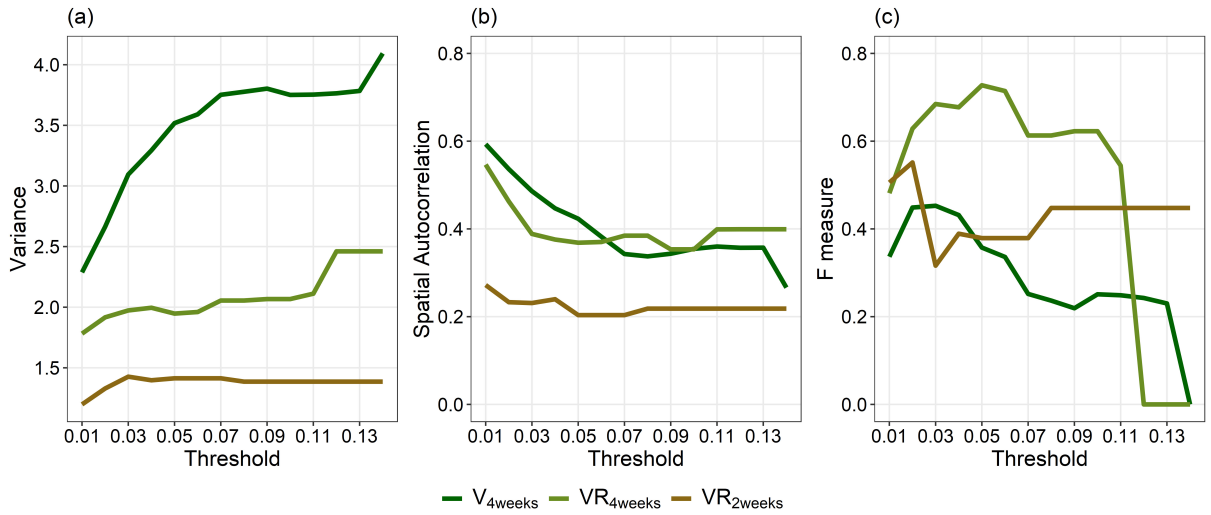

Figure 5.5: Course of (a) variance, (b) spatial autocorrelation, and (c) F measure values for different threshold values in three different image regions where VR_{4weeks}: regrown vegetation 4 weeks after mowing, VR_{2weeks}: regrown vegetation 2 weeks after mowing, and V_{4weeks}: vegetation four weeks older than 12th June vegetation

5.3.2 Classification model training and testing

Six classification models were trained while holding out one dataset at each time. The model results are summarised in Table 5.3. Based on the all performance measures in model testing phase, model M12 (model tested with D1G2 data) obtained the lowest performances (OA = 78.2 %, K = 0.55) and model M32 (model tested with D3G2 data) achieved the highest values (OA = 97.2 %, K = 0.94). Although model M12 accurately classified all lupine objects (100 % TPR), it also categorised nearly half of the non-lupine objects as lupine objects (47.3 % FPR). Additionally, models that tested with D1 data (M11 and M12) obtained slightly lower performances compared to other models.

Table 5.3: Classification model results. L: lupine, NL: non-lupine, TA: training accuracy, OA: overall accuracy, K: Kappa statistics, TPR: true positive rate, FNR: false negative rate.

Model	Training	Testing				
	No. of objects	No. of objects	OA (%)	TPR (%)	FPR (%)	K
M11	L = 1581 NL = 1545	L = 311 NL = 261	83.2	76.8	9.2	0.67
M12	L = 1394 NL = 1381	L = 498 NL = 425	78.2	100.0	47.3	0.55
M21	L = 1578 NL = 1429	L = 314 NL = 377	90.6	84.1	4.0	0.81
M22	L = 1701 NL = 1638	L = 191 NL = 168	96.4	95.8	3.0	0.93
M31	L = 1530 NL = 1405	L = 362 NL = 401	90.1	88.4	6.7	0.82
M32	L = 1676 NL = 1632	L = 216 NL = 174	97.2	96.7	2.3	0.94

5.3.3 Final classification model and important attributes

After testing six classification models with the different spatial-temporal dataset, the complete classification model (M_{all}) was trained using all available data (3698 objects) with spatial cross-validation. The M_{all} model achieved 94.2 % training accuracy.

The importance of the objects' attributes to the M_{all} classification model was assessed based on the mean decrease Gini value (Figure 5.6). It is based on "the total decrease in node impurities from splitting on the variable, averaged over all trees" (Liaw and Wiener, 2002). The six most important variable of the model were *Mean CHM*, *SD SSI*, *Area*, *SD CHM*, *Perimeter*, and *Mean hue* attribute values. Attributes related to texture features were the least essential prediction variables to the M_{all} model.

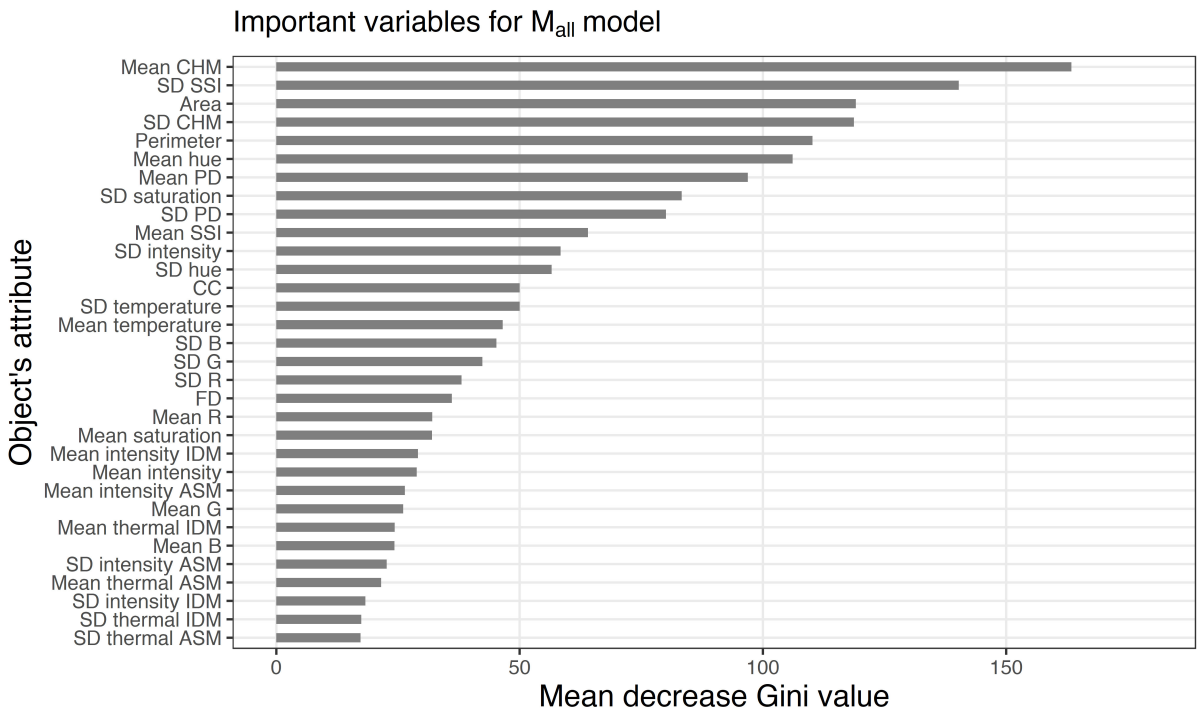

Figure 5.6: Important object's attributes for the M_{all} classification model (complete model) based on mean decrease Gini values.

5.3.4 Lupine coverage maps

Based on visual observation between digitised lupine map and classified lupine map, both maps showed similar visual representation. Figure 5.7 illustrates lupine coverage maps from both digitising and classification for three sampling dates (D1, D2, D3) in G1 field. However, the area-based comparison showed maximum ±5 % of the change in total lupine coverage (Table 5.4).

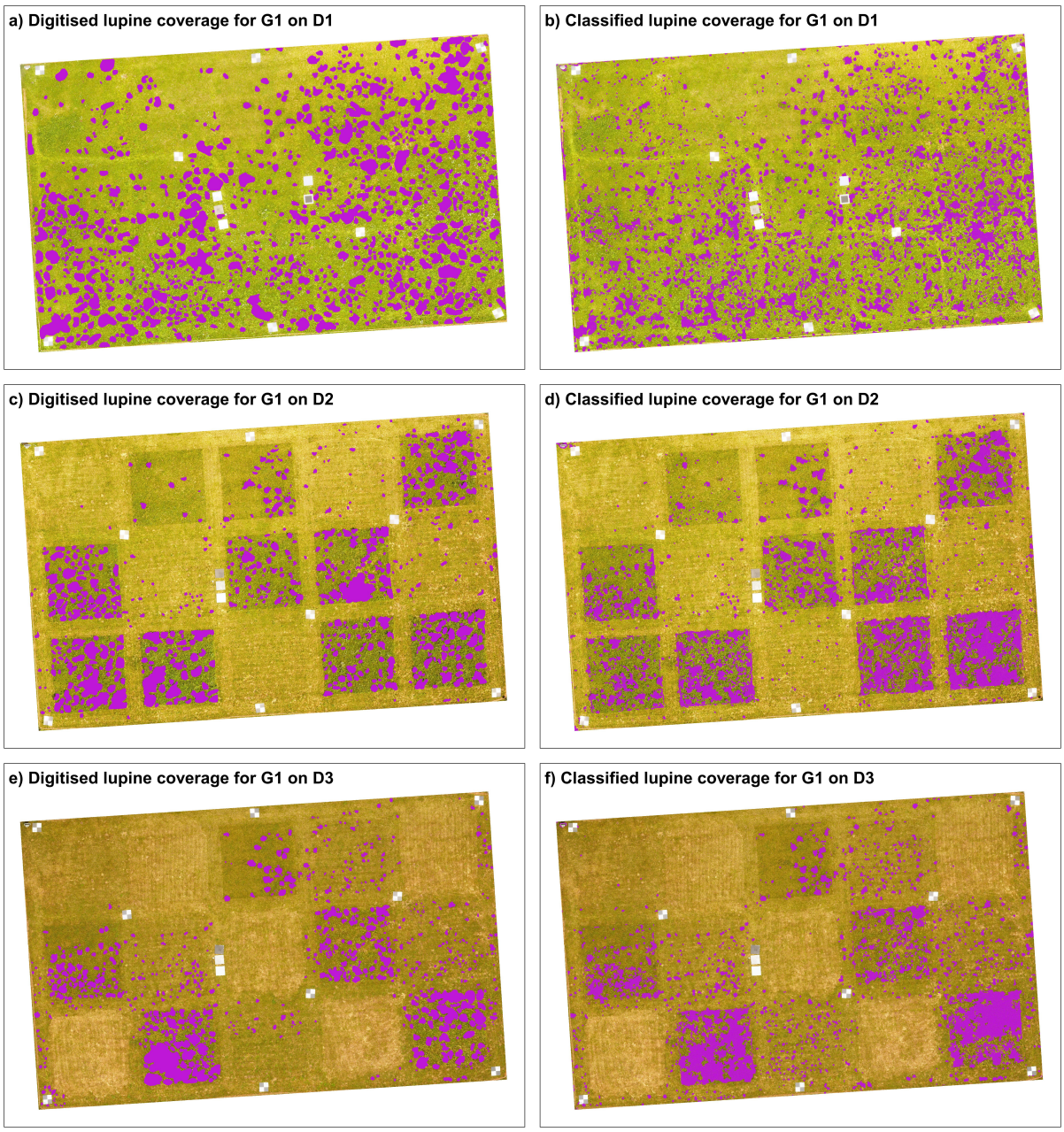

Figure 5.7: Lupine coverage map of the G1 field with a, c, e, showing manually digitised lupine cover (purple) at D1 (12th June), D2 (26th June), and D3 (9th July) and b, d, f, showing lupine cover classified by UAV-borne RS data and OBIA.

Table 5.4: Pixel-based comparison between manually digitised and classified lupine coverage. MA: map accuracy, PCC: pixel-wise Pearson's correlation coefficient.

Date	Field	Lupine area (m^2)	Relative lupine area difference (%)	MA (%)	PCC
D1	G1	294	-5	80.4	0.40
	G2	443	+3	80.9	0.50
D2	G1	237	+1	88.7	0.52
	G2	308	+3	89.0	0.61
D3	G1	188	+2	93.1	0.63
	G2	181	+2	93.8	0.65

The classification based lupine coverage was assessed against reference lupine coverage map using comparing pixels in two raster maps. From comparison results, map accuracy relative to the reference map and CC was computed (Table 5.4). According to raster comparison results, D1 dataset obtained the lowest MA (80.4 %, 80.9 %) and PCC (0.40, 0.50) values in G1 and G2 fields respectively. The MA and PCC values tended to increase with reducing lupine coverage. However, comparison results for G2 dataset always indicated slightly better results than G1.

Relationship between the relative LA and MA indicated a negative exponential trend (Figure 5.8). The correlation coefficient between relative LA and MA was -0.88, and trend line had 0.80 goodness of fit. Regardless of the vegetation maturity, the explained relationship was valid. Until LA reached 25 %, it showed a strong relationship with MA, but over 25 % LA the MA values were scattered around the regression curve.

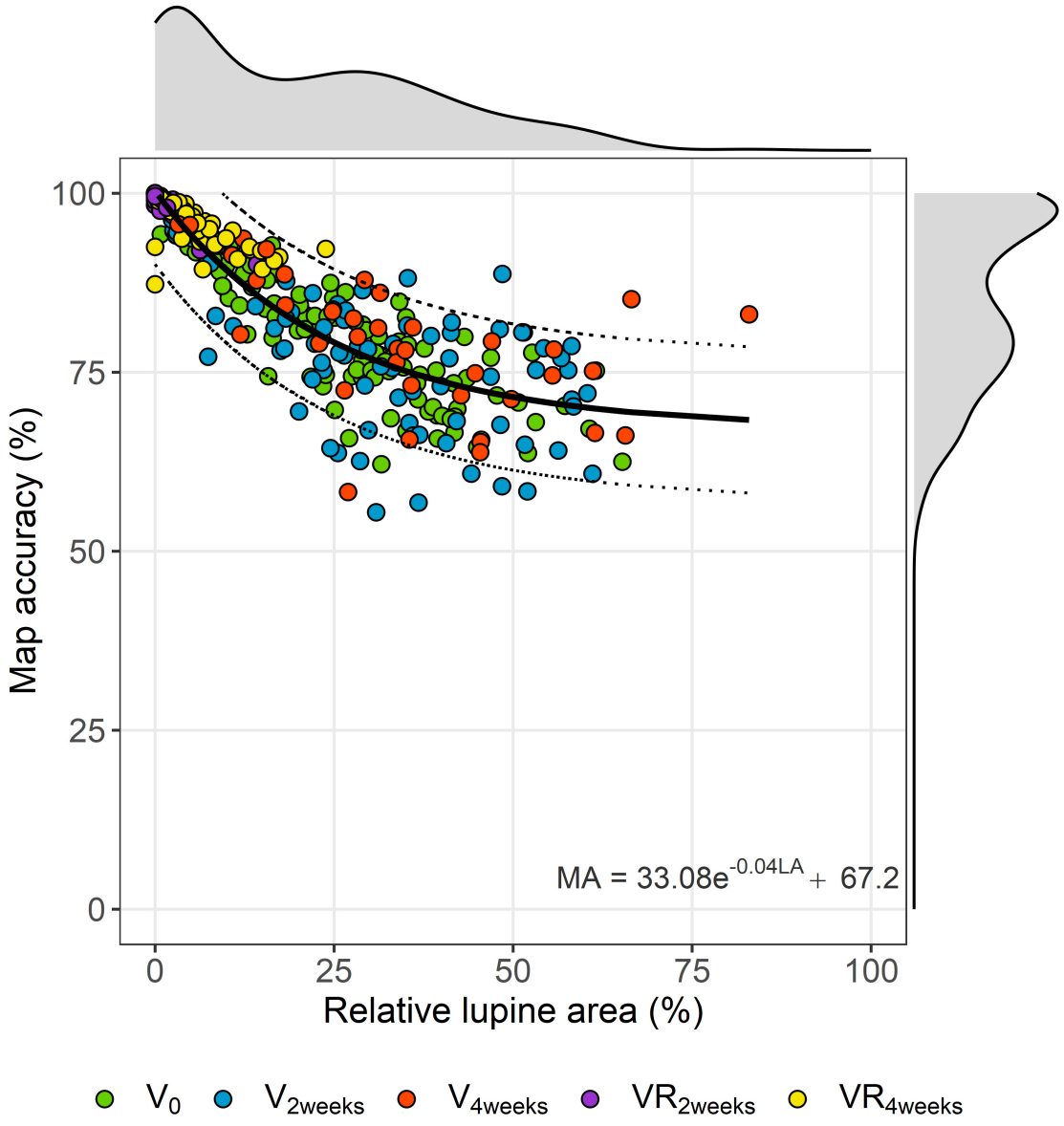

Figure 5.8: The relationship between relative lupine area (LA) from manual digitising and map accuracy (MA) based on the generalised model, comprising undisturbed/not mowed vegetation (V_0, V_{2weeks}, V_{4weeks}), and regrown vegetation after mowing (VR_{2weeks}, VR_{4weeks}). Grey areas indicate the data density along the x- and y-axis. The black line represents the fitted exponential curve, and dotted lines show the 95th confidence interval of the fitted curve.

5.4 Discussion

Invasion by lupine endangers biodiversity and ecosystem functionality (Klinger et al., 2019). The spatial and temporal distribution of lupine is essential to understand the invasive pattern, to plan appropriate management strategies and to monitor the impact of control actions. While RS was utilised to map several invasive plant species (e.g. *Impatiens glandulifera*, *Spartina anglica*, *Solidago canadensis*), invasion patterns of lupine

were not examined until now (Skowronek et al., 2018). This study aimed to develop an operational workflow to map the spatial distribution of invasive lupine in grasslands using UAV-borne imageries and OBIA.

OBIA has shown its' effectiveness to work with very high-resolution (<1 m spatial resolution) images, where several pixels represent one object rather than classifying each pixel separately. While OBIA allowed taking advantage of RGB images only, a pixel-based classification approach would have demanded spectral signatures. Segmentation is the critical step in the OBIA. The first step of the proposed workflow was to segment collected UAV-borne images into image objects that represent either lupine or non-lupine (i.e. mainly grass) plants. USPO based area-specific threshold values benefitted for obtaining good object delineation (Figure 5.5). However, USPO for a multitude of image areas leads to an increased computational time corresponding to the size of the areas and the spatial resolution of the images (Georganos et al., 2018).

Apart from optimal threshold identification, different combinations of various raster types were tested (data not shown). Visual assessment of the segments obtained suggested that the combined raster with CHM, PD and hue data provided the best segmentation results. This is comprehensible, as the canopy height of lupine plants is usually taller than the surrounding grass vegetation (Otte and Maul, 2005), also resulting in higher point densities at the edges of the lupine plant than in the plants' centres. Therefore, CHM and PD raster data significantly contributed to the delineation of objects and the contour like pattern can be seen from segmented raster (Appendix Figure 5.10). CHM data has been utilised recently as classification variable for invasive species mapping (Jones et al., 2011; Lehmann et al., 2017), but this is the first study where CHM data was employed to delineate objects in invasive species mapping. Additionally, hue data derived from RGB images characterised the degree of pureness of the colour compared to the primary colours (Gonzalez and Woods, 2008) also assisted in defining object boundaries.

Random forest classification models with 32 attributes as predictors were trained and tested based on different datasets. The model M12 obtained the highest TPR but got the lowest FPR and tended to over-classify non-lupine objects as lupine objects. As the M12 model was tested with datasets containing only young lupine plants, small objects that were not lupine may have been overestimated. This may also be true for the M11 model, which had a similarly low accuracy compared to the other models. Overall, the performance of the six models showed high model stability and robustness across time and space, which indicates that the models could be transferred easily to other grassland sites of varying maturity. As demonstrated with previous studies (Belgiu

and Drăgu, 2016), our results confirmed that RF modelling creates robust algorithms to use object classification in OBIA for vegetation mapping.

Several attributes related to plant structure or architecture as well as colour were essential predictors in the M_{all} model. The height difference between lupine plants and grass vegetation contributed to the classification of segmented objects. It points at a prominent advantage of UAV-borne RS, which allows the separation of two plant types by CHM attributes. This was also proven by other studies that utilised CHM from UAV-borne RS data to map invasive species mapping, i.e. *Phragmites australis* in estuaries by Abeysinghe et al. (2019) and *Fallopia spp.* in floodplains by Martin et al. (2018).

Segment's area and perimeter were further vital geometric features in the final classification model, whereas fractional dimensions and circle compactness were not useful. A closer look at the segmented objects shows that area (average values were 0.04 m^2 and 0.17 m^2 for L and NL objects respectively) and perimeter (average values were 1.6 m and 3.5 m for L and NL objects respectively) of lupine objects were substantially smaller compared to non-lupine objects, irrespective of the lupine coverage (Appendix Figure 5.10). The automated process segmented lupine objects always in relatively small areas even when large parts of the area were covered by lupine. Our findings confirm results from other studies, where area and perimeter were essential variables in discrimination models, e.g. species mapping in arid areas as demonstrated by Silver et al. (2019).

To reduce the computation complexity, only two texture parameters (angular second moment, inverse difference moment) were computed out of many existing parameters. Surprisingly, all four texture attributes (intensity-based and thermal-based) were ineffective in our study. Previous studies (Chabot et al., 2018; Silver et al., 2019) with OBIA have proven that textural information was useful. However, they utilised many more texture attributes than employed in our study. Hence, the accuracy of our models might be increased by including further texture parameters.

Corresponding to the intense green colour of lupine leaves and pronounced red and blue shades of flowers, SSI values computed from RGB intensities indicated higher values in leafy areas and lower values in regions, where flowering lupine dominated. Consequently, an increased cover of lupine plants at different maturity stages resulted in increased standard deviations of SSI, due to a broader distribution of the SSI values (Appendix Figure 5.10). This may explain why the variation of standard deviation values among objects supported the categorisation of lupine and non-lupine objects.

As lupine plants contain higher water contents compared to grasses (Hensgen and Wachendorf, 2016), lupine containing areas in thermal images showed lower temper-

atures compared to the surrounding grass area (Figure 5.4). Additionally, the bushy structure of lupine plants creates shaded areas in the surrounding, which may have further decreased temperature. Surprisingly, temperature-related attributes (temperature or texture attributes from thermal image) did not become significant predictors in the classification models. Evidently, other predictors were of superior relevance than the temperature attributes. However, this leads to reduced costs for sensors and platforms as well as model complexity and computing time.

As relative LA increased, the MA of the lupine coverage maps that generated from our workflow decreased (Figure 5.8). The negative relationship was valid for both undisturbed vegetation of different maturity and regrown vegetation after mowing. With an increasing lupine area, the classification procedure tends to over-estimate lupine coverage due to difficulty to separate lupine and grass vegetation. In general, early detection of invasive plant species and rapid action is critical to control invasive species (Cock and Wittenberg, 2001). Similarly, for lupine management activities, ecologists prefer to act in regions with lower lupine coverage, as at this stage of invasion, eradication and containment are easier than high lupine coverage regions. Since maps with lower lupine coverage were accurate, ecologists can identify regions with relatively small lupine coverage and precisely locate single lupine plants for eradication.

Though it could be shown that the proposed method performed as well as the standard digitising method, it may be criticised that vegetation mapping based on UAV-borne RS data is challenging to scale up (e.g. Chabot et al. (2018)). In this study, one UAV flight took 20 minutes (including ground preparation and flight time) to collect data of approximately 0.4 hectares (without thermal sensor). The conduction of additional flight sessions, as well as expected advance in sensor and platform technology, may lead to an increased data acquisition area in the future. The proposed method can be considered cost-efficient, as it only requires a standard UAV-mounted RGB camera, and as most of the utilised software is free and open-source (GRASS GIS, R, QGIS), except the Agisoft PhotoScan software, which could be replaced with available free software (e.g. open drone map).

Our proposed classification approach can easily be applied in other comparable environments, as the model was trained with heterogeneous datasets from commonly occurring grassland vegetation at different stages of maturity. The spatial lupine coverage maps that were created can be utilised i) to identify the distribution of lupine in grasslands, ii) to estimate the size and degree of lupine invasion by comparing maps generated in different years, and iii) to evaluate the effectiveness of lupine control. As suggested by Kattenborn et al. (2019), UAV-borne lupine coverage maps can further

be employed for the creation of field samples to train and test satellite image-based models for invasive lupine mapping in larger areas.

5.5 Conclusions

Gaining knowledge on the spatio-temporal distribution of lupine is vital to maintain biodiversity in grasslands which are threatened by the invasion of this plant. We successfully developed a workflow that can accurately map lupine coverage in a grassland using UAV-borne RS and OBIA. In our proposed workflow, we developed a robust RF classification model that can classify lupine and non-lupine image objects. The resulting maps showed a ±5 % discrepancy in the lupine area compared to the standard digitising method. Moreover, the classification model can be transferred to other regions, and thereby overcomes limitations of the standard way of lupine mapping. Finally, the developed procedure can be adopted for mapping other invasive species.

Appendix

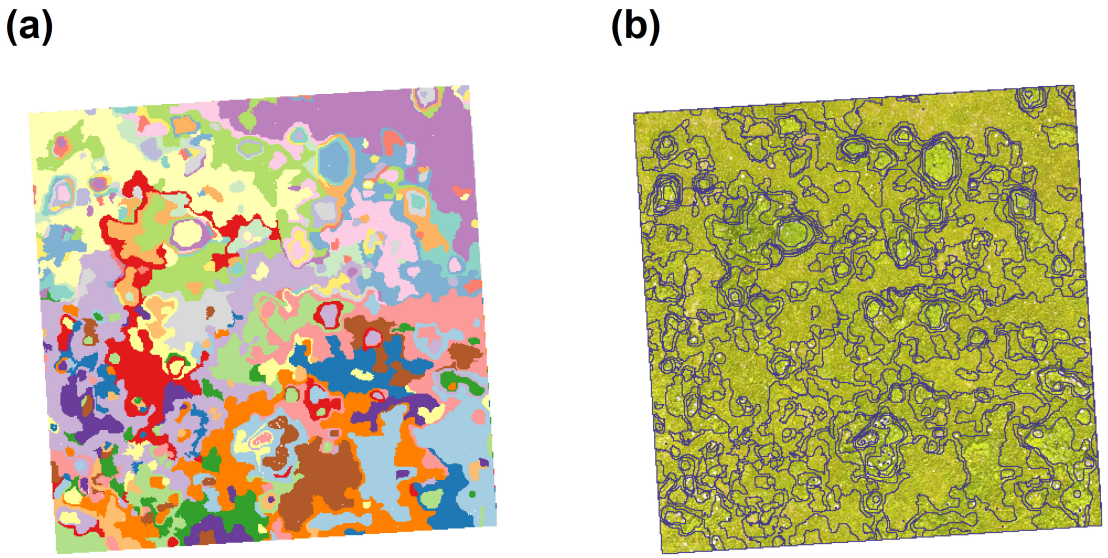

Figure 5.9: Subset of the (a) segmented object raster (unique colour represents a single segmented object and colours are repeated), and (b) vectorised segmented object overlay with RGB image for G_1D_1 (Field G1, 12th June) dataset

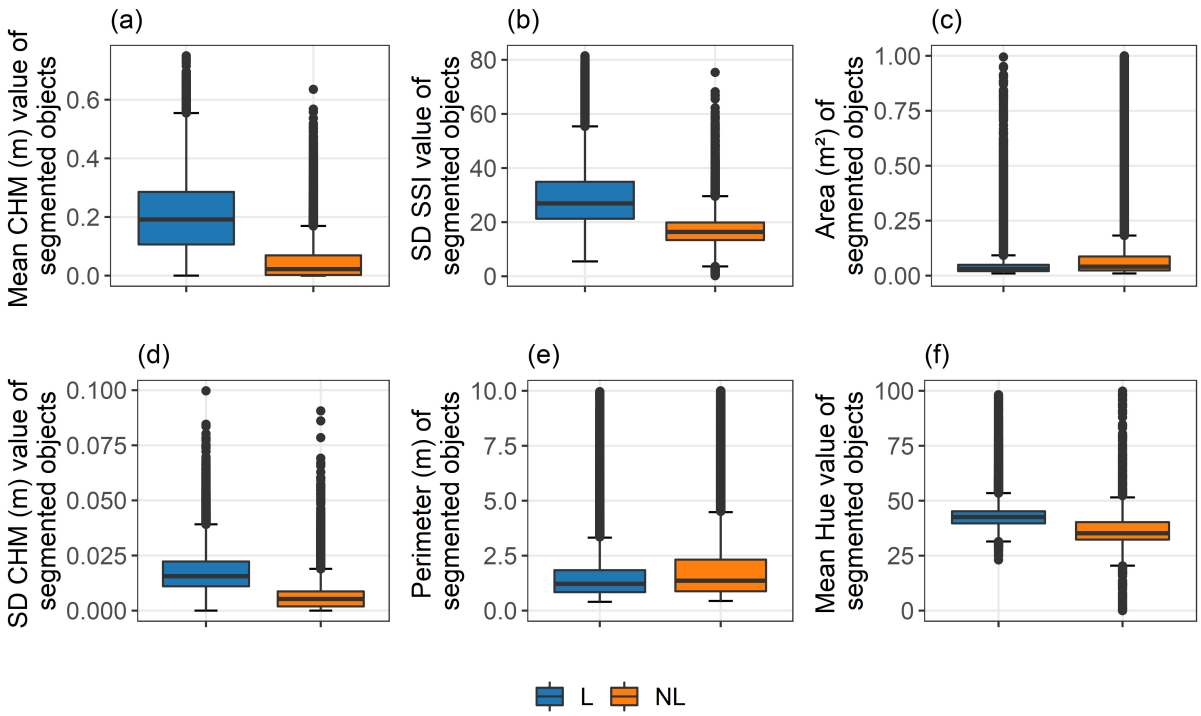

Figure 5.10: Distribution of the values of the most six significant predictors in the classification model for lupine (L), and non-lupine (NL) category. (a) mean canopy height model values, (b) standard deviation values of spectral shape index, (c) area values, (d) standard deviation values of canopy height model, (e) perimeter values, and (f) mean hue values

The content of Chapter 5 has not been changed from the original submitted version.

Wijesingha, J., Astor, T., Schulze-Brüninghoff, D., Wachendorf, M., Mapping invasive *Lupinus polyphyllus* Lindl. in semi-natural grasslands using object-based analysis of UAV-borne images. (Manuscript submitted for publication in Journal of Photogrammetry, Remote Sensing and Geoinformation Science on 08 January 2020)

Chapter 6

General discussion

According to Frame and Laidlaw (2011), attention to detail is vital for effective grassland management. To achieve great details in grassland monitoring, sampling unit size (grain) must be smaller (t'Mannetje and Jones, 2000). Ground-borne observations can obtain fine grain but covering a broader geographic area (extent) requires a lot of time and labour. UAV-borne RS observations provide fine-grain (high spatial resolution) data due to low-altitude flight. Furthermore, UAVs can effortlessly cover a greater spatial extent (e.g. grassland field or paddock level) compared to ground-borne observations.

In the last few years, UAV-borne RS has been employed for fine-scale (small extent in fine-grain) vegetation monitoring including grasslands. Most of the studies that demonstrated UAV-borne RS for fine-scale grassland monitoring focused on the experimental grassland conditions or on a single grassland type. Thus, this whole study addressed the applicability of UAV-borne RS for monitoring and mapping grassland in fine-scale in a multitude of grassland types under actual field conditions. Estimating grassland biomass, grassland forage quality values and classifying invasive species in grasslands were considered as applications in this study using UAV-borne RS.

In the first part (6.1) of the following discussion, the results from each chapter combining the corresponding sub-objectives of the whole study are discussed. The potential applications from this thesis outcomes are discussed in the second part (6.2) of this discussion. Finally, limitations and possible improvements (6.3) for fine-scale grassland monitoring using UAV-borne RS are discussed.

6.1 Biomass, forage quality estimation and invasive lupine mapping in grasslands

The sward height is an essential structural measure for grassland management decision (Hopkins, 1999). Chapter 3 described CHM derived from UAV-borne images using SFM technique (hereafter referred to as UAV SFM) which can be another technique to measure grassland sward height other than existing methods such as ruler (Williamson et al., 1987), disk pasture meter (Santillan et al., 1979), ultra-sonic measurement (Fricke et al., 2011), and TLS (Schulze-Brüninghoff et al., 2019). The CHM derived from UAV SFM underestimated actual field measured height due to small sward structure and high mobility of grass swards due to wind (Cunliffe et al., 2016). Apart from vegetation formation, depth filtering during the SFM could also remove extreme points where it might represent actual swards of grasses. It was confirmed by the results in Chapter 3, where TLS provided taller sward height compared to UAV SFM (average sward height was 0.21 m and 0.18 m for TLS and UAV SFM respectively). As reported by Bendig (2015), this is a common drawback of UAV SFM based CHM developed for arable crops (e.g. rice) also.

The CHM derivation from UAV SFM involved two primary height models, namely the digital surface model (DSM) and the digital terrain model (DTM). The DSM represents the vegetation canopy surface, whereas the DTM acts as a reference plane which contains only the base layer without vegetation. Thus, the precision of the CHM is always reliant on the precision of DTM and DSM. When subtracting two height models, the positional accuracy of the two models could affect the accuracy of the output CHM. This could occur if the sources of the two height models are different. To calculate CHM from UAV SFM data in Chapter 3, the DTM from TLS and DSM from UAV SFM were utilised. Due to slight changes in the horizontal position of the two height models, inaccurate canopy height values were observed in some regions. On the contrary, two UAV SFM data sets were utilised as DSM and DTM to compute CHM in Chapter 5 with the experience from Chapter 3. Hence, those errors were not observed in the CHM calculated in Chapter 5. 3D point clouds with vegetation could be classified into ground points and vegetation points using terrain filtering methods avoiding a need for two data sets for CHM generation (Dandois and Ellis, 2013). However, this method only works when the ground area can be recognised clearly in the images. In grasslands, it is difficult to see bare ground areas due to dense sward canopy, so this method did not work for our studies.

In Chapter 3, the field samples represented 1 m^2 area. Hence the most correlated sward height metric from 1m^2 area (e.g. mean, max, median, percentiles) against grassland

fresh and dry biomass (FB and DB) were identified. The most robust relationship between grassland biomass was shown by the 75th percentile (p75) sward height (average correlation coefficient = 0.7). Similarly, 80th and 90th percentile sward height values showed the highest correlation coefficient with grassland biomass in the experiment conducted by Viljanen et al. (2018). Conversely, Grüner et al. (2019) demonstrated mean sward height obtains the highest relationship with grassland biomass. This explains the fact that it is necessary to check various sward height metrics to identify the best candidate as a proxy for biomass estimation.

Three different levels of biomass estimation models were built in Chapter 3, which were i) harvest-specific, ii) grassland-specific, and iii) global models with all data points. The DB estimation models obtained average nRMSE of 19.5 %, 27.1 %, and 36.2 % respectively at three mentioned modelling levels. The species richness and related spatial heterogeneity of grassland were increasing from harvest-specific to global models. Therefore, model performances were decreasing in the same order. The same pattern was observed from models that were generated using TLS data. Our results imply that using solely sward height could not be enough to model biomass under complex grassland conditions. There might be a necessity for additional data such as spectral characteristics which was already suggested by Fricke and Wachendorf (2013). The RGB camera was employed in our study; hence spectral data was limited. However, the combination of CHM from UAV SFM and RGB values showed improved results in an experimental grassland setup (Viljanen et al., 2018). Generally, Chapter 3 effectively investigated the usage of CHM derived from UAV-borne images for estimating grassland biomass, which was the first sub-objective of this study.

UAV-borne imaging spectroscopy data and machine learning regression were utilised for estimating two important forage quality parameters (CP and ADF) in a multitude of grasslands in Chapter 4. The relationship between spectral reflectance and forage nutritional values has been widely employed for modelling forage chemical concentrations (Curran, 1989). Results in Chapter 4 showed that CP and ADF could be estimated with less than 15 % relative error regardless of the grassland type. These model performances were comparable to the forage quality estimation models from field spectroscopy data (Kawamura et al., 2008; Pullanagari et al., 2012; Safari et al., 2016b).

Chapter 4 highlighted that single spectral features (single wavebands, NDSI, SR) did not show a strong relationship with CP or ADF. Thus, the combination of full-spectral data and ML aided to grasp the variety of different grasslands and to provide accurate models. Following previous studies (Singh et al., 2017; Pullanagari et al., 2018), ML regression was employed due to multicollinearity of spectral reflectance data and

the possibility to use all spectral bands. Besides, several ML regression algorithms were compared to find out the best performing algorithm because there is no single algorithm that consistently delivers excellent results for every data set (Yuan et al., 2017). The ML algorithm comparison showed the most popular algorithm (PLSR) that utilised with spectral data being outperformed by all other employed algorithms (CBR, SVR, GPR, RFR). Furthermore, the identified best two ML regression algorithms (CBR, SVR) have not been employed for forage quality estimation, which verified that it is critical to assess more than one ML algorithm.

2D images from imaging spectroscopy data were processed to create forage quality maps that visualised the spatial distribution of CP and ADF. Those maps displayed forage quality data based on actual measured reflectance values. Hence, they contain lower inaccuracies compared to the interpolated maps, which could contain uncertainties from interpolation. The spatial pattern of the forage values from the maps could be utilised for identifying an underlying relationship between forage nutritional values and species composition or other factors such as soil moisture and grazing intensities. Moreover, an examination of multi-temporal maps would explain the link between quality values and regrown grasses after mowing or grazing activities. Overall, this verified that low-altitude spectral images with fine grain from UAV could be utilised for forage quality estimation as an alternative to standard field-based methods. Hence, it indicates that our second sub-objective was fruitfully accomplished

UAV-borne RS data was employed to map invasive lupine in semi-natural grasslands in Chapter 5. To get the full advantages from very high spatial resolution images (less than 1m the spatial resolution) from UAV-borne images, OBIA was exploited. Additionally, OBIA allowed taking the maximal benefits of RGB images (Silver et al., 2019). The canopy height variation between lupine and non-lupine vegetation was the critical variable in both segmentation and classification steps. Straightforward derivation of CHM using UAV-borne images provided an extra data component for invasive species classification, which was also demonstrated by several previous studies in different habitats (Martin et al., 2018; Abeysinghe et al., 2019).

Two ML classification algorithms (RF and C5.0) were tested in the study in Chapter 5. Results were only shown for RF because the models based on the C5.0 algorithm showed almost similar results. Generally, spatial autocorrelation can be found in RS data. Moreover, if dealing with time-series RS data, there is temporal autocorrelation in addition to spatial autocorrelation (Meyer et al., 2019; Rocha et al., 2019). Prediction models that used data featured by spatial or temporal autocorrelation can result in higher performance due to the autocorrelation effect. It is recommended to train

and test models with spatio-temporal cross-validation to obtain actual model performance without auto-correlation effect (Meyer et al., 2019). In Chapter 5, six different RF classification models were trained and tested. In each model, five spatio-temporal data sets were used to train the model, and the hold-out spatio-temporal data set was utilised to assess the trained model. This procedure was similar to leave-one-out spatial-temporal cross-validation, which allowed to evaluate model robustness for spatio-temporal variations. Except for one model (M12), all other five models showed stable model performances in every evaluating metric, namely overall accuracy, kappa statistics, true-positive rate, and false-negative rate.

In Chapter 5, UAV-borne thermal camera images were utilised in addition to RGB images. Thermal images are usually employed to retrieve evapotranspiration and water stress in vegetation (Berni et al., 2009; Brenner et al., 2018; Sagan et al., 2019). According to our knowledge, UAV-borne thermal images have been investigated for species mapping for the first time in Chapter 5. In thermal images, low temperature indicated lupin plant regions compared to the surrounding non-lupine vegetation regions being indicated by higher temperatures. Higher water content in lupine compared to other grassland species (Hensgen and Wachendorf, 2016) and a shading effect due to the bushy lupine structure were the possible reasons, therefore. Although thermal images showed a distinct difference between lupine and non-lupine vegetation, the thermal attributes did not turn out to be considerable predictors in the classification models. An error resulting from a shift between thermal and RGB images due to different spatial resolutions (2 cm for thermal images and 1 cm for RGB images) as well as variations in geo-reference accuracy might be the possible reasons for that.

The lupine coverage maps generated from image classification showed a similar map and area accuracy to the maps made from image digitising. Cock and Wittenberg (2001) explained that the early detection of regions with low coverage of invasive species is critical to control those species. Therefore, the ecologist must identify regions sparsely invaded by lupine to start immediate eradication actions. Parallel to that, the generated lupine coverage maps showed higher map accuracy when the relative lupine area was lower. As discussed here, the developed novel workflow to map invasive lupine in grassland using UAV-borne images showed robust performance, and it indicated that positive attainment of the third sub-objective.

6.2 Potential applications

In the last few decades, the agricultural industry changed to deliver site-specific management responding to field variability with technological development leading to a

system called precision agriculture (PA) (Cox, 2002). It facilitated utilising available resources more efficiently by the precise identification of a requirement, possibly increasing yields while reducing cost. According to Cox (2002), global navigational satellite systems (GNSS) and RS are the crucial tools that are applied in PA, enabling non-destructive measurements of agricultural vegetation at an exact location. The availability of UAVs as the RS platform has been widely utilised in PA. Salamí et al. (2014) reported that more than 60 % of UAV-borne RS data researches focused on PA.

UAV-borne RS has been widely employed for PA in arable crops such as maize, wheat, cotton, rice, soya and vineyards (Tsouros et al., 2019). However, PA in grasslands was not much investigated using UAV-borne RS, though a review by Schellberg et al. (2008) mentioned that UAV-borne RS could be a potential technique for PA in grasslands. Therefore, the findings of this study can shed light on the application of UAV-borne RS for PA in grasslands. This study could help to answer three main questions related to UAV-borne RS for PA in grasslands.

Which grassland traits can be accurately measured using UAV-borne RS?
This study demonstrated that both structural (sward height, fresh and dry biomass) and biochemical (forage nutritional values) grassland traits could be successfully estimated using UAV-borne RS data. Further, maps visualising those traits can be generated using UAV-borne image, which is useful for PA in grasslands. Measuring sward height enables to monitor the growth of grass halms that is essential to identify the regions where different growth pattern occurs as well as underlying mechanisms for growth pattern (i.e. species composition, fertiliser application, water availability) and growth rate (Schellberg et al., 2008). Similar to the sward height, knowledge about available biomass from grassland is necessary for PA to manage feedstocks for ruminants (Wachendorf et al., 2017). Accurate estimation of both CP and ADF values of grass forage was reported in Chapter 4. Besides stated quality parameters, UAV-borne RS showed the potential to estimate other forage quality parameters such as crude ash, metabolic energy, and minerals (e.g. Na, K) in experimental grassland setup (Capolupo et al., 2015). Maps with forage nutritional values can facilitate to farmers; i) to schedule mowing and grazing activities, and ii) to harvest and ensile similar quality biomass together to meet requirements of distinct animal species and performance categories. However, forage nutritional values are closely related to stages of growth (young or matured), species composition (e.g. legume percentage) (Frame and Laidlaw, 2011), which might be determined by combined data retrieved from biomass and sward height.

Which sensor or camera is suitable to measure those traits?

Miniaturising of sensors facilitated to build light-weight sensors which could be payloads for the UAV. An RGB camera (visible light camera), imaging spectroscopy (hyperspectral camera), and a thermal camera were employed in this study. The RGB camera provided very high-resolution true colour images. RGB cameras are relatively low cost and easy to operate compared to other sensors but do not provide valuable non-visible spectral data that are crucial for the estimation of vegetation properties. However, through processing with SFM, they can deliver 3D point clouds that could be useful to derive vegetation CHM. Further, vegetation indices based on RGB values could also provide potential data related to vegetation. In Chapter 3, CHM derived from the UAV-borne RGB camera was successfully employed to obtain grassland sward height and estimate grassland biomass. An Imaging spectroscopy sensor onboard the UAV provides hyperspectral 2D images where each pixel contains near-continuous spectral reflectance data. The sensor employed was a relatively expensive and complicated sensor. The hyperspectral camera delivered 20 cm image while the RGB camera delivered 1 cm spatial resolution images at 20 m flying height. The near-continuous spectral reflectance data are useful to estimate forage nutritional values as well as grassland biomass (Capolupo et al., 2015; Näsi et al., 2018). A UAV-borne thermal camera captures images that represent emitted thermal infrared data from vegetation (Berni et al., 2009). In Chapter 5, thermal images were utilised to discriminate lupine and non-lupine vegetation based on plant water content. Following the same concept, thermal cameras can be employed for PA in grassland as a sensor to monitor water stress in grassland vegetation and soil water content as well as evapotranspiration of grassland (Brenner et al., 2018).

In addition to the sensors employed in this study, it is worth to mention that multispectral cameras and light-weight LiDAR sensors were reported in few studies as UAV payloads for grassland trait estimation (Wang et al., 2017; Grüner et al., 2020). Multispectral sensors have wide spectral bands in selected regions of the electromagnetic spectrum such as green, red, red-edge, and near-infrared. Additionally, multispectral sensors are less expensive than hyperspectral sensors. Data from multispectral cameras mostly used to calculate popular vegetation indices, namely NDVI, EVI, and SAVI, which can be utilised as a proxy for estimating grassland biomass and nitrogen content (Grüner et al., 2020). UAV-borne LiDAR sensors are a trend recently developed trend in UAV-borne RS, which can also be applied to estimate sward height and grassland biomass (Wang et al., 2017).

Which statistical methods are appropriate for modelling grassland traits?
To develop a model that can estimate grassland traits, various statistical methods have been employed. In this study, both simple linear models, as well as complex ML mod-

els, were applied. Simple linear models are easy to understand and interpret, although they do not allow the use of multicollinearity data. As RS data can provide many multicollinearity explanatory variables, the optimal variables must be selected to be used in simple linear regression models. In Chapter 3, the Pearson correlation coefficient was employed to identify the optimal variables. On the contrary, the multicollinearity data can be applied to the ML models though those are complex to understand and explain (Garg and Tai, 2013). ML regression and classification models were utilised in Chapter 4 and 5 to materialise the advantages of all available explanatory variables. Capolupo et al. (2015) also proved that PLSR models performed better than linear models. Besides the statistical algorithm, models are biased to an underlying data set that has been employed to train the model, so it is challenging to develop a generalised statistical model that can be utilised for all grasslands. In Chapter 3, when the level of the heterogeneity (i.e. species, management) was increased, the performance of the linear models decreased. However, ML models in Chapter 4 and Chapter 5 showed that they can address those complex variation up to some level in the data set and can deliver comprehensive models. Nevertheless, for successful utilisation of UAV-borne RS for PA in grassland, the models had to be trained at least one time with the data from every grassland sampled to increase the precision of the model.

In the previous paragraphs, the discussion was focused on the question, "how the findings of this study support for PA utilisation in grasslands". Apart from PA, Wachendorf et al. (2017) reported the maps representing grassland traits produced from RS could be used for three different levels (i.e. strategic level, tactical level, and operational level) of decision making in grassland farm management which in the future might be suited to provide cheap, accurate, timely information to farmers. The application of UAV-borne RS could directly involve the operational level where farmers could use the information derived to influence day to day decisions such as pasture rotation and fertiliser input. When it comes to the strategic level, an aggregation of a time series of UAV-borne RS data could assist. However, the usage of models with UAV-borne RS data alone is not enough to provide suitable information to farmers. Dry conditions in summer of 2018 caused a different situation than usual and models in Chapter 4 could not explain some variations due to that effect. Therefore, data related to weather is also necessary as an input in addition to RS data models to address changes in weather. This could be one focus for future research in the UAV-borne RS.

Besides forage production from grassland, UAV-borne RS could be used for monitoring biodiversity and measures for climate change in grasslands. Biodiversity is an essential component of semi-natural grassland (Gibson, 2009). When semi-natural grasslands are contested by invasive plant species, the species richness of grasslands could decline

(Courchamp et al., 2017). The described workflow in Chapter 5 helped to map invasive lupine coverage which can be utilised as an indicator for species diversity. Those maps with invasive species coverage could be employed for the grassland restoration process, which was considered as one of the main grassland research activities in the 21st century (Wilsey, 2018). Additionally, airborne hyperspectral data showed the potential for estimation of alpha and beta diversity (Möckel, 2015), and it might be implemented using UAV-borne imaging spectroscopy data. This would be another direction to future research. Overall, monitoring biodiversity indicators in grasslands using UAV-borne RS data would also be beneficial to achieve the United Nations sustainable development goal 15 (SDG 15: Life On Land) (Spröte, 2010; United Nations, 2020)

Grassland can sequestrate carbon which can help to mitigate climate change, but emissions of methane and nitrous oxide from ruminants (often fed with grassland-based forage) increase the effect of climate change (Frame and Laidlaw, 2011). Emission of those greenhouse gasses can be reduced by proper management of grasslands and livestock (FAO, 2009). The data obtained from UAV-borne RS can assist in conducting proper management of grasslands, as discussed under the PA section. The maps indicating available biomass and quality information can improve the effective use of grazing management. Forage with controlled CP content, for instance, will help to reduce the emissions of nitrous oxide from ruminants (Frame and Laidlaw, 2011). Furthermore, UAV-borne RS application may be a suitable method for the non-destructive sampling of experimental works which explore grassland condition due to climate change.

6.3 Limitations and ways forward

The fourth sub-objective of the study was to understand the limitations as well as measures to improve fine-scale grassland monitoring using UAV-borne RS. Subsequent discussion section reviews identified problems and possible solutions derived from this study. However, most of the identified problems are not limited to grassland monitoring, and they are familiar to general UAV-borne RS in agriculture.

One of the significant concerns of UAV-borne RS is a limitation in the data collection area. According to experience gained from fieldwork in this study, it was observed that 0.5 hectare was the maximum area (within 15 minutes) which could be covered in one flight session at 20 m flying height using a quadcopter or an octocopter. Fixed-wing UAVs can fly with more extended flight sessions, but there are limitations in their flying characteristics (not possible to hoover in the air, higher-flying speed) (Bendig,

2015). Increment of flying height can provide more excellent area coverage, but it will lead to a decrease in spatial resolution (Shi et al., 2016). Hence, in UAV-borne RS, there is always a trade-off between the area to be covered and details to be inspected due to limited battery capacity in UAVs. However, about 65 % of farm fields in Europe are less than five hectares (Eurostat, 2016), and a few flight sessions using extra batteries can cover one field easily. On the other hand, UAV technology is still evolving, and future technological development could deliver a single battery with a longer cycle. However, the UAV flights with most commercial available platforms cannot be conducted on rainy or very windy days. Additionally, a special permission is needed before being allowed to fly in specific areas (e.g. conservation areas, urban areas, close to air-traffic control regions) as required according to legislation and rules of the country (Tsouros et al., 2019).

The requirement of skilled human resources and physical resources for UAV-borne RS data collection and image processing are additional challenges in UAV-borne RS. During the last few years, the availability of a simple and inexpensive UAV system has increased, and they are easily customisable to existing sensors. In Chapter 5, the thermal camera was attached to the commercial UAV system using a 3D printed gimbal. Additionally, those simple UAVs are easy to deploy, and an auto-pilot system of the UAV allows to do systematic data collection, which can be repeated in the same way. When it comes to processing UAV-borne images, commercial software such as Agisoft PhotoScan, Pix4D dominates (Gross, 2015). This commercial software is relatively expensive, and algorithms used to process images are not disclosed to the users. However, they are easy to use and provide excellent results, as well as they are popular among the UAV-borne RS community. Nevertheless, open-source software is available, and they are being developed to compete against commercial software (Open Drone Map, 2019).

In addition to the software, the computational capacity (memory and processing power) of the computer should be high to process large raster files from UAV-borne RS. This study employed a computer with 128 GB memory and 3.6 GHz processor. Moreover, some sensors also offer cloud-based processing options, where collected images are uploaded to the cloud and processed. Afterwards, output ortho-mosaics can be downloaded; (e.g. MicaSense Inc (2019) Atlas). After obtaining an ortho-mosaic, fundamental RS and statistical skills are required to generate models and maps. Due to the explained necessity of knowledge, skills and resources, farmers are not able to become the direct users of UAVs to manage their grassland fields. However, universities, agricultural organisations or private companies can act as the service providers (collect and process images, build models and disseminate grassland trait maps) to farmers through the internet or another possible method. Additionally, future research should

focus on automating the whole work chain, and identification of effective mechanism to distribute information to farmers.

As mentioned in the previous sections (6.1 and 6.2), a generalised prediction model that is suitable for any grassland type is challenging to develop. Data representing all possible grassland varieties should be included to obtain an accurate generalised model, but this is a practically tough task. However, a combination of ML and hyperspectral data from UAV showed some potential to develop comprehensive models for grasslands in the north Hessen region in Germany in Chapter 4. Further, the fusion of different UAV-borne RS data (e.g. CHM and spectral) could be a way forward for achieving a generalised model. Möckel et al. (2017) reported that the combined usage of ground-borne hyperspectral data and ultra-sonic height measurements had improved biomass estimation in different pastures.

UAV-borne data collection of this study was conducted one day before the farmer's mowing date in each field to simulate the actual conditions. However, time-series data related to the full growing period was missing in this study. That data is vital for PA in grasslands, for example, i) to identify growth patterns of grass swards in spring and after mowing or grazing, ii) to outline the point in time of high nutritional or high productive grass biomass for the animals. Grüner et al. (2019) demonstrated grass biomass modelling using data from the whole growing season in experimental field conditions, but they recommended future studies towards this direction. Confirming the same, future research focusing on UAV-borne RS to describe grass sward growth patterns and temporal grassland traits should be conducted.

To sum up, this study comprehensively examined the applicability of UAV-borne RS for fine-scale grassland monitoring under real field conditions. Based on the findings from this study, it can be stated that grassland biomass, forage quality as well as invasive species mapping in grassland can be successfully conducted using UAV-borne RS. Further development of the described methods can be obtained using the suggested improvements to the identified limitations.

6.4 Conclusions

This study was conducted to fill the research gaps of UAV-borne RS for fine-scale grassland monitoring under real field conditions. Overall, this study demonstrated that UAV-borne RS is a potential and promising tool for fine-scale grassland monitoring with the aspect of grassland biomass, forage quality estimation and invasive species mapping in grassland. According to the findings from this study, the following con-

clusions can be drawn based on the specific study aims.

i The 3D point cloud derived from UAV-borne RGB images showed that it could be utilised to extract grassland CHM (Chapter 3). The obtained sward height from CHM employed as a proxy to estimate grassland biomass (both fresh and dry) successfully from different grasslands. However, model performances decreased when the grassland species richness and canopy heterogeneity increased.

ii The spectral reflectance obtained from UAV-borne imaging spectroscopy data and ML algorithms revealed that generalised forage quality estimation models could be developed (Chapter 4). Consequently, those comprehensive models proved that they could accurately estimate important two forage quality values (CP and ADF) irrespective of grassland type. Further, based on the model estimations spatio-temporal maps indicating forage nutritional values were generated, and they assist the practical grassland agriculture.

iii The combination of UAV-borne RS images and OBIA directed to build an effective workflow to map invasive lupine in grasslands (Chapter 5). The lupine coverage maps generated from developed workflow obtained small discrepancy than the standard digitised maps. The classification models indicated that they were robust in both spatial and temporal variations in grasslands. Hence, the models can be directly transferred to other lupine invaded grassland regions. Additionally, data derived from UAV-borne RGB images (hue, CHM, SSI) were essential variables in the classification model. However, thermal and texture attributes did not become crucial for classifying lupine and non-lupine vegetation.

iv Relatively small area coverage, the requirement of human and technical resources, and developing generalised models that are compatible with any grassland type are the identified limitations for UAV-borne RS for fine-scale grassland monitoring under real field conditions. Simultaneously, procedures to improve those limitations were recognised and discussed, which would be helpful to apply these study findings to practical grassland applications.

Bibliography

Aasen, H., Burkart, A., Bolten, A., & Bareth, G. (2015). Generating 3D hyperspectral information with lightweight UAV snapshot cameras for vegetation monitoring: from camera calibration to quality assurance. *ISPRS Journal of Photogrammetry and Remote Sensing*, *108*, 245–259. doi:10.1016/j.isprsjprs.2015.08.002

Abeysinghe, T., Milas, A. S., Arend, K., Hohman, B., Reil, P., Gregory, A., & Vázquez-Ortega, A. (2019). Mapping invasive Phragmites australis in the Old Woman Creek estuary using UAV remote sensing and machine learning classifiers. *Remote Sensing*, *11*(11), 23. doi:10.3390/rs11111380

AgiSoft LLC. (2018). AgiSoft PhotoScan Professional. Retrieved from https://www.agisoft.com/downloads/installer/

Ali, I., Cawkwell, F., Dwyer, E., Barrett, B., & Green, S. (2016). Satellite remote sensing of grasslands: from observation to management. *Journal of Plant Ecology*, *9*(6), 649–671. doi:10.1093/jpe/rtw005

Bareth, G., Bolten, A., Hollenberg, J., Aasen, H., Burkart, A., & Schellberg, J. (2015). Feasibility study of using non-calibrated UAV-based RGB imagery for grassland monitoring: case study at the Rengen Long-term Grassland Experiment (RGE), Germany. *DGPF Tagungsband 24*, 55–62.

Belgiu, M., & Drăgu, L. (2016). Random forest in remote sensing: A review of applications and future directions. *ISPRS Journal of Photogrammetry and Remote Sensing*, *114*, 24–31. doi:10.1016/j.isprsjprs.2016.01.011

Belgiu, M., Drăguţ, L., & Strobl, J. (2014). Quantitative evaluation of variations in rule-based classifications of land cover in urban neighbourhoods using WorldView-2 imagery. *ISPRS Journal of Photogrammetry and Remote Sensing*, *87*, 205–215. doi:10.1016/j.isprsjprs.2013.11.007

Bendig, J. (2015). *Unmanned aerial vehicles (UAVs) for multi-temporal crop surface modelling-A new method for plant height and biomass estimation based on RGB-imaging* (Doctoral

dissertation). Retrieved from http://kups.ub.uni-koeln.de/6018/1/Bendig%7B%5C_%7DPhD%7B%5C_%7D2014%7B%5C_%7DOrt%7B%5C&%7DDatum%7B%5C_%7Dfinal%7B%5C_%7DnoCV.pdf

Bendig, J., Bolten, A., Bennertz, S., Broscheit, J., Eichfuss, S., & Bareth, G. (2014). Estimating biomass of barley using crop surface models (CSMs) derived from UAV-based RGB imaging. *Remote Sensing*, *6*(11), 10395–10412. doi:10.3390/rs61110395

Bendig, J., Willkomm, M., Tilly, N., Gnyp, L., Bennertz, S., Qiang, C., ... Bareth, G. (2013). Very high resolution crop surface models (CSMs) from UAV-based stereo images for rice growth monitoring In Northeast China. *International Archives of the Photogrammetry, Remote Sensing and Spatial Information Sciences*, *40*(September), 4–6. doi:10.5194/isprsarchives-XL-1-W2-45-2013

Berni, J. A., Zarco-Tejada, P. J., Suárez, L., & Fereres, E. (2009). Thermal and narrowband multispectral remote sensing for vegetation monitoring from an unmanned aerial vehicle. *IEEE Transactions on Geoscience and Remote Sensing*, *47*(3), 722–738. doi:10.1109/TGRS.2008.2010457

Bhatta, B. (2013). *Research Methods in Remote Sensing*. London, UK: Springer.

Biewer, S., Fricke, T., & Wachendorf, M. (2009a). Determination of dry matter yield from legume-grass swards by field spectroscopy. *Crop Science*, *49*(5), 1927–1936. doi:10.2135/cropsci2008.10.0608

Biewer, S., Fricke, T., & Wachendorf, M. (2009b). Development of canopy reflectance models to predict forage quality of legume-grass mixtures. *Crop Science*, *49*(5), 1917–1926. doi:10.2135/cropsci2008.11.0653

Biosphärenreservat Rhön. (2019). Biosphärenreservat Rhön. Retrieved October 8, 2019, from https://biosphaerenreservat-rhoen.de/

Bischl, B., Lang, M., Kotthoff, L., Schiffner, J., Richter, J., Studerus, E., ... Jones, Z. M. (2016). Mlr: Machine learning in R. *Journal of Machine Learning Research*, *17*, 1–5.

Blaschke, T. (2010). Object based image analysis for remote sensing. *ISPRS Journal of Photogrammetry and Remote Sensing*, *65*(1), 2–16. doi:10.1016/j.isprsjprs.2009.06.004

Blaschke, T., Hay, G. J., Kelly, M., Lang, S., Hofmann, P., Addink, E., ... Tiede, D. (2014). Geographic Object-Based Image Analysis - Towards a new paradigm. *ISPRS Journal of Photogrammetry and Remote Sensing*, *87*, 180–191. doi:10.1016/j.isprsjprs.2013.09.014

Borre, J., Paelinckx, D., Mücher, C. A., Kooistra, L., Haest, B., Blust, G. D., & Schmidt, A. (2011). Integrating remote sensing in Natura 2000 habitat monitoring: prospects on the way forward. *Journal for Nature Conservation*, *19*(2), 116–125.

Breiman, L. (2001). Random forests. *Machine learning*, *45*, 5–32.

Brenner, C., Zeeman, M., Bernhardt, M., & Schulz, K. (2018). Estimation of evapotranspiration of temperate grassland based on high-resolution thermal and visible range imagery from unmanned aerial systems. *International Journal of Remote Sensing*, *39*(15-16), 5141–5174. doi:10.1080/01431161.2018.1471550

Brenning, A. (2012). Spatial cross-validation and bootstrap for the assessment of prediction rules in remote sensing: The R package sperrorest. *International Geoscience and Remote Sensing Symposium (IGARSS)*, 5372–5375. doi:10.1109/IGARSS.2012.6352393

Capolupo, A., Kooistra, L., Berendonk, C., Boccia, L., & Suomalainen, J. (2015). Estimating plant traits of grasslands from UAV-acquired hyperspectral images: a comparison of statistical approaches. *ISPRS International Journal of Geo-Information*, *4*(4), 2792–2820. doi:10.3390/ijgi4042792

Castro, P. A., & Garbulsky, M. F. (2018). Spectral normalized indices related with forage quality in temperate grasses : scaling up from leaves to canopies. *International Journal of Remote Sensing*, *39*(10), 3138–3163. doi:10.1080/01431161.2018.1430394

Catchpole, W. R., & Wheelert, C. J. (1992). Review estimating plant biomass : a review of techniques. *Australian Journal of Ecology*, *17*, 121–131. doi:10.1111/j.1442-9993.1992.tb00790.x

Chabot, D., Dillon, C., Shemrock, A., Weissflog, N., & Sager, E. P. (2018). An object-based image analysis workflow for monitoring shallow-water aquatic vegetation in multispectral drone imagery. *ISPRS International Journal of Geo-Information*, *7*(8). doi:10.3390/ijgi7080294

Chen, Y., Su, W., Li, J., & Sun, Z. (2009). Hierarchical object oriented classification using very high resolution imagery and LIDAR data over urban areas. *Advances in Space Research*, *43*(7), 1101–1110. doi:10.1016/j.asr.2008.11.008

Clark, R. N., & Roush, T. L. (1984). Reflectance spectroscopy: quantitative analysis techniques for remote sensing applications. *Journal of Geophysical Research: Solid Earth*, *89*(B7), 6329–6340. doi:10.1029/JB089iB07p06329

Cock, M. J. W., & Wittenberg, R. (2001). Early detection. In M. J. W. Cock & R. Wittenberg (Eds.), *Invasive alien species: A toolkit of best prevention and management practices* (Chap. Chapter 4, pp. 101–123). doi:10.1079/9780851995694.0000

Cooper, S. D., Roy, D. P., Schaaf, C. B., & Paynter, I. (2017). Examination of the potential of terrestrial laser scanning and structure-from-motion photogrammetry for rapid nondestructive field measurement of grass biomass. *Remote Sensing*, *9*(6). doi:10.3390/rs9060531

Courchamp, F., Fournier, A., Bellard, C., Bertelsmeier, C., Bonnaud, E., Jeschke, J. M., & Russell, J. C. (2017). Invasion biology: Specific problems and possible solutions. *Trends in Ecology and Evolution*, *32*(1), 13–22. doi:10.1016/j.tree.2016.11.001

Cox, S. (2002). Information technology: The global key to precision agriculture and sustainability. *Computers and Electronics in Agriculture*, *36*(2-3), 93–111. doi:10.1016/S0168-1699(02)00095-9

Cubert GmbH. (2016). *Cubert S185*. Cubert GmbH. Ulm. Retrieved from https://cubert-gmbh.com/product/uhd-185-firefly/

Cubert GmbH, & Copter Squad. (2018). *RTK-X8 Hyperspectral mapping*. Cubert GmbH; Copter Squad. Ulm. Retrieved from https://cubert-gmbh.com/product/rtk-x8-hyperspectral-mapping/

Cunliffe, A. M., Brazier, R. E., & Anderson, K. (2016). Ultra-fine grain landscape-scale quantification of dryland vegetation structure with drone-acquired structure-from-motion photogrammetry. *Remote Sensing of Environment*, *183*, 129–143. doi:10.1016/j.rse.2016.05.019

Curran, P. J. (1989). Remote sensing of foliar chemistry. *Remote Sensing of Environment*, *30*(3), 271–278. doi:10.1016/0034-4257(89)90069-2

Dandois, J. P., & Ellis, E. C. (2013). High spatial resolution three-dimensional mapping of vegetation spectral dynamics using computer vision. *Remote Sensing of Environment*, *136*, 259–276. doi:10.1016/j.rse.2013.04.005

Dawson, T. P., & Curran, P. J. (1998). Technical note A new technique for interpolating the reflectance red edge position. *International Journal of Remote Sensing*, *19*(11), 2133–2139. doi:10.1080/014311698214910

de Sá, N. C., Castro, P., Carvalho, S., Marchante, E., López-Núñez, F. A., & Marchante, H. (2018). Mapping the flowering of an invasive plant using unmanned aerial vehicles: Is there potential for biocontrol monitoring? *Frontiers in Plant Science*, *9*(March), 1–13. doi:10.3389/fpls.2018.00293

Drucker, H., Burges, C. J. C., Kaufman, L., Smola, A., & Vapnik, V. (2003). Support vector regression machines. *Fuzzy Sets and Systems*, *138*(2), 271–281. doi:10.1016/S0165-0114(02)00514-6

Dunnington, D., & Harvey, P. (2019). *exifr: EXIF Image Data in R*. Retrieved from https://cran.r-project.org/package=exifr

Durante, M., Oesterheld, M., Piñeiro, G., & Vassallo, M. M. (2014). Estimating forage quantity and quality under different stress and senescent biomass conditions via spectral reflectance. *International Journal of Remote Sensing*, *35*(9), 2963–2981. doi:10.1080/01431161.2014.894658

Eitel, J. U. H., Magney, T. S., Vierling, L. A., Brown, T. T., & Huggins, D. R. (2014). LiDAR based biomass and crop nitrogen estimates for rapid, non-destructive assessment of wheat nitrogen status. *Field Crops Research*, *159*, 21–32. doi:10.1016/j.fcr.2014.01.008

Espindola, G. M., Camara, G., Reis, I. A., Bins, L. S., & Monteiro, A. M. (2006). Parameter selection for region-growing image segmentation algorithms using spatial autocorrelation. *International Journal of Remote Sensing*, *27*(14), 3035–3040. doi:10.1080/01431160600617194

European Environment Agency. (2018). High Resolution Layer: Grassland (GRA) 2015. Retrieved January 9, 2020, from https://land.copernicus.eu/pan-european/high-resolution-layers/grassland/status-maps/2015?tab=mapview

Eurostat. (2016). Distribution of EU farms and utilised agricultural area according to farm size, 2016 (%). Retrieved December 28, 2019, from https://ec.europa.eu/eurostat/statistics-explained/index.php/Farms_and_farmland_in_the_European_Union_-_statistics

FAO. (2009). *Grasslands: Enabling their potential to contribute to greenhouse gas mitigation*. FAO.

FLIR. (2016). *FLIR Vue Pro and Vue Pro R User Guide*. FLIR.

Frame, J., & Laidlaw, A. (2011). Feeding value of grass. In J. Frame & A. Laidlaw (Eds.), *Improved grassland management* (Chap. 14, pp. 167–180). Wiltshire: Corwood Press.

Fremstad, E. (2010). NOBANIS - Invasive alien species fact sheet. Retrieved October 7, 2019, from http://www.nobanis.org/

Fricke, T., Richter, F., & Wachendorf, M. (2011). Assessment of forage mass from grassland swards by height measurement using an ultrasonic sensor. *Computers and Electronics in Agriculture*, *79*(2), 142–152. doi:10.1016/j.compag.2011.09.005

Fricke, T., & Wachendorf, M. (2013). Combining ultrasonic sward height and spectral signatures to assess the biomass of legume-grass swards. *Computers and Electronics in Agriculture*, *99*, 236–247. doi:10.1016/j.compag.2013.10.004

Garg, A., & Tai, K. (2013). Comparison of statistical and machine learning methods in modelling of data with multicollinearity. *International Journal of Modelling, Identification and Control*, *18*(4), 295–312. doi:10.1504/IJMIC.2013.053535

Geladi, P., & Kowalski, B. R. (1986). Partial least-squares regression: a tutorial. *Analytica Chimica Acta*, *185*(100), 1–17. doi:10.1016/0003-2670(86)80028-9. arXiv: arXiv:1011.1669v3

Georganos, S., Grippa, T., Lennert, M., Vanhuysse, S., Johnson, B. A., & Wolff, E. (2018). Scale matters: Spatially partitioned unsupervised segmentation parameter optimization for large and heterogeneous satellite images. *Remote Sensing*, *10*(9). doi:10.3390/rs10091440

Gibson, D. (2009). *Grasses and grassland ecology* (1st ed.). Oxford University Press.

Glenn, N. F., Olsoy, P. J., Mitchell, J. J., & Shrestha, R. (2015). Aboveground biomass estimates of sagebrush using terrestrial and airborne LiDAR data in a dryland ecosystem. *Agricultural and Forest Meteorology*, *213*, 138–147. doi:10.1016/j.agrformet.2015.06.005

Goetz, A. F. H., Vane, G., Solomon, J. E., & Rock, B. N. (1985). Imaging spectrometry for earth remote sensing. *Science*, *228*(4704), 1147–1153. doi:10.1126/science.228.4704.1147

Gonzalez, R. C., & Woods, R. E. (2008). Color image processing. In R. C. Gonzalez & R. E. Woods (Eds.), *Digital image processing* (Third Edit, Chap. 6, pp. 401–414). New Jersy: Pearson Education.

GRASS Development Team. (2017). *Geographic Resources Analysis Support System (GRASS GIS) Software, Version 7.2*. Open Source Geospatial Foundation. Retrieved from http://grass.osgeo.org

Greaves, H. E., Vierling, L. A., Eitel, J. U. H., Boelman, N. T., Magney, T. S., Prager, C. M., & Griffin, K. L. (2015). Estimating aboveground biomass and leaf area of low-stature Arctic shrubs with terrestrial LiDAR. *Remote Sensing of Environment*, *164*, 26–35. doi:10.1016/j.rse.2015.02.023

Grippa, T., Lennert, M., Beaumont, B., Vanhuysse, S., Stephenne, N., & Wolff, E. (2017). An open-source semi-automated processing chain for urban object-based classification. *Remote Sensing*, *9*(4). doi:10.3390/rs9040358

Gross, J. W. (2015). A comparison of orthomosaic software for use with ultra high resolution imagery of a wetland environment.

Grüner, E., Astor, T., & Wachendorf, M. (2019). Biomass prediction of heterogeneous temperate grasslands using an SfM approach based on UAV imaging. *Agronomy*, *9*(2), 54. doi:10.3390/agronomy9020054

Grüner, E., Astor, T., & Wachendorf, M. (2020). *The potential of UAV-borne spectral and textural information for predicting aboveground biomass and N fixation in legume-grass mixture*.

Hafeez, S., Wong, M., Ho, H., Nazeer, M., Nichol, J., Abbas, S., … Pun, L. (2019). Comparison of machine learning algorithms for retrieval of water quality indicators in case-II waters: a case study of Hong Kong. *Remote Sensing*, *11*(6), 617. doi:10.3390/rs11060617

Haralick, R. M. (1979). Statistical and structural approaches to texture. *Proceedings of the IEEE*, *67*(5), 786–804. doi:10.1109/PROC.1979.11328

Heather, R., & Nature, E. (1999). Grassland Monitoring. In A. Crofts & R. Jefferson (Eds.), *Lowland grassland management handbook* (2nd ed., Chap. Chapter 15, Vol. 2, *March*, 15:1–15:21). English Nature.

Hensgen, F., & Wachendorf, M. (2016). The effect of the invasive plant species lupinus polyphyllus Lindl. On energy recovery parameters of semi-natural grassland biomass. *Sustainability (Switzerland)*, *8*(10). doi:10.3390/su8100998

Heritage, G., & Large, A. (2009). Principles of 3D laser scanning. In G. Heritage & A. Large (Eds.), *Laser scanning for the environmental sciences* (Chap. 2, pp. 21–34). doi:10.1002/9781444311952.ch2

Hesse, R. (2014). Three-dimensional vegetation structure of Tillandsia latifolia on a coppice dune. *Journal of Arid Environments*, *109*, 23–30. doi:10.1016/j.jaridenv.2014.05.001

Hijmans, R. J. (2019). *Raster: geographic data analysis and modelling*. Retrieved from https://cran.r-project.org/package=raster

Holman, F. H., Riche, A. B., Michalski, A., Castle, M., Wooster, M. J., & Hawkesford, M. J. (2016). High throughput field phenotyping of wheat plant height and growth

rate in field plot trials using UAV based remote sensing. *Remote Sensing*, *8*. doi:10.3390/rs8121031

Hönigová, I., Vačkář, D., Lorencová, E., Melichar, J., Götzl, M., Sonderegger, G., … Chobot, K. (2012). *Survey on grassland ecosystem services. Report to the EEA – European Topic Centre on Biological Diversity*. Nature Conservation Agency of the Czech Republic. Prague.

Hopkins, J. J. (1999). Grassland management decision making. In *Lowland grassland management handbook* (March, pp. 1–10).

Horrocks, R. D., & Vallentine, J. F. (1999). Forage quality - the basics. In R. D. Horrocks & J. F. Vallentine (Eds.), *Harvested forage* (Chap. 2, pp. 17–47). doi:10.1016/B978-0-12-356255-5.50024-9

Huyghe, C., De Vliegher, A., van Gils, B., & Peeters, A. (2014). *Grasslands and herbivore production in Europe and effects of common policies* (C. Huyghe, A. De Vliegher, B. van Gils, & A. Peeters, Eds.). doi:10.35690/978-2-7592-2157-8

Ishii, J., & Washitani, I. (2013). Early detection of the invasive alien plant Solidago altissima in moist tall grassland using hyperspectral imagery. *International Journal of Remote Sensing*, *34*(16), 5926–5936. doi:10.1080/01431161.2013.799790

Johnson, B., Bragais, M., Endo, I., Magcale-Macandog, D. B., & Macandog, P. B. M. (2015). Image segmentation parameter optimization considering within-and between-segment heterogeneity at multiple scale levels: Test case for mapping residential areas using Landsat imagery. *ISPRS International Journal of Geo-Information*, *4*(4), 2292–2305. doi:10.3390/ijgi4042292

Jones, D., Pike, S., Thomas, M., & Murphy, D. (2011). Object-based image analysis for detection of Japanese Knotweed s.l. taxa (polygonaceae) in Wales (UK). *Remote Sensing*, *3*(2), 319–342. doi:10.3390/rs3020319

Jones, H. G., & Vaughan, R. A. (2010). Integrated applications. In H. G. Jones & R. A. Vaughan (Eds.), *Remote sensing of vegetation - principles, techniques, and applications* (First Edit, Chap. Chapter 11, pp. 271–306). New York: Oxford University Press.

Kattenborn, T., Lopatin, J., Förster, M., Braun, A. C., & Fassnacht, F. E. (2019). UAV data as alternative to field sampling to map woody invasive species based on combined Sentinel-1 and Sentinel-2 data. *Remote Sensing of Environment*, *227*, 61–73. doi:https://doi.org/10.1016/j.rse.2019.03.025

Kawamura, K., Watanabe, N., Sakanoue, S., & Inoue, Y. (2008). Estimating forage biomass and quality in a mixed sown pasture based on partial least squares regression

with waveband selection. *Grassland Science*, *54*(3), 131–145. doi:10.1111/j.1744-697X.2008.00116.x

Keller, S., Maier, P. M., Riese, F. M., Norra, S., Holbach, A., Börsig, N., … Hinz, S. (2018). Hyperspectral data and machine learning for estimating CDOM, chlorophyll a, diatoms, green algae and turbidity. *International Journal of Environmental Research and Public Health*, *15*(9), 1–15. doi:10.3390/ijerph15091881

Klinger, Y. P., Harvolk-scho, S., Otte, A., & Ludewig, K. (2019). Applying landscape structure analysis to assess the spatio-temporal distribution of an invasive legume in the Rho UNESCO Biosphere Reserve. *21*, 2735–2749. doi:10.1007/s10530-019-02012-x

Knox, N. M., Skidmore, A. K., Prins, H. H., Asner, G. P., van der Werff, H. M., de Boer, W. F., … Grant, R. C. (2011). Dry season mapping of savanna forage quality, using the hyperspectral Carnegie Airborne Observatory sensor. *Remote Sensing of Environment*, *115*(6), 1478–1488. doi:10.1016/j.rse.2011.02.007

Kuhn, M., & Johnson, K. (2013). *Applied predictive modelling*. doi:10.1007/978-1-4614-6849-3

Kuhn, M., Wing, J., Weston, S., Williams, A., Keefer, C., Engelhardt, A., … Hunt, T. (2018). *Caret: Classification and regression training*. Retrieved from https://cran.r-project.org/package=caret

Kvalseth, T. O. (1985). Cautionary note about R2. *The American Statistician*, *39*(4), 279–285.

Laliberte, A. S., Rango, A., Havstad, K. M., Paris, J. F., Beck, R. F., McNeely, R., & Gonzalez, A. L. (2004). Object-oriented image analysis for mapping shrub encroachment from 1937 to 2003 in southern New Mexico. *Remote Sensing of Environment*, *93*(1-2), 198–210. doi:10.1016/j.rse.2004.07.011

Lambdon, P. W., Pyšek, P., Basnou, C., Hejda, M., Arianoutsou, M., Essl, F., … Hulme, P. E. (2008). Alien flora of Europe: Species diversity, temporal trends, geographical patterns and research needs. *Preslia*, *80*(2), 101–149.

Leclère, D., Valin, H., Frank, S., & Havlík, P. (2016). *Assessing the land use change effects of using EU grassland for biofuel production. Task 4b of tender ENER/C1/2013-412*. ECOFYS Netherlands B.V. Utrecht. Retrieved from https://ec.europa.eu/energy/sites/ener/files/documents/Annex%20I%20case%20study%201.pdf

Lehmann, J. R. K., Prinz, T., Ziller, S. R., Thiele, J., Heringer, G., Meira-Neto, J. A. A., & Buttschardt, T. K. (2017). Open-source processing and analysis of aerial im-

agery acquired with a low-cost Unmanned Aerial System to support invasive plant management. *Frontiers in Environmental Science*, *5*(JUL), 1–16. doi:10.3389/fenvs.2017.00044

Leica Geosystems. (2017). *Leica ScanStation P30 / P40*. Leica Geosystems.

Lennert, M., & GRASS Development Team. (2019). Addon i.segment.stats. Geographic resources analysis support system (GRASS) software, version 7.6. Retrieved October 18, 2019, from https://grass.osgeo.org/grass76/manuals/addons/i.segment.stats.html

Lesschen, J. P., Elbersen, B. S., Hazeu, G. W., van Doorn, A., Mucher, C. A., & Velthof, G. L. (2014). *Defining and classifying grasslands in Europe - Task 1*. Alterra, Wageningen UR. Wageningen.

Li, A., Dhakal, S., Glenn, N. F., Spaete, L. P., Shinneman, D. J., Pilliod, D. S., … McIlroy, S. K. (2017). Lidar aboveground vegetation biomass estimates in shrublands: prediction, uncertainties and application to coarser scales. *Remote Sensing*, *9*(9). doi:10.3390/rs9090903

Liaw, A., & Wiener, M. (2002). Classification and Regression by randomForest. *R Journal*, *2*(December), 18–22. doi:10.1177/154405910408300516

Lu, B., & He, Y. (2017). Species classification using Unmanned Aerial Vehicle (UAV)-acquired high spatial resolution imagery in a heterogeneous grassland. *ISPRS Journal of Photogrammetry and Remote Sensing*, *128*, 73–85. doi:10.1016/j.isprsjprs.2017.03.011

Lussem, U., Bolten, A., Menne, J., Gnyp, M. L., Schellberg, J., & Bareth, G. (2019). Estimating biomass in temperate grassland with high resolution canopy surface models from UAV-based RGB images and vegetation indices. *Journal of Applied Remote Sensing*, *13*(03), 1. doi:10.1117/1.jrs.13.034525

Ma, L., Li, M., Tong, L., Wang, Y., & Cheng, L. (2013). Using unmanned aerial vehicle for remote sensing application. In *2013 21st international conference on geoinformatics* (pp. 1–5). doi:10.1109/Geoinformatics.2013.6626078

Malambo, L., Popescu, S. C., Murray, S. C., Putman, E., Pugh, N. A., Horne, D. W., … Bishop, M. (2018). Multitemporal field-based plant height estimation using 3D point clouds generated from small unmanned aerial systems high-resolution imagery. *International Journal of Applied Earth Observation and Geoinformation*, *64*(June 2017), 31–42. doi:10.1016/j.jag.2017.08.014

Martin, F. M., Müllerová, J., Borgniet, L., Dommanget, F., Breton, V., & Evette, A. (2018). Using single- and multi-date UAV and satellite imagery to accurately monitor invasive knotweed species. *Remote Sensing*, *10*(10). doi:10.3390/rs10101662

McCune, B., & Grace, J. (2002). Measures of distance between samples :non-Euclidean. In *Analysis of ecological communities* (Chap. Chapter 5, pp. 33–44).

Meyer, H., Reudenbach, C., Wöllauer, S., & Nauss, T. (2019). Importance of spatial predictor variable selection in machine learning applications – Moving from data reproduction to spatial prediction. *Ecological Modelling*, *411*(March), 108815. doi:10.1016/j.ecolmodel.2019.108815. eprint: 1908.07805

MicaSense Inc. (2019). Atlas Cloud - Micasense. Retrieved December 28, 2019, from https://support.micasense.com/hc/en-us/categories/202581928-Atlas-Cloud

Michez, A., Piégay, H., Jonathan, L., Claessens, H., & Lejeune, P. (2016). Mapping of riparian invasive species with supervised classification of Unmanned Aerial System (UAS) imagery. *International Journal of Applied Earth Observations and Geoinformation*, *44*, 88–94. doi:10.1016/j.jag.2015.06.014

Milton, E. J. (1987). Principles of field spectroscopy. *International Journal of Remote Sensing*, *8*(12), 1807–1827. doi:10.1080/01431168708954818

Mirik, M., Chaudhuri, S., Surber, B., Ale, S., & James Ansley, R. (2013). Detection of two intermixed invasive woody species using color infrared aerial imagery and the support vector machine classifier. *Journal of Applied Remote Sensing*, *7*(1), 073588. doi:10.1117/1.jrs.7.073588

Möckel, T. (2015). *Hyperspectral and multispectral remote sensing for mapping grassland vegetation*. doi:10.13140/RG.2.1.2745.4564

Möckel, T., Dalmayne, J., Schmid, B. C., Prentice, H. C., & Hall, K. (2016). Airborne hyperspectral data predict fine-scale plant species diversity in grazed dry grasslands. *Remote Sensing*, *8*(2), 1–20. doi:10.3390/rs8020133

Möckel, T., Safari, H., Reddersen, B., Fricke, T., & Wachendorf, M. (2017). Fusion of ultrasonic and spectral sensor data for improving the estimation of biomass in grasslands with heterogeneous sward structure. *Remote Sensing*, *9*(1), 98. doi:10.3390/rs9010098

Morgenroth, J., & Gomez, C. (2014). Assessment of tree structure using a 3D image analysis technique—A proof of concept. *Urban Forestry & Urban Greening*, *13*(1), 198–203. doi:10.1016/j.ufug.2013.10.005

Müllerová, J., Brůna, J., Bartaloš, T., Dvořák, P., Vítková, M., & Pyšek, P. (2017). Timing is important: Unmanned aircraft vs. Satellite imagery in plant invasion monitoring. *Frontiers in Plant Science*, *8*(May), 1–13. doi:10.3389/fpls.2017.00887

Mutanga, O., & Skidmore, A. K. (2004). Integrating imaging spectroscopy and neural networks to map grass quality in the Kruger National Park, South Africa. *Remote Sensing of Environment*, *90*(1), 104–115. doi:10.1016/j.rse.2003.12.004

Mutanga, O., Skidmore, A. K., & Prins, H. H. (2004). Predicting in situ pasture quality in the Kruger National Park, South Africa, using continuum-removed absorption features. *Remote Sensing of Environment*, *89*(3), 393–408. doi:10.1016/j.rse.2003.11.001

Näsi, R., Viljanen, N., Kaivosoja, J., Alhonoja, K., Hakala, T., Markelin, L., & Honkavaara, E. (2018). Estimating biomass and nitrogen amount of barley and grass using UAV and aircraft based spectral and photogrammetric 3D features. *Remote Sensing*, *10*(7), 1–32. doi:10.3390/rs10071082

Numata, I. (2011). Characterization on pastures using field and imaging spectrometers. In T. Prasad S, L. John G, & H. Alfredo (Eds.), *Hyperspectral remote sensing of vegetation* (Chap. Chapter 9, pp. 207–225). Florida, USA: CRC Press.

Open Drone Map. (2019). Open Drone Map - Open Source Toolkit for processing Civilian Drone Imagery. Retrieved from https://www.opendronemap.org/

Otte, A., & Maul, P. (2005). Verbreitungsschwerpunkte und strukturelle Einnischung der Stauden-Lupine (Lupinus polyphyllus Lindl.) in Bergwiesen der Rhön. *Tuexenia*, *25*, 151–182.

Otto, S. A. (2019). How to normalize the RMSE. Retrieved May 30, 2019, from https://www.marinedatascience.co/blog/2019/01/07/normalizing-the-rmse/

Peeters, A. (2009). Importance, evolution, environmental impact and future challenges of grasslands and grassland-based systems in Europe. *Grassland Science*, *55*, 113–125. doi:10.1111/j.1744-697X.2009.00154.x

Petras, V., Petrasove, A., & Mitasova, H. (2018). Processing lidar and UAV point clouds in GRASS GIS. Retrieved May 6, 2018, from https://grasswiki.osgeo.org/wiki/Processing_lidar_and_UAV_point_clouds_in_GRASS_GIS_(workshop_at_FOSS4G_Boston_2017)

Phil Harvey. (2016). *ExifTool*. Kingston, Ontario, Canada. Retrieved from http://owl.phy.queensu.ca/%7B~%7Dphil/exiftool/

Possoch, M., Bieker, S., Hoffmeister, D., Bolten, A. A., Schellberg, J., & Bareth, G. (2016). Multi-Temporal crop surface models combined with the rgb vegetation index from UAV-based images for forage monitoring in grassland. *International Archives of the Photogrammetry, Remote Sensing and Spatial Information Sciences - ISPRS Archives*, *XLI-B1*, 991–998. doi:10.5194/isprsarchives-XLI-B1-991-2016

Probst, P., Wright, M. N., & Boulesteix, A. L. (2019). Hyperparameters and tuning strategies for random forest. *Wiley Interdisciplinary Reviews: Data Mining and Knowledge Discovery*, *9*(3), 1–19. doi:10.1002/widm.1301. arXiv: 1804.03515

Pullanagari, R., Kereszturi, G., & Yule, I. (2018). Integrating airborne hyperspectral, topographic, and soil data for estimating pasture quality using recursive feature elimination with random forest regression. *Remote Sensing*, *10*(7). doi:10.3390/rs10071117

Pullanagari, R., Yule, I. J., Tuohy, M. P., Hedley, M. J., Dynes, R. A., & King, W. M. (2012). In-field hyperspectral proximal sensing for estimating quality parameters of mixed pasture. *Precision Agriculture*, *13*(3), 351–369. doi:10.1007/s11119-011-9251-4

Pyšek, P., & Richardson, D. M. (2011). Invasive plants. *Ecological Engineering*, *2011*(26 September), 2011–2020.

Quinlan, J. R. (1992). Learning with continuous classes. In Adams & Sterling (Eds.), *Proceedings ai'92*, Singapore.

Quinlan, J. R. (1999). Simplifying decision trees. *International Journal of Human-Computer Studies*, *51*, 497–510.

Quinlan, J. (2006). Combining instance-based and model-based learning. In M. Kaufmann (Ed.), *Machine learning proceedings 1993* (Vol. 93, pp. 236–243). doi:10.1016/b978-1-55860-307-3.50037-x

R Core Team. (2019). *R: A Language and Environment for Statistical Computing*. R Foundation for Statistical Computing. Vienna, Austria. Retrieved from https://www.r-project.org/

Ramoelo, A., Skidmore, A. K., Cho, M. A., Mathieu, R., Heitkönig, I. M., Dudeni-Tlhone, N., … Prins, H. H. (2013a). Non-linear partial least square regression increases the estimation accuracy of grass nitrogen and phosphorus using in situ hyperspectral and environmental data. *ISPRS Journal of Photogrammetry and Remote Sensing*, *82*, 27–40. doi:10.1016/j.isprsjprs.2013.04.012

Ramoelo, A., Skidmore, A. K., Schlerf, M., Heitkönig, I. M., Mathieu, R., & Cho, M. A. (2013b). Savanna grass nitrogen to phosphorous ratio estimation using field spectroscopy and the potential for estimation with imaging spectroscopy. *International Journal of Applied Earth Observation and Geoinformation*, *23*(1), 334–343. doi:10.1016/j.jag.2012.10.008

Raschka, S. (2018). Model evaluation, model selection, and algorithm selection in machine learning. *Computing Research Repository*, *abs/1811.1*. arXiv: 1811.12808

Rasmussen, C. E., & Williams, C. K. I. (2006). *Gaussian processes for machine learning*. doi:10.1142/S0129065704001899. arXiv: 026218253X

Rocha, A. D., Groen, T. A., & Skidmore, A. K. (2019). Spatially-explicit modelling with support of hyperspectral data can improve prediction of plant traits. *Remote Sensing of Environment*, *231*(May), 111200. doi:10.1016/j.rse.2019.05.019

Royimani, L., Mutanga, O., Odindi, J., Dube, T., & Matongera, T. N. (2018). Advancements in satellite remote sensing for mapping and monitoring of alien invasive plant species (AIPs). *Physics and Chemistry of the Earth*, (December). doi:10.1016/j.pce.2018.12.004

Safari, H., Fricke, T., Reddersen, B., Möckel, T., & Wachendorf, M. (2016a). Comparing mobile and static assessment of biomass in heterogeneous grassland with a multisensor system. *Journal of Sensors and Sensor Systems*, *5*(2), 301–312. doi:10.5194/jsss-5-301-2016

Safari, H., Fricke, T., & Wachendorf, M. (2016b). Determination of fibre and protein content in heterogeneous pastures using field spectroscopy and ultrasonic sward height measurements. *Computers and Electronics in Agriculture*, *123*, 256–263. doi:10.1016/j.compag.2016.03.002

Sagan, V., Maimaitijiang, M., Sidike, P., Eblimit, K., Peterson, K. T., Hartling, S., … Mockler, T. (2019). UAV-based high resolution thermal imaging for vegetation monitoring, and plant phenotyping using ICI 8640 P, FLIR Vue Pro R 640, and thermomap cameras. *Remote Sensing*, *11*(3). doi:10.3390/rs11030330

Salamí, E., Barrado, C., & Pastor, E. (2014). UAV Flight Experiments Applied to the Remote Sensing of Vegetated Areas. *Remote Sensing*, *6*(11), 11051–11081. doi:10.3390/rs61111051

Santillan, R. A., Ocumpaugh, W. R., & Mott, G. O. (1979). Estimating forage yield with a disk meter. *Agronomy Journal*, *71*, 71–74. doi:10.2134/agronj1979.00021962007100010017x

Schellberg, J., Hill, M. J., Gerhards, R., Rothmund, M., & Braun, M. (2008). Precision agriculture on grassland: Applications, perspectives and constraints. *European Journal of Agronomy*, *29*(2-3), 59–71. doi:10.1016/j.eja.2008.05.005

Schirrmann, M., Giebel, A., Gleiniger, F., Pflanz, M., Lentschke, J., & Dammer, K. H. (2016). Monitoring agronomic parameters of winter wheat crops with low-cost UAV imagery. *Remote Sensing*, *8*(9). doi:10.3390/rs8090706

Schulze-Brüninghoff, D., Hensgen, F., Wachendorf, M., & Astor, T. (2019). Methods for LiDAR-based estimation of extensive grassland biomass. *Computers and Electronics in Agriculture*, *156*(December 2018), 693–699. doi:10.1016/j.compag.2018.11.041

Shi, Y., Thomasson, J. A., Murray, S. C., Pugh, N. A., Rooney, W. L., & Shafian, S. (2016). Unmanned aerial vehicles for high-throughput phenotyping and agronomic. *100*, 1–26. doi:10.5061/dryad.65m87

Silva, J. P., Toland, J., Jones, W., Elridge, J., Thorpe, E., & O'Hara, E. (2008). *LIFE and Europe´s grasslands: Restoring a forgotten habitat*. doi:10.2779/23028

Silver, M., Tiwari, A., & Karnieli, A. (2019). Identifying vegetation in arid regions using object-based image analysis with RGB-only aerial imagery. *Remote Sensing*, *11*(19), 1–26. doi:10.3390/rs11192308

Singh, L., Mutanga, O., Mafongoya, P., & Peerbhay, K. (2017). Remote sensing of key grassland nutrients using hyperspectral techniques in KwaZulu-Natal, South Africa. *Journal of Applied Remote Sensing*, *11*(3), 036005. doi:10.1117/1.JRS.11.036005

Skidmore, A. K., Ferwerda, J. G., Mutanga, O., Van Wieren, S. E., Peel, M., Grant, R. C., … Venus, V. (2010). Forage quality of savannas - simultaneously mapping foliar protein and polyphenols for trees and grass using hyperspectral imagery. *Remote Sensing of Environment*, *114*(1), 64–72. doi:10.1016/j.rse.2009.08.010

Skowronek, S., Stenzel, S., & Feilhauer, H. (2018). Detecting invasive species from above - How can we make use of remote sensing data to map invasive plant species in Germany? *Natur und Landschaft*, 434–438. doi:10.17433/9.2018.50153623.434-438

Smit, H. J., Metzger, M. J., & Ewert, F. (2008). Spatial distribution of grassland productivity and land use in Europe. *Agricultural Systems*, *98*(3), 208–219. doi:10.1016/j.agsy.2008.07.004

Smith, K., Wells, D., & Welsh, P. (1985). *Botanical Surveys and Monitoring Methods for Grasslands - Hand Book Number 1*. Peterborough, UK: Nature Conservancy Council.

Smola, A. J., & Scholkopf, B. (2004). A tutorial on support vector regression. *Statistics and Computing*, 199–222. doi:10.1023/B:STCO.0000035301.49549.88. arXiv: arXiv:1011.1669v3

Smola, A. (1996). *Regression estimation with support vector learning machines* (Master thesis, Technische Universität München). doi:10.1.1.10.3628

Snavely, N., Seitz, S., & Szeliski, R. (2006). Photo Tourism: Exploring Photo Collections in 3D. In *Siggraph conference proceedings* (pp. 835–846). doi:10.1145/1141911.1141964

Spröte, W. (2010). *ECOSOC – Economic And Social Council* (tech. rep. No. May). doi:10.1163/ej.9789004180048.i-962.115

Starks, P. J., Coleman, S. W., & Phillips, W. A. (2004). Determination of forage chemical composition using remote sensing. *Journal of Range Management*, *57*(6), 635–640.

Statistisches Bundesamt. (2018). Yield per hectare (field crops and grassland): Germany, years, types of crops. Retrieved May 17, 2018, from https://www-genesis.destatis.de/genesis/online/data;jsessionid=772A52BD2BEC1EE3F91F5A1389D498BD.tomcat%7B%5C_%7DGO%7B%5C_%7D2%7B%5C_%7D1?operation=abruftabelleAbrufen%7B%5C&%7Dselectionname=41241-0003%7B%5C&%7Dlevelindex=1%7B%5C&%7Dlevelid=1526569169115%7B%5C&%7Dindex=2

Sun, L., Wu, Z., Liu, J., Xiao, L., & Wei, Z. (2015). Supervised spectral-spatial hyperspectral image classification with weighted markov random fields. *IEEE Transactions on Geoscience and Remote Sensing*, *53*(3), 1490–1503. doi:10.1109/TGRS.2014.2344442

t'Mannetje, L., & Jones, R. (2000). *Field and Laboratory Methods for Grassland and Animal Production Research* (L. t Mannetje & R. Jones, Eds.). Oxon, UK: CABI Publishing.

Tilly, N., Hoffmeister, D., Cao, Q., Huang, S., Lenz-Wiedemann, V., Miao, Y., & Bareth, G. (2014a). Multitemporal crop surface models: accurate plant height measurement and biomass estimation with terrestrial laser scanning in paddy rice. *Journal of Applied Remote Sensing*, *8*(1), 083671. doi:10.1117/1.JRS.8.083671

Tilly, N., Hoffmeister, D., Schiedung, H., Hütt, C., Brands, J., & Bareth, G. (2014b). Terrestrial laser scanning for plant height measurement and biomass estimation of maize. In *International archives of the photogrammetry, remote sensing and spatial information sciences - isprs archives* (Vol. 40, *7*, pp. 181–187). doi:10.5194/isprsarchives-XL-7-181-2014

Tsouros, D. C., Bibi, S., & Sarigiannidis, P. G. (2019). A Review on UAV-Based Applications for Precision Agriculture. *Information*, *10*(11), 349. doi:10.3390/info10110349

Turner, D., Lucieer, A., & Parkes, S. (2017). Thermal Infrared remote sensing with a FLIR Vue Pro-R. In *Uas4rs 2017*, Tasmania.

United Nations. (2020). Sustainable development goal 15. Retrieved from https://sustainabledevelopment.un.org/sdg15

Viljanen, N., Honkavaara, E., Näsi, R., Hakala, T., Niemeläinen, O., & Kaivosoja, J. (2018). A novel machine learning method for estimating biomass of grass swards using a photogrammetric canopy height model, images and vegetation indices captured by a drone. *Agriculture*, *8*(5), 70. doi:10.3390/agriculture8050070

Wachendorf, M. (2018). Advances in remote sensing for monitoring grassland and forage production. In A. Marshal & R. Collins (Eds.), *Improving grassland and pasture management in temperate agriculture* (Chap. 14). Cambridge: Burleigh Dodds Science Publishing.

Wachendorf, M., Fricke, T., & Möckel, T. (2017). Remote sensing as a tool to assess botanical composition, structure, quantity and quality of temperate grasslands. *Grass and Forage Science*, (July 2017), 1–14. doi:10.1111/gfs.12312

Wallace, L., Hillman, S., Reinke, K., & Hally, B. (2017). Non-destructive estimation of above-ground surface and near-surface biomass using 3D terrestrial remote sensing techniques. *Methods in Ecology and Evolution*. doi:10.1111/2041-210X.12759

Wang, D., Xin, X., Shao, Q., Brolly, M., Zhu, Z., & Chen, J. (2017). Modeling aboveground biomass in Hulunber grassland ecosystem by using unmanned aerial vehicle discrete lidar. *17*(1), 1–19. doi:10.3390/s17010180

Weinmann, M. (2016). Preliminaries of 3D point cloud processing. In M. Weinmann (Ed.), *Reconstruction and analysis of 3d scenes from irregularly distributed 3d points to object classes* (Chap. Chapter 2, pp. 17–36). doi:10.1007/978-3-319-29246-5

Wijesingha, J. (2016). *Geometric quality assessment of UAV-borne remote sensing (RS) products for precision agriculture (PA)* (Master, Lund University).

Wijesingha, J., Moeckel, T., Hensgen, F., & Wachendorf, M. (2019). Evaluation of 3D point cloud-based models for the prediction of grassland biomass. *International Journal of Applied Earth Observation and Geoinformation*, *78*(June), 352–359. doi:10.1016/J.JAG.2018.10.006

Williams, C. K. I., & Rasmussen, C. E. (2008). Gaussian processes for regression. Retrieved from http://eprints.aston.ac.uk/651/

Williamson, S. C., Detling, J. K., Dodd, J. L., & Dyer, M. I. (1987). Nondestructive estimation of shortgrass aerial biomass. *Journal of Range Management*, *40*(3), 254–256. doi:10.2307/3899090

Wilsey, B. J. (2018). Conclusions, Future Research Needs, and Issues. In B. J. Wilsey (Ed.), *The biology of grasslands* (Chap. 9, p. 195). Oxford: Oxford University Press.

Xu, D., & Guo, X. (2015). Some insights on grassland health assessment based on remote sensing. *Sensors (Basel, Switzerland)*, *15*(2), 3070–3089. doi:10.3390/s150203070

Yang, G., Li, C., Wang, Y., Yuan, H., Feng, H., Xu, B., & Yang, X. (2017). The DOM generation and precise radiometric calibration of a UAV-mounted miniature snapshot hyperspectral imager. *Remote Sensing*, *9*(7), 642. doi:10.3390/rs9070642

Yuan, H., Yang, G., Li, C., Wang, Y., Liu, J., Yu, H., … Yang, X. (2017). Retrieving soybean leaf area index from unmanned aerial vehicle hyperspectral remote sensing: analysis of RF, ANN, and SVM regression models. *Remote Sensing*, *9*. doi:10.3390/rs9040309

Zengeya, F. M., Mutanga, O., & Murwira, A. (2012). Linking remotely sensed forage quality estimates from worldview-2 multispectral data with cattle distribution in a savanna landscape. *International Journal of Applied Earth Observation and Geoinformation*, *21*(1), 513–524. doi:10.1016/j.jag.2012.07.008

Zielinska, K. D., Goliński, P., Jorgensen, M., Mølmann, J., Taff, G., Tomaszewska, M., … Gatkowska, M. (2015). New methodologies for grasslands monitoring. In *23rd international grassland congress (xxiii igc)*, New Delhi, India: Range Management Society of India.

Zillmann, E., Gonzalez, A., Montero Herrero, E. J., Van Wolvelaer, J., Esch, T., Keil, M., … Garzón, A. M. (2014). Pan-European grassland mapping using seasonal statistics from multisensor image time series. *IEEE Journal of Selected Topics in Applied Earth Observations and Remote Sensing*, *7*(8), 3461–3472. doi:10.1109/JSTARS.2014.2321432